UNICA

UNIVERSITÀ
DEGLI STUDI
DI CAGLIARI

Ph.D. DEGREE IN

Industrial Engineering

Cycle XXXVIII

TITLE OF THE Ph.D. THESIS

LARGE EDDY SIMULATION OF TURBULENT HYDROGEN FLAMES

Scientific Disciplinary Sector(s)

IIND – 06/A Macchine a Fluido

Ph.D. Student:	**Antonio Masucci**
Supervisor	**Prof. Ing. Tiziano Ghisu**
Co. Supervisor	**Prof. Ing. Francesco Cambuli**

Final exam. Academic Year 2024/2025

Thesis defence session: July 2026

List of Publications

Journal Articles

1. **Masucci A.**, Porcarelli A., Ghisu T. and Langella I., 2025, "*Investigation of tangential strain rate impact on NO emissions in turbulent premixed hydrogen flames using the Eulerian Stochastic Fields approach*", **Combustion and Flame**.

2. **Masucci A.**, Ferrante G., Giusti A., Ghisu T. and Langella I., 2025, "*Investigation of Differential Diffusion and Strain Coupling in Large Eddy Simulations of Hydrogen-Air Flames*", **Combustion Science and Technology**.

3. **Masucci A.**, Ghisu T. and Giusti A., 2025, "*Numerical Investigation of Premixed and Non-Premixed Hydrogen Flames Using Large-Eddy Simulations and Flamelet Models*", **ASME Journal of Engineering Gas Turbines Power**.

Conferences

1. **Masucci A.**, Ferrante G., Giusti A., Ghisu T. and Langella I., 2025, "*Investigation of Differential Diffusion and Strain Coupling in Large Eddy Simulations of Hydrogen-Air Flames*", **13th Mediterranean Combustion Symposium**, Corfù, Greece, 1-5 June 2025.

2. **Masucci A.**, Ghisu T. and Giusti A., 2025, "*Numerical Investigation of Premixed and Non-Premixed Hydrogen Flames Using Large-Eddy Simulations and Flamelet Models*", **ASME Turbo Expo**, Memphis, Tennessee, 16-21 June 2025.

Abstract

Hydrogen is considered a promising energy carrier for low-carbon power generation, especially in gas turbine applications. However, its use introduces important challenges related to flame stability, strong differential diffusion effects, and increased nitrogen oxides (NO_x) emissions. These issues are particularly critical in lean premixed conditions, which are commonly used to limit emissions but lead to complex turbulence-chemistry interactions.

This dissertation investigates turbulent hydrogen combustion using large eddy simulation (LES) combined with advanced combustion modeling approaches. In particular, flamelet-based models and transported probability density function (PDF) methods based on the Eulerian stochastic fields (ESF) framework are employed to capture the interaction between turbulence and chemistry.

The study focuses on both premixed and non-premixed hydrogen flames, using well documented experimental configurations for validation. The numerical results are assessed against available measurements, demonstrating the capability of the investigated modeling approaches to reproduce key features of the flow and flame structure.

Special attention is given to the role of differential diffusion and flame stretch, with emphasis on tangential strain rate. The results show that these effects strongly influence flame structure, local reactivity, and stability, especially in lean premixed hydrogen–air mixtures. Their interaction leads to deviations from classical combustion behavior observed in hydrocarbon flames.

Finally, the impact of tangential strain rate on NO formation is analyzed. The findings indicate that strain can significantly affect NO production by modifying temperature, radical concentrations, and reaction pathways. In particular, increasing tangential strain is shown to reduce NO emissions under certain conditions, suggesting a potential strategy for emission control in hydrogen combustion systems.

Overall, this work provides a detailed assessment of LES-based combustion models for hydrogen flames and offers new insights into the coupled effects of strain and differential diffusion on flame behavior and pollutant formation.

Contents

1 Introduction **11**
- 1.1 Hydrogen as energy carrier . . . 14
- 1.2 Hydrogen Production Pathways and Costs . . . 15
- 1.3 Utilization of Hydrogen in Gas Turbines . . . 17
  - 1.3.1 Challenges . . . 18
  - 1.3.2 NO_x Emissions . . . 20
  - 1.3.3 Hydrogen Lean Premixed Combustion . . . 22
  - 1.3.4 Stabilization . . . 24
- 1.4 Numerical combustion modeling . . . 27
- 1.5 Aims and Objectives . . . 30
- 1.6 Outline . . . 30

2 Technical Background **33**
- 2.1 Thermochemical Relations . . . 33
- 2.2 Molecular transport . . . 34
- 2.3 Governing Equations . . . 35
  - 2.3.1 Equations of fluid motion . . . 35
  - 2.3.2 Species transport equation . . . 36
  - 2.3.3 Enthalpy equation . . . 36
  - 2.3.4 Low Mach approximation . . . 37
- 2.4 Non-premixed combustion . . . 39
  - 2.4.1 Key parameters of non-premixed flames . . . 40
- 2.5 Premixed combustion . . . 41
  - 2.5.1 Key parameters of premixed flames . . . 41
  - 2.5.2 Stretch effects . . . 44
  - 2.5.3 Intrinsic flame instabilities . . . 46
- 2.6 Turbulent combustion . . . 49
  - 2.6.1 Turbulent premixed flames . . . 49
  - 2.6.2 Combustion regimes . . . 50

2.7 Modeling . . . 52
2.7.1 Turbulence modeling . . . 52
2.7.2 Large Eddy Simulation . . . 54
2.7.3 Turbulent combustion modeling . . . 55

3 Methods **61**
3.1 Flamelet-based model . . . 61
3.1.1 Non-premixed combustion . . . 61
3.1.2 Partially premixed combustion . . . 62
3.2 Transported FDF approach . . . 67
3.2.1 Eulerian stochastic fields approach . . . 68

4 Test Cases **71**
4.1 NTNU case . . . 71
4.2 HYLON case . . . 73

5 Investigation of Premixed and Non-Premixed Hydrogen Flames Using LES with Flamelet Models **75**
5.1 Introduction . . . 75
5.2 Numerical Methods . . . 76
5.2.1 NTNU case . . . 77
5.2.2 HYLON case . . . 79
5.3 Results and Discussion . . . 81
5.3.1 NTNU case . . . 81
5.3.2 HYLON case . . . 85
5.4 Summary and Conclusions . . . 90

6 Investigation of Differential Diffusion and Strain Coupling in LES of Hydrogen Premixed Flames **91**
6.1 Introduction . . . 91
6.2 Numerical Methods . . . 93
6.3 Results and Discussion . . . 94
6.3.1 Validation and flame structure . . . 94
6.3.2 Average resolved stretch effects . . . 97
6.3.3 Reacting states . . . 100
6.4 Summary and Conclusions . . . 103

7 Investigation of tangential strain rate impact on NO emissions **105**
7.1 Introduction . . . 106
7.2 Case study and operating conditions . . . 108
7.3 Numerical set-up . . . 108
7.3.1 3-D case . . . 108
7.3.2 1-D Counterflow setup . . . 110

7.4 Results and Discussion . . . 111
7.4.1 Validation . . . 111
7.4.2 Reacting states . . . 116
7.4.3 Tangential strain effects on the flame structure . . . 118
7.4.4 Tangential strain effects on NO emissions . . . 121
7.5 Summary and Conclusions . . . 125

8 Conclusions and Outlooks **127**
8.1 Summary and Conclusions . . . 127
8.2 Future Work . . . 129

1 Introduction

Anthropogenic emissions of greenhouse gases are widely recognized as the dominant cause of the ongoing change in Earth's climate [1]. A strong link exists between the concentration of greenhouse gases in the atmosphere, in particular carbon dioxide (CO_2), and the global mean surface temperature. This relationship is well documented and has been observed throughout the climatic history of the planet [2]. An increase in the atmospheric concentration of these gases alters the radiative balance of the atmosphere. As a result, part of the outgoing solar radiation is absorbed and re-emitted, leading to a warming of both the Earth's surface and the lower layers of the atmosphere [3].

Since the onset of the industrial era, human activities have substantially disrupted this natural balance, producing a rate of global temperature rise that is unprecedented in the instrumental record.

Fig. 1.1 shows the evolution of the global mean surface temperature anomaly relative to a pre-industrial baseline, defined here as the average temperature over the period 1861–1890. The data indicate a sustained warming trend, with current global mean temperatures exceeding pre-industrial values by approximately 1.3 to 1.55 °C [4]. This level of warming has already produced measurable effects on natural systems and human activities, and further increases in temperature are expected to amplify these impacts.

The rise in sea level represents one of the most severe consequences of global climate change, as increasing temperatures accelerate the melting of ice sheets and glaciers. This process leads to higher sea levels as well as rising water levels in rivers and lakes, thereby increasing the risk of flooding and associated damage [6]. Climate change also alters precipitation regimes and contributes to a higher frequency and intensity of extreme weather events, including heatwaves, heavy rainfall, and storms [7, 8]. Limiting further warming therefore requires rapid and substantial reductions in greenhouse gas emissions, which in turn demand major changes in the way energy is generated and consumed, industrial processes are carried out, and food is produced [9].

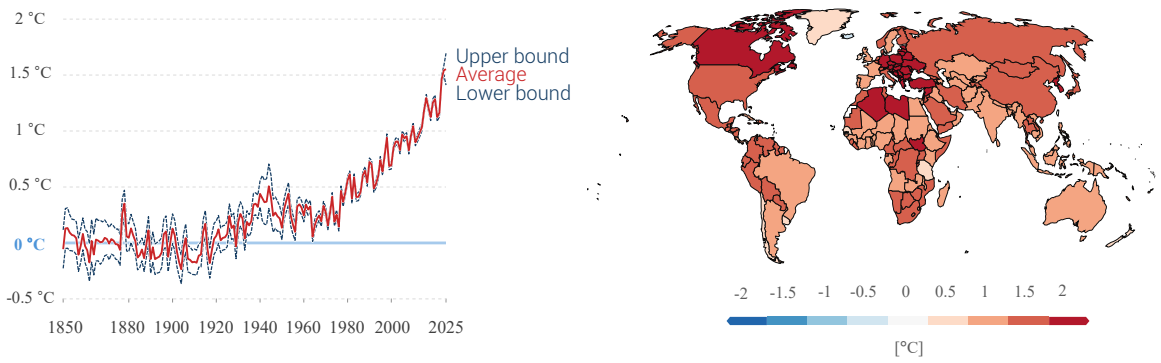

Figure 1.1: Temperature anomaly, measured as the difference between the average land-sea surface temperature in a given year and the 1861-1890 mean, in degrees Celsius (left) and difference between 2025 average surface temperature and the 1991-2020 mean, in degrees Celsius (right) [5].

Greenhouse gas emissions, including carbon dioxide (CO_2) and nitrous oxide (N_2O), mainly arise from the combustion of fossil fuels, energy demanding industrial activities such as steel and cement production, and agricultural practices [10]. In 2024, total global emissions from human activities reached approximately 53.2 GTs of CO_2 equivalent [11]. The development of effective mitigation strategies therefore relies on a detailed assessment of the contribution of different economic sectors, in order to identify the areas where emission reductions can be most effectively achieved [12].

Fig. 1.2 illustrates the global distribution of greenhouse gas emissions across economic sectors [13]. The figure highlights the complexity of the climate problem, as emissions originate from a broad range of activities throughout the global economy. Consequently, no single technology or individual sector can provide the reductions required to limit climate change on its own. Instead, meaningful progress depends on coordinated mitigation efforts involving multiple sectors.

The energy sector is responsible for almost three quarters of global greenhouse gas emissions. Reducing emissions from electricity generation is a central element of mitigation efforts, however, this alone is not sufficient. Significant emission reductions also depend on the widespread use of electricity in sectors where energy is currently supplied mainly by direct fuel combustion, such as space heating and road transport. In addition, some activities, including aviation and maritime transport, still lack technological solutions that are both technically viable and deployable at large scale, which makes emission reductions in these sectors particularly difficult [15].

Fig. 1.3 shows the contribution of primary energy sources to global carbon dioxide

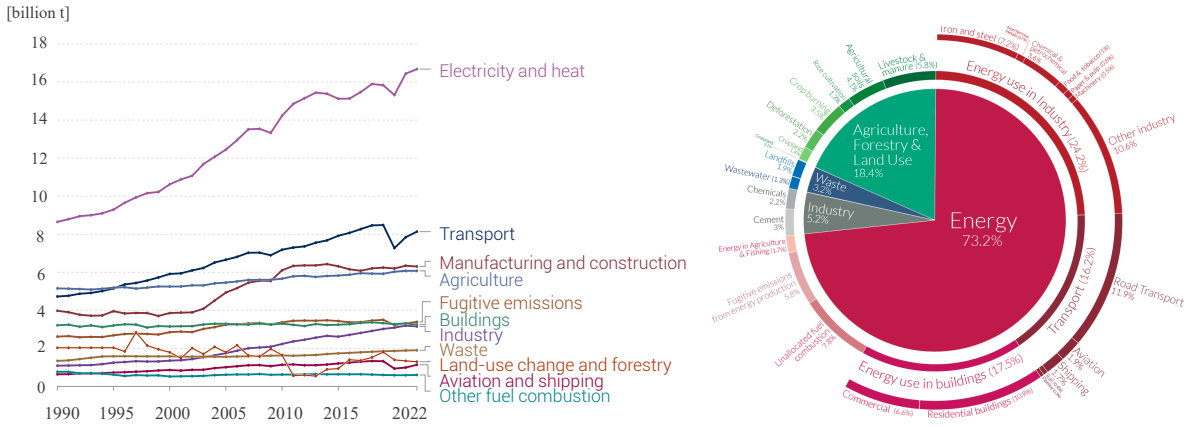

Figure 1.2: Global greenhouse gas emissions by sector from 1990 to 2022 (left) and percentage distribution for the year 2020 by sector(right) [14].

emissions. Although renewable energy production has increased rapidly in recent years, fossil fuels, specifically coal, oil, and natural gas, continue to dominate the global energy system. Together, they account for approximately 77% of total primary energy supply and remain the main source of human related carbon dioxide emissions [16].

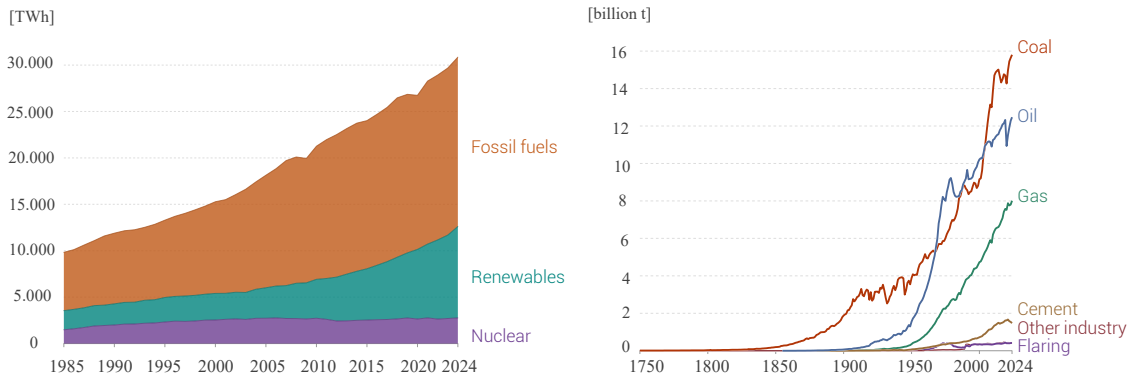

Figure 1.3: Global electricity generation by source (left) and the corresponding CO_2 emissions from fossil fuel sources (right) [13].

Energy production and environmental impact are closely connected. In an ideal setting, sustainable development would be based entirely on energy systems that do not produce harmful emissions. In reality, however, every energy conversion process involves some impact on the environment. For this reason, improvements in energy

efficiency play a central role in reducing environmental pressure. For a fixed level of delivered energy service or material output, higher efficiency generally results in lower fuel consumption and reduced pollutant emissions, thereby reinforcing the connection between efficiency gains and environmental sustainability.
Since the Industrial Revolution, the extensive use of coal, oil, and natural gas has supported economic growth on an unprecedented scale, while at the same time contributing to the increase in atmospheric carbon dioxide concentrations and the emergence of global warming [10, 17]. In this context, sustainable energy engineering seeks to exploit available energy resources in ways that are consistent with long term environmental protection and societal needs. This approach includes the continued use of fossil fuels operated at high efficiency and combined with technologies for carbon capture and storage [17, 18]. Within this framework, hydrogen has gained increasing attention as an energy carrier with the potential to enable substantial emission reductions across several parts of the energy system [17–19].

1.1 Hydrogen as energy carrier

Hydrogen is widely regarded as a potential contributor to the reduction of greenhouse gas emissions across the global energy system. Its high specific energy, versatility, and wide availability make it attractive for use in a range of applications.
In contrast to fossil fuels, hydrogen does not contain carbon and therefore it does not produce carbon dioxide emissions when used in electrochemical fuel cells or combustion devices [20, 21]. When obtained through processes with low associated emissions, such as water electrolysis powered by renewable or nuclear energy, hydrogen can lead to substantial reductions in greenhouse gas emissions, particularly in sectors where direct electrification remains difficult. Hydrogen is especially well suited to applications that require high energy density, long duration energy storage, or high temperature heat supply. These include heavy transport, aviation, maritime propulsion, and industrial heating processes [22]. In such cases, the use of electricity alone is often constrained by limitations in battery capacity, infrastructure requirements, or achievable power density. Under these conditions, hydrogen represents a viable alternative, acting not only as a fuel but also as an energy carrier that enables an indirect use of electricity from variable renewable sources in applications that are otherwise difficult to decarbonize [23].
Despite its potential to support substantial emission reductions, the widespread use of hydrogen presents significant technical challenges. Hydrogen air flames exhibit high laminar flame speeds, broad flammability ranges, strong thermodiffusive effects, and a marked sensitivity to flow strain and turbulence [24–26]. These characteristics increase the probability of flashback, thermoacoustic oscillations, and elevated formation of nitrogen oxides, particularly in premixed combustion systems and gas turbine combustors. Ensuring safe, stable, and efficient operation therefore

requires a detailed understanding of hydrogen flames behavior, especially under turbulent conditions.
From a modeling perspective, hydrogen combustion imposes demanding requirements due to the strong interaction between turbulence, chemical reactions, and molecular transport. Assumptions that are commonly acceptable for hydrocarbon fuels, such as the use of unity Lewis numbers, are often not valid for hydrogen flames. This limitation becomes especially relevant when accurate predictions of turbulent reacting flows are required.
As a result, major research challenges extend beyond hydrogen production pathways and their economic implications to include the integration of hydrogen into gas turbine systems for power generation. In this context, combustion stability, pollutant formation, and operational flexibility remain central issues that must be addressed to enable reliable and efficient hydrogen based energy conversion [27, 28].

1.2 Hydrogen Production Pathways and Costs

Hydrogen is considered an important energy carrier on the way to substantially reduce greenhouse gas emissions across the global energy system. Its high energy content per unit mass, applicability across a wide range of uses, and abundance in combined form make hydrogen a promising option for reducing emissions in sectors where direct electrification remains difficult.
Despite its long term promise, the current hydrogen supply chain relies predominantly on production routes associated with significant carbon dioxide emissions. Nowadays, most hydrogen is obtained from fossil resources, mainly through steam methane reforming of natural gas, a process that results in considerable carbon dioxide release [29–31]. Consequently, reducing the environmental impact of hydrogen use depends strongly on the development and large scale deployment of production methods with low or negligible associated emissions.
In response to this need, hydrogen production based on energy sources with low carbon intensity has attracted increasing attention from both research and industry in recent years. Initial efforts to differentiate among production pathways led to the introduction of a color based terminology. In this scheme, hydrogen produced from fossil fuels with direct emissions was labeled as gray, while hydrogen generated through water electrolysis powered by renewable electricity was referred to as green. Over time, additional colors were introduced to represent a broader range of production routes and energy inputs.
Although the term green hydrogen is now commonly associated with hydrogen produced by electrolysis using electricity from renewable sources, the electrolysis process itself is not restricted to renewable power sources. For example, electricity from nuclear energy can also be used to drive water electrolysis without direct carbon dioxide emissions. As a result, the increasing reliance on color based labels has

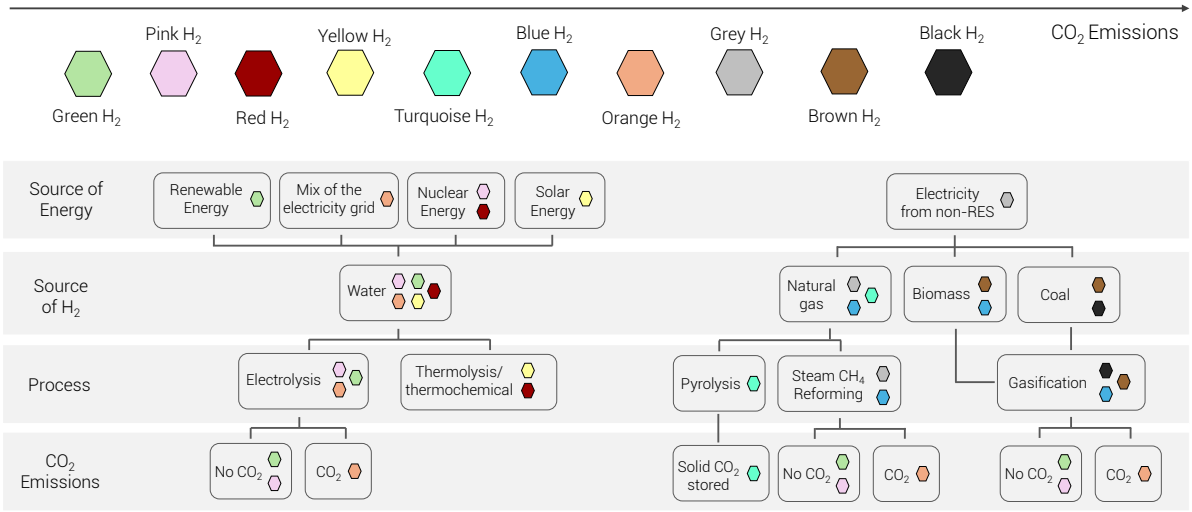

Figure 1.4: Overview of hydrogen color classifications and their respective production processes, reproduced from Ref. [32].

shifted the focus toward the origin of the energy supply rather than the underlying production process, giving rise to ambiguity and inconsistent usage across the literature.
The lack of a universally accepted color classification has therefore emphasized the need for clearer and more transparent frameworks to describe hydrogen production pathways. Within this context, a representative set of ten commonly cited hydrogen categories is summarized in Fig. 1.4 to illustrate the diversity of existing production routes.

- **Green hydrogen**: Generated via water electrolysis supplied exclusively by renewable energy sources (RES), resulting in no direct CO_2 emissions.
- **Red hydrogen**: Produced through nuclear-assisted thermolysis or thermochemical water splitting processes, without direct CO_2 emissions.
- **Pink hydrogen**: Obtained by water electrolysis driven by nuclear-generated electricity, with no direct CO_2 emissions.
- **Yellow hydrogen**: Generated using solar based pathways, such as solar thermochemical cycles, with no direct CO_2 emissions.
- **Turquoise hydrogen**: Produced via methane pyrolysis, yielding solid carbon as a by-product and negligible direct CO_2 emissions.
- **Blue hydrogen**: Derived from natural gas or biomass through steam methane reforming (SMR) or related reforming processes combined with carbon capture, utilization, and storage (CCUS), resulting in reduced CO_2 emissions.

- **Orange hydrogen**: Produced through electrolysis powered by a mixed electricity grid, with associated CO_2 emissions determined by the grid's carbon intensity.
- **Gray hydrogen**: Produced from natural gas via SMR without carbon capture, characterized by significant CO_2 emissions.
- **Brown hydrogen**: Obtained from lignite coal or biomass gasification, associated with high CO_2 emissions.
- **Black hydrogen**: Produced through the gasification of bituminous coal, with high CO_2 emissions.

Each mode of hydrogen production involves a different cost and a different amount of CO_2 emitted. The features associated to the different colors are summarized in Table 1.1:

Color	Cost [$/kg]	CO_2 emissions [kg_{CO_2}/kg_{H_2}]
Green	1.9 – 8.2	0 – 2.8
Red	2.2 – 2.6	≈ 0.1
Pink	3 – 7	0.3 – 0.6
Yellow	7.9 – 8.4	< 1.7
Turquoise	1.6 – 3.4	1.9 – 4.8
Blue	1.4 – 3.2	0.8 – 4.8
Orange	3.35 – 3.6	Up to fossil-like
Gray	0.7 – 2.3	7.5 – 13
Brown	1.3 – 2.5	18 – 25
Black	1.3 – 2.5	18 – 25

Table 1.1: Indicative cost and CO_2 emissions for hydrogen colors (values per kg H_2) from Ref. [32].

Although hydrogen production from renewable energy sources offers clear environmental benefits, its current cost is higher than the one of hydrogen obtained via conventional reforming methods.

1.3 Utilization of Hydrogen in Gas Turbines

Gas turbines play an important role in meeting global energy demand, providing efficient and flexible solutions for electricity generation and a wide range of industrial applications [33–35]. In such systems, the energy released by chemical reactions in the combustor is converted into mechanical work or electrical power. The type of fuel used in the combustion chamber strongly influences both the overall efficiency of the process and the level of pollutant emissions. Traditionally, fossil fuels such as oil and natural gas have been the dominant energy sources for gas turbine operation

[36]. Although these fuels enable high efficiency and reliable performance, their use leads to significant greenhouse gas emissions.
In order to reduce carbon dioxide emissions from power generation, alternative fuels have been increasingly investigated, with hydrogen receiving particular attention. When burned, hydrogen produces water vapor as the main combustion product, thereby avoiding direct carbon dioxide emissions [37, 38]. Therefore, the use of hydrogen as fuel in gas turbines represents a potential route toward cleaner energy conversion [39–42], substantially lowering greenhouse gas emissions compared to conventional fossil fuels and contributing to the achievement of climate mitigation objectives. At the same time, hydrogen introduces specific challenges related to its combustion behavior, which can affect operating stability, alter flame dynamics, influence pollutant formation, and raise concerns related to material durability and compatibility [43, 44].

1.3.1 Challenges

Understanding the influence of hydrogen on gas turbine performance is essential as research progresses toward increasing use of hydrogen as an energy carrier. Although hydrogen offers clear environmental advantages, its application in gas turbines requires careful design and optimization to ensure safe, efficient, and reliable operation [27]. The main challenges associated with the use of hydrogen as a gas turbine fuel are outlined below:

- **Storage**: Hydrogen storage represents a major challenge for its large-scale use in gas turbine applications. Although hydrogen has a lower heating value (LHV) higher than methane, its volumetric LHV is approximately one third of that of methane. As a consequence, achieving the same thermal power output requires fuel volume flow rates that are roughly three times higher, which imposes significant constraints on gas turbine and fuel system design [27]. In addition, materials used for hydrogen storage and transport are susceptible to hydrogen embrittlement. In this process, atomic hydrogen diffuses into metallic lattices, leading to a reduction in ductility and fracture toughness and increasing the likelihood of cracking and structural failure [27, 45]. Ensuring material integrity is therefore essential for safe and reliable operation. Economic factors further limit widespread deployment, as hydrogen storage requires dedicated infrastructure with higher costs compared to conventional fuels. Several storage approaches are currently under investigation [46–48], including high pressure compression, cryogenic liquefaction, and chemical carriers such as hydrogen–methane blends or ammonia.

- **Increased water content**: Although hydrogen combustion eliminates direct carbon dioxide emissions, it leads to a higher concentration of water vapor in the combustion products, introducing several engineering challenges for gas

turbine operation. One important concern is the impact on heat transfer within the turbine, as an increased water content can enhance the heat transfer coefficient between hot gases and solid surfaces. This may result in higher metal temperatures in critical components such as turbine blades, potentially reducing their durability and service life [49, 50]. Moreover, elevated water vapor levels can promote a more aggressive corrosive environment, decreasing the corrosion resistance of materials used in turbine components [51]. The performance of turbine cooling systems, which are designed to manage heat loads in high temperature regions, may also be affected, with possible implications for overall thermal management and efficiency [52].

- **High flame speed**: Hydrogen exhibits combustion characteristics that differ significantly from those of natural gas, most notably its very high flame speed [53]. While a high flame speed can improve combustion completeness, it poses challenges for flame stability and control, particularly by increasing the risk of flashback [21]. Flashback occurs when the flame propagation speed exceeds the local flow velocity, for instance within boundary layers, allowing the flame to travel upstream into the fuel injection system [27]. Such events can cause combustion in unintended regions and may lead to damage of the combustor or associated hardware. To reduce flashback risk in hydrogen or hydrogen–methane combustion, a range of mitigation measures can be employed, including flame arrestors, optical flame sensors, and pressure monitoring systems [54, 55]. However, these measures increase system complexity and can raise capital costs. Advanced combustion strategies, such as staged combustion and lean premixed operation, are also commonly adopted to improve flame control under high flame speed conditions.

- **High flame temperature**: Hydrogen–air combustion is characterized by a high adiabatic flame temperature, reaching approximately 2500 °C under stoichiometric conditions. Previous studies have shown that higher flame temperatures can improve thermodynamic efficiency by increasing the temperature difference between the combustion process and the exhaust gases, potentially enhancing gas turbine power output [56, 57]. However, elevated flame temperatures also promote the formation of nitrogen oxides (NO_x), representing one of the main challenges associated with hydrogen combustion in gas turbines [21]. To limit NO_x emissions, advanced combustion approaches such as lean premixed and staged combustion are commonly employed [58–61]. Although these techniques have demonstrated reductions in NO_x formation, further improvements are still required to meet increasingly stringent emission targets. High flame temperatures also affect material performance in combustors and turbine components. Long exposure to elevated temperatures can accelerate material degradation through oxidation and thermal stresses [44, 62], necessitating the use of advanced, heat resistant materials to ensure component relia-

bility and long service life.

1.3.2 NO_x Emissions

Hydrogen combustion behaves differently from traditional hydrocarbon fuels, especially in terms of emissions. One major issue is the formation of nitrogen oxides (NO_x), which are harmful pollutants [63]. Hydrogen flames can lead to relatively high NO_x levels, making emission control an important challenge.
Inside combustion systems, NO_x forms under high-temperature conditions and in highly turbulent flows. The situation is further complicated by the geometry of the combustion chamber, which strongly affects how air and fuel mix and move. Because of this combination of turbulence, temperature, and geometry, accurately predicting NO_x levels is not straightforward.
Another difficulty comes from the nature of the formation process itself. NO_x production involves both fluid dynamics and chemical reactions that interact with each other across different scales [64]. In turbulent flows, this interaction becomes even more complex. At the same time, the chemical reactions responsible for NO_x formation are relatively slow compared to the fast oxidation processes of the fuel [65].
As a result, the residence time of the gases inside the combustion chamber plays a key role. Since gases often leave the chamber before NO_x formation is complete, the system does not reach chemical equilibrium. This means that NO_x can continue to form even after the gases exit the combustion region, and its concentration can keep evolving [66]. For these reasons, predicting NO_x emissions requires a strong coupling between flow behavior and temperature fields. This coupling adds another layer of complexity and makes accurate modeling particularly challenging.
In recent years, many studies have explored lean premixed hydrogen combustion as a strategy to reduce emissions. Operating under lean conditions lowers the flame temperature, which helps limit NO_x formation, especially through the thermal mechanism. However, stabilizing and controlling hydrogen flames in such turbulent, lean conditions introduces additional technical challenges, which will be discussed in the next section.
NO_x is produced through several chemical pathways involving dissociation reactions during combustion. The most relevant mechanisms for this work are outlined below.

- **Thermal NO_x pathway**: This is the most important mechanism at high temperatures and is often referred to as the Zeldovich mechanism [67]. It starts when nitrogen (N_2) in the air breaks apart due to high temperature, producing atomic nitrogen:

$$N_2 + O \rightarrow NO + N \tag{1.1}$$

  The nitrogen atoms formed in this step then react with oxygen-containing species

such as O_2 and OH to produce nitrogen monoxide (NO):

$$N + O_2 \rightarrow NO + O \tag{1.2}$$
$$N + OH \rightarrow NO + H \tag{1.3}$$

Temperature is the main factor controlling this pathway. As temperature increases, the production of thermal NO_x rises quickly. Above about 1600°C, this mechanism becomes dominant over the others [68].
Residence time is also important. Since NO formation is relatively slow, longer residence times allow more NO_x to form. This is different from fuel oxidation, which happens much faster. As a result, increasing the time that gases stay in the combustion zone generally leads to higher NO_x emissions [69].

- **Prompt NO_x pathway**: This mechanism occurs directly in the flame front and is fast. It involves reactions between hydrocarbon radicals and nitrogen from the air. These reactions first produce intermediate species such as HCN, which are later oxidized to form NO [70]. This pathway is mainly relevant in hydrocarbon flames.

- **N_2O pathway**: In this case, nitrogen reacts with oxygen to form nitrous oxide (N2O), which is then converted into NO:

$$N_2 + O + M \rightarrow N_2O + M \tag{1.4}$$
$$N_2O + O \rightarrow 2, NO \tag{1.5}$$

This pathway becomes more relevant under lean combustion conditions [71]. However, it is often neglected because its overall contribution to NO_x formation is usually small [72].

- **NNH pathway**: This route involves the intermediate species NNH. It is formed when molecular nitrogen reacts with radicals such as H:

$$N_2 + H \rightarrow NNH \tag{1.6}$$
$$NNH + O \rightarrow NO + H \tag{1.7}$$

This mechanism is particularly important at lower temperatures and short residence times [73]. Under these conditions, it can become a major contributor to NO formation [74].

- **Fuel-N pathway**: This pathway only occurs when the fuel itself contains nitrogen. During combustion, fuel-bound nitrogen can form species such as NH_3 and HCN, which are then oxidized into NO. This mechanism is typical of fuels like coal and is generally not relevant for hydrogen combustion.

It is important to point out that these mechanisms mainly explain how nitrogen monoxide (NO) is formed. Nitrogen dioxide (NO_2) can also appear in combustion systems, but it is usually produced later, through the oxidation of NO. This process mainly takes place in cooler regions after the flame or in areas with excess oxygen. In most practical situations, however, the amount of NO_2 remains much lower than NO [75].
The higher NO_x emissions observed in premixed hydrogen flames, compared to hydrocarbon flames, are mainly linked to the thermal pathway. This is because hydrogen flames typically reach higher adiabatic flame temperatures, which strongly promote thermal NO formation.

1.3.3 Hydrogen Lean Premixed Combustion

Another significant technical challenge for the utilization of hydrogen in aircraft propulsion is the need to redesign gas turbine combustors to accommodate the unique characteristics of hydrogen combustion. Traditional aviation gas turbines typically operate with turbulent, often non-premixed combustion, in which liquid fuel is injected into the airflow and mixes with the oxidizer as combustion occurs. By contrast, lean premixed combustion, where the fuel is fully mixed with an excess of air before ignition, offers notable advantages, including improved fuel efficiency and reductions in pollutant emissions such as CO_2, CO, and NO_x [60, 76]. A schematic comparison of premixed and non-premixed (diffusion) combustion configurations is shown in Fig. 1.5.

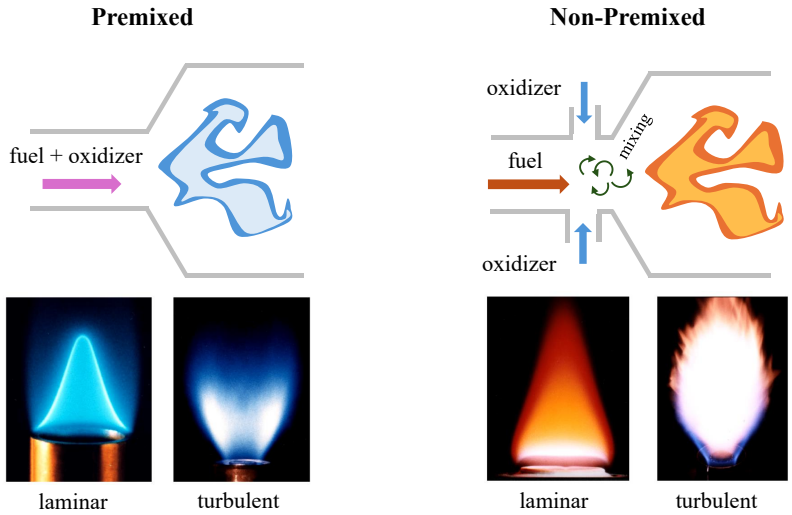

Figure 1.5: Schematic of premixed (left) and non-premixed (right) configurations, alongside laminar and turbulent experimental flames from Ref. [77].

Both premixed and diffusion flames present distinct advantages and limitations. Premixed flames typically achieve higher combustion efficiency because the fuel and

oxidizer are more uniformly distributed, which promotes rapid and complete combustion and generally results in lower pollutant formation. However, premixed flames often operate within a narrower stability range and are more susceptible to abnormal combustion events. In contrast, diffusion flames are generally more robust and can maintain stable operation over a wider range of conditions, although this comes at the expense of lower efficiency and higher emissions [78].
In premixed combustion systems, the flame stability is largely determined by the balance between the velocity of the incoming reactants and the speed at which the flame propagates. Departures from this balance can result in flame extinction through two distinct mechanisms, as illustrated in Fig. 1.6 [79, 80]. These extinction mechanisms are:

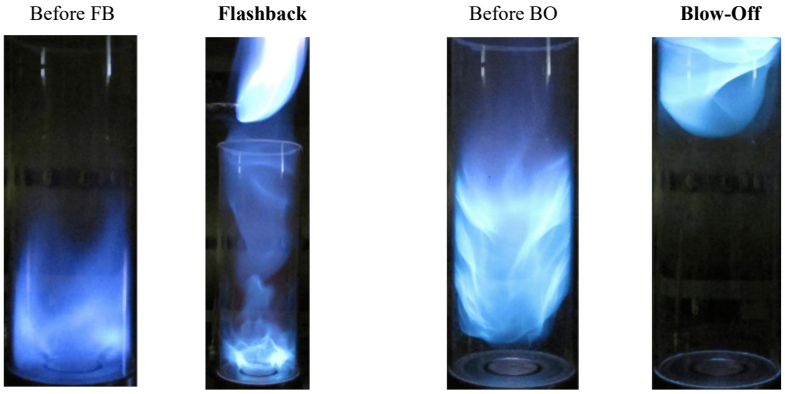

Figure 1.6: Flashback and blow-off for flames with fixed swirl. From left to right: before flashback, flashback, before blow-off, blow-off from Ref. [77]

- **Flashback**: Flashback occurs when the velocity of the reactant mixture entering the combustor falls below the flame propagation speed, allowing the flame to move upstream toward the fuel injection or mixing region. As the flame advances upstream, combustion occurs closer to the injector and may eventually cause self extinction or damage to the structures. Flashback induced by combustion instabilities is often linked to large amplitude pressure oscillations that temporarily reduce or even reverse the axial flow velocity [81]. Turbulence can further increase the risk of flashback by enlarging the flame surface area, which raises the effective turbulent flame speed [78]. Flashback is therefore a critical operational concern and typically occurs in regions of low flow velocity. Several modes of flashback have been identified, including *core* flashback, *boundary layer* flashback, *auto ignition driven* flashback, *thermoacoustically induced* flashback, and *combustion induced vortex breakdown (CIVB)* flashback [82].
- **Blow-off**: Blow-off occurs when the flow velocity of the reactants exceeds the flame propagation speed. In this case, the flame is convected downstream,

moving progressively away from the stabilizing region until it detaches and eventually extinguishes once a critical flow rate is reached. For systems fueled with hydrogen, blow-off is generally less of a concern. Due to hydrogen's simple chemical kinetics, its flames have very high laminar flame speeds, low lean flammability limits, and short auto-ignition delay times compared to hydrocarbon fuels such as methane [21].

Beyond flame stability, hydrogen–air combustion exhibits transport phenomena that differ fundamentally from those of methane–air flames. In hydrocarbon systems, thermal and mass diffusivities are often similar, corresponding to Lewis numbers close to unity. This approximation does not hold true in hydrogen flames, where the low molecular weight leads to mass diffusivities that are significantly higher than the corresponding thermal diffusivity. This imbalance gives rise to differential and preferential diffusion effects. Although sometimes used interchangeably, these terms describe distinct processes: *differential diffusion* refers to unequal mass diffusivities among chemical species, while *preferential diffusion* describes the mismatch between species mass diffusivity and the thermal diffusivity of the mixture, i.e., deviations from unity Lewis number [83].
These transport characteristics are responsible for thermodiffusive instabilities, which can strongly influence flame structure, heat release, and overall flame morphology [84]. The mechanisms driving these instabilities, particularly their interaction with turbulent flow, are not yet fully understood and remain challenging to predict and control. Nevertheless, they present opportunities for advancing combustion technologies, including improvements in efficiency, emissions reduction, enhanced fuel flexibility, and the design of more compact combustors. Because these instabilities span multiple scales, from local flame front perturbations to global flame behavior, they pose a significant challenge for predictive models currently used in combustor design [21].

1.3.4 Stabilization

The development of a commercial hydrogen gas turbine represents a challenge that requires a careful evaluation of alternative combustion strategies. In this context, two main approaches are commonly considered: non-premixed (diffusion) combustion and premixed combustion. In diffusion systems, fuel and air mix directly within the combustion chamber, leading to stoichiometric conditions and, thus, elevated flame temperatures. Premixed systems, in contrast, rely on the thorough mixing of fuel and air upstream of the combustion zone, which allows to control the flame temperature and a corresponding reduction in nitrogen oxide emissions.
Despite these advantages, premixed hydrogen combustion presents significant operational challenges. Due to hydrogen's high laminar flame speed and wide flammability range, the risks of flashback and lean blow-off are substantially increased and

must be carefully controlled. For this reason, dedicated flame stabilization techniques are required to ensure safe and reliable operation. Several stabilization concepts have been proposed and investigated for hydrogen-fueled gas turbines, an illustration of these is shown in Fig. 1.7. Among them we find:

- **Swirler**: Swirling flows are widely employed in gas turbines and industrial combustion systems, where they provide an effective aerodynamic mechanism for flame stabilization and for promoting rapid mixing between fuel and air [85]. Although premixed operation is relatively straightforward in natural gas combustors [86], hydrogen premixing introduces a considerably higher flashback risk, which necessitates a careful design of mixing strategies [87]. A key advantage of swirl-stabilized combustors lies in the formation of central recirculation zones and reverse flow regions, which transport hot combustion products upstream and support flame anchoring [88]. To achieve stable operation while limiting flashback, the design objective is to combine fast mixing with sufficient spatial separation between fuel injection and the flame. Approaches such as axial air injection and boundary layer air injection increase the axial momentum of the flow and locally reduce the fuel concentration, thereby leading to a lower flashback susceptibility [89].

- **Bluff-Body**: In premixed combustors equipped with bluff-body flame holders, flame stabilization is governed by the interaction between the incoming combustible mixture and the hot products trapped within the recirculation region downstream of the obstacle. Continuous ignition occurs within the shear layers that bound this region, where fresh reactants are repeatedly exposed to high temperatures and reactive species [94]. The geometry of the bluff body plays a crucial role in determining flame stability, as it controls both the size and the structure of the wake region [95]. Although bluff bodies are most commonly used in premixed configurations, additional fuel or air injection along the wake centerline may be employed to further improve stabilization [96]. The flame holder is often shaped to locally accelerate the flow, increasing axial velocity near the bluff-body and reducing the risk of flashback. In these configurations, turbulence is mainly generated at the base of the bluff body, where strong acceleration produces large strain rates acting on the flame front. These strain effects influence chemical reaction rates and can enhance the flame stability, particularly under lean hydrogen combustion conditions [97].

- **Micro-Mix**: The Micromix combustion concept is based on the injection of hydrogen through a large number of small ports into an accelerated air stream. Fuel–air interaction is governed by jet-in-crossflow dynamics, which enable rapid mixing and aerodynamic flame stabilization without the need for large recirculation zones. With appropriate geometric design, stable combustion can be achieved while maintaining compact flame structures. The small characteristic size of the flames reduces the residence time of nitrogen oxide precursors

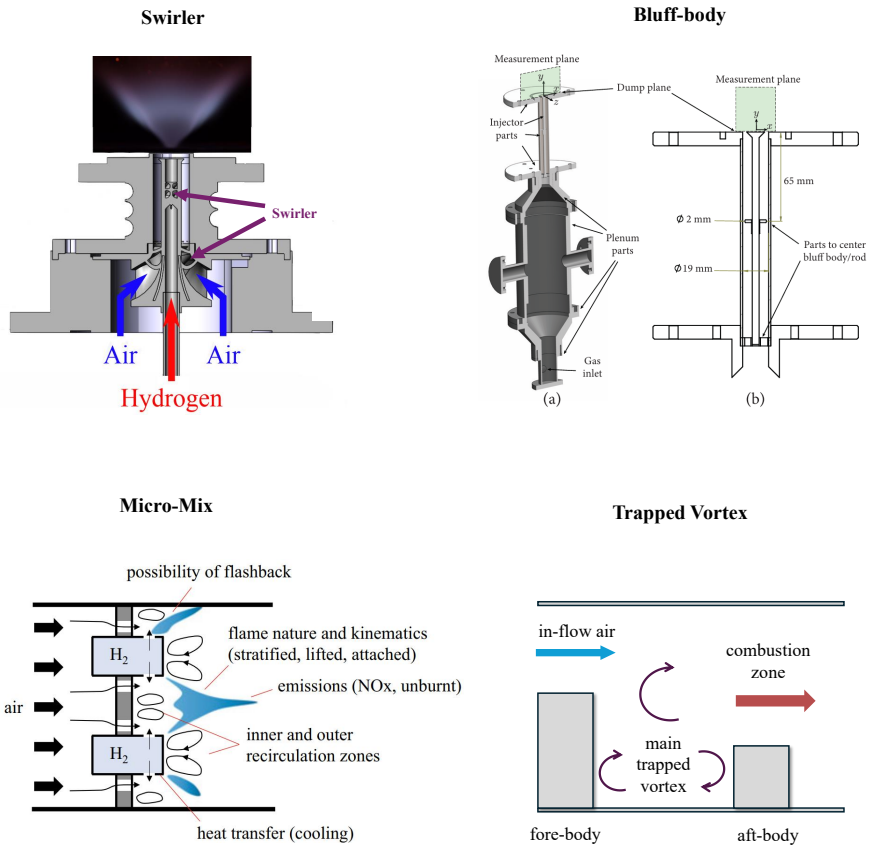

Figure 1.7: Flame stabilization concepts: (top-left) HYLON-IMFT swirled combustor [90]; (top-right) bluff-body stabilized flame [91]; (bottom-left) micromix combustor [92]; and (bottom-right) trapped-vortex combustor [93].

in high temperature regions, resulting in significantly lower emissions. In addition, since flammable mixtures are not present upstream of the injection locations, the risk of flashback is inherently minimized [98]. Unlike conventional combustors that rely on a single large recirculation zone to stabilize a global flame, Micromix systems generate multiple localized recirculation regions in the wakes of individual air jets at the burner inlet. These flow structures anchor a distributed set of small flames rather than a single continuous flame front. Depending on the design, hydrogen injection may occur in coflow or crossflow arrangements relative to the air stream, leading to flame lift-off and partial premixing upstream of the reaction zone. As a result, the combustor may exhibit either a globally lifted flame or a collection of discrete flamelets under both swirling and non-swirling conditions [92]. Achieving very low nitrogen oxide emissions requires that most of the fuel–air mixing occurs before ignition, thereby avoiding locally stoichiometric conditions within the reacting region.

- **Trapped Vortex**: Trapped vortex combustors achieve flame stabilization by means of a cavity integrated into the combustor wall, where a vortex is formed and

confined between upstream and downstream bodies. This cavity contains a hot, strongly recirculating flow that is largely isolated from the main stream, protecting the stabilized flame from high external velocities. As a result, stable combustion can be maintained even at very high flow speeds, making this concept particularly suitable for lean operation [93]. One of the main advantages of trapped vortex combustors is their ability to operate at high inlet velocities, including supersonic regimes [99, 100]. This feature is especially relevant for hydrogen combustion, where the high laminar flame speed significantly increases the risk of flashback [101]. Preventing flashback requires bulk flow velocities that exceed the flame propagation speed, conditions under which conventional swirl stabilization becomes less effective [102]. These difficulties are further amplified in lean premixed systems, where flashback into the injector can lead to severe hardware damage. In this context, trapped vortex combustors represent a promising alternative, offering stable combustion with relatively low pressure losses and reduced sensitivity to acoustic disturbances [103, 104]. A key aspect of their operation is the controlled transport of hot combustion products from the cavity into the main flow [105], which can be enhanced by wake regions generated by struts or other solid bodies [106, 107]. By relying on geometric confinement rather than purely aerodynamic stabilization, trapped vortex combustors exhibit reduced sensitivity to combustion instabilities, particularly near lean blow-off conditions. This enables an extension of both lean and rich stability limits [108].

1.4 Numerical combustion modeling

Numerical simulations have become an essential tool in the development and analysis of modern combustion systems. Over the past two decades, research activity has increasingly focused on large eddy simulation (LES), largely as a result of the steady growth in available computational resources. By resolving the dominant turbulent structures while modeling only the smaller scales, LES has substantially improved the predictive capability of numerical combustion studies. Despite these advances, the routine use of LES in industrial design remains limited by its high computational cost. Moreover, LES results used for engineering decisions should be supported by a careful evaluation of uncertainties arising from modeling choices and numerical discretization [109].

The numerical description of turbulent reacting flows plays a central role in the development of combustion systems aimed to improve efficiency while reducing pollutant emissions [110, 111]. As computing power has increased, LES has gained broader acceptance and has begun to appear in industrial practice, mainly for selected configurations and detailed analyses rather than for systematic design tasks [112]. Compared with Reynolds averaged Navier Stokes (RANS) methods, LES pro-

vides a higher degree of physical detail, while remaining significantly less demanding than direct numerical simulation (DNS). This intermediate level of fidelity makes LES well suited for the investigation of coupled phenomena such as turbulence–chemistry interaction (TCI), transport effects, and multiphase processes in regimes that cannot be addressed by DNS [113].

Within the LES framework, the governing equations are spatially filtered in order to resolve flow structures larger than a prescribed length scale. The influence of the unresolved motions at the smallest scales on the resolved ones are taken into account using subgrid-scale models (SGS). The interaction between the resolved field and the unresolved scales depends on both the filtering operation and the closure model employed, making their effects inherently intertlinked [114]. As a result, the validation and assessment of models for the unresolved scales is not straightforward. In addition, LES predictions are known to be sensitive to grid resolution, grid anisotropy, and the specification of boundary conditions.

Many modeling approaches originally developed for non-reacting flows have been extended to reacting configurations. In particular, closures for the unresolved stresses in the momentum equations often rely on the gradient hypothesis, leading to linear eddy viscosity formulations with either fixed coefficients [115–117] or coefficients determined dynamically during the simulation [118, 119]. However, since chemical reactions and heat release predominantly occur at the smallest scales, particular attention is required to model reacting flows. Despite these limitations, LES is generally regarded as providing more reliable predictions of reacting flows than lower resolution approaches [120].

Combustion processes occur over a wide range of regimes, and no single modeling strategy can be applied universally.

In non-premixed configurations, fuel and oxidizer are introduced separately and react only after mixing through molecular diffusion and turbulence. In such flows, particularly at high turbulence levels, an accurate representation of mixture fraction transport at unresolved scales is essential in order to capture the controlled mixing nature of the combustion process [121].

In premixed combustion, chemical reactions are typically confined to thin zones that propagate through the flow in the form of flame fronts. This propagation is characterized by the burning velocity, which reflects the combined influence of chemical kinetics and local flow conditions. In turbulent premixed flames, interactions between turbulent eddies and the flame front modify the effective propagation speed, making its modeling a key aspect of LES [121].

Partially premixed combustion exhibits characteristics of both premixed and non-premixed regimes. Locally, well mixed but unreacted mixtures may coexist with regions where combustion is controlled by diffusion, such as in recirculation zones, lifted flames, or shear layers formed by interacting fuel and oxidizer streams. Accurately describing such flows requires modeling approaches capable of consistently representing both combustion modes [121]. As a result, a broad range of combus-

tion models has been proposed to address these diverse regimes [110, 111, 121–124]. In LES, the influence of unresolved turbulence on flame wrinkling is often described using a statistical formulation. In this framework, the unresolved variability of the thermochemical state is represented by a filtered density function (FDF). The shape of this function may be assumed in advance, leading to the presumed FDF approach, or it may be obtained by solving a transport equation for the FDF itself, known as the transported FDF formulation [110, 121, 125, 126]. In the latter case, the transport equation is reconstructed through the evolution of stochastic representations of the thermochemical state, which may take the form of Lagrangian particles or Eulerian stochastic fields that represent instantaneous states throughout the computational domain [127, 128].

When hydrogen combustion is considered, combustion models originally developed for hydrocarbon fuels require careful reassessment. Many such models rely on the assumption of unity Lewis number, an approximation that does not hold for hydrogen–air mixtures and can lead to substantial errors if applied without modification.

In addition to differential diffusion effects, the tangential strain rate plays a central role in determining the behavior of hydrogen flames. Previous studies have shown that the strong preferential diffusion of hydrogen and its sensitivity to strain are closely linked and jointly govern flame response [129, 130]. Early investigations of flames with fuel Lewis numbers below unity demonstrated that increasing strain rates can lead to excess enthalpy relative to unstretched laminar flames, resulting in increased flame speeds [131]. Unlike hydrocarbon flames, which weaken and ultimately extinguish as strain increases, hydrogen flames have been shown to remain stable at significantly higher strain rates [132, 133].

Although hydrogen-enriched fuels and hydrogen blending have been widely studied [132–136], the combined influence of hydrogen's transport properties and high strain rates in pure, lean premixed hydrogen–air flames remains insufficiently understood. This gap is particularly evident in relation to flame stability and nitrogen oxide formation, highlighting the need for further investigation.

Moreover, in lean premixed hydrogen flames, the interaction between flame stretch and non-unity Lewis number effects can lead to thermodiffusive instabilities that may amplify under certain conditions [137]. These effects are especially pronounced in turbulent flows, where turbulence further strengthens the coupling between strain and differential diffusion mechanisms [138].

Such phenomena present significant challenges not only for flame stabilization but also for the predictive capability of existing combustion models used in computational fluid dynamics. This is particularly relevant for LES, which is increasingly employed in the analysis and design of advanced combustion systems. Ensuring the robustness and accuracy of these models is therefore a central objective.

1.5 Aims and Objectives

The main goal of this dissertation is to improve the understanding and prediction of turbulent hydrogen combustion using high-fidelity numerical methods such as large eddy simulations (LES). In particular, this work focuses on lean premixed hydrogen–air flames, which are relevant for low-emission energy systems but remain challenging to model accurately.
To achieve this goal, large eddy simulations are combined with advanced combustion modeling approaches, including flamelet-based methods and transported probability density function (PDF) models based on the Eulerian stochastic fields (ESF) framework. These tools are used to capture the interaction between turbulence and chemistry.
A key aspect of this work is the investigation of physical mechanisms that are particularly important in hydrogen combustion. Special attention is given to differential diffusion effects and tangential strain rate, as well as their interaction and combined influence on flame characteristics. These phenomena play a major role in determining flame structure, stability, and pollutant formation.
The objectives of this dissertation can be summarized as follows:

- Assess the capability of flamelet-based models to predict both premixed and non-premixed hydrogen flames under different operating conditions by validating LES results against available experimental data for canonical test cases.
- Analyze the role of differential diffusion and flame stretch and their effects on flame structure and dynamics.
- Evaluate the impact of tangential strain rate on NO_x formation and identify potential mechanisms for emission control.

1.6 Outline

This dissertation is organized into several chapters, each addressing a specific aspect of hydrogen combustion modeling. Chapter 2 presents the theoretical and physical background required for this work, introducing the governing equations for reacting flows, thermochemical relations, and molecular transport processes. It also reviews the main concepts of premixed and non-premixed combustion, as well as turbulence–chemistry interaction and combustion regimes. Chapter 3 describes the numerical methods used in this study. In particular, it focuses on flamelet-based models for different combustion regimes and on the transported PDF method using the Eulerian stochastic fields approach. Moreover, these methods are discussed in the context of their applicability to hydrogen combustion. Chapter 4 presents the test cases used for validation and analysis, along with the corresponding experimental

data for comparison. Chapter 5 presents a first investigation of both premixed and non-premixed hydrogen flames using LES coupled with flamelet models without including differential diffusion effects. The results are validated against experimental measurements, and the performance of the models is assessed. Chapter 6 focuses on the analysis of differential diffusion and strain coupling in turbulent premixed hydrogen flames. The effects of these mechanisms on flame structure and reacting states are examined in detail. Chapter 7 investigates the influence of tangential strain rate on NO_x emissions. The relationship between strain, flame structure, and pollutant formation is analyzed, providing insights into possible strategies for emission reduction. Chapter 8 concludes the work, summarizing the main findings and suggesting perspectives for future research.

2 Technical Background

Large eddy simulation is a high fidelity numerical method that can offer good accuracy for complex fluid dynamics problems such as simulations of turbulent reacting flows and aerodynamically complex configurations [114, 121]. In this approach, the large, energy-containing turbulent eddies are computed directly, while the effects of smaller eddies below a chosen filter width are modeled. A major challenge in applying LES to turbulent combustion is the interaction between turbulence and chemistry at the unresolved subgrid scales. The chemical reaction rates are highly nonlinear and appear in the filtered scalar equations as unclosed source terms and, therefore, require modeling. Several combustion models have been proposed in the literature to address this closure problem and will be summarized at the end of this chapter. This dissertation focuses primarily on a fully premixed test case. However, to evaluate the performance of flamelet models across different combustion regimes, a non-premixed flame is also investigated. This chapter, therefore, reviews key modeling techniques with emphasis on premixed combustion, introduces fundamental concepts of non-premixed combustion, and presents basic principles of numerical combustion modeling.

2.1 Thermochemical Relations

In reacting flows, several chemical species participate in the combustion process. The number of species involved depends on the composition of the fuel and the oxidizer. It is therefore useful to introduce a dimensionless quantity that measures the ratio between the mass of species k, denoted m_k, and the total mass m. This quantity is called the *mass fraction*:

$$Y_k = \frac{m_k}{m} \tag{2.1}$$

Alternative measures can also be used. An example is the *mole fraction* defined as $X_k = N_k/N$, where N_k represents the number of moles of species k and N is the total number of moles [123]. Mass fractions are often preferred because the total mass is

a conserved quantity and is therefore a useful property from a fluid mechanics point of view. Mass fractions are linked to mole fractions by the following relation:

$$Y_k = \frac{W_k}{W} X_k \tag{2.2}$$

Here, W_k is the molecular weight of species k and W is the mean molecular weight of the mixture calculated as $W = \sum_{k=1}^{N} X_k W_k$. The energy equation is usually written in terms of absolute enthalpy, defined as the sum of sensible and chemical enthalpy. The sensible enthalpy accounts for the change due to temperature variation during the combustion process whereas the chemical enthalpy accounts for the change in composition during chemical reactions. The absolute enthalpy of species k is then calculated as:

$$h_k = \underbrace{\int_{T_0}^{T} C_{p,k}\, dT}_{\text{sensible}} + \underbrace{\Delta h^0_{f,k}}_{\text{chemical}} \tag{2.3}$$

Here, T_0 is a reference temperature, usually set to 298.15 K. At this temperature, the sensible enthalpy h_{sk} is zero, although the enthalpy of formation $\Delta h^0_{f,k}$ of species k is not. One more point concerns the heat capacities at constant pressure $C_{p,k}$. In reacting flows, this quantity changes significantly due to large temperature variations. Their values are usually tabulated as functions of temperature using polynomials (JANAF [**139**]). For a mixture of N species, the enthalpy of the mixture is finally calculated as:

$$h = \sum_{k=1}^{N} \left(\int_{T_0}^{T} C_{p,k}\, dT + \Delta h^0_{f,k} \right) Y_k = \int_{T_0}^{T} C_p\, dT + \sum_{k=1}^{N} \Delta h^0_{f,k} Y_k \tag{2.4}$$

where the heat capacity at constant pressure of the mixture is calculated as:

$$C_p = \sum_{k=1}^{N} C_{p,k} Y_k \tag{2.5}$$

making the constant heat capacity at constant pressure a function of both temperature and mixture composition.

2.2 Molecular transport

Key diffusive processes in gases are described by three coefficients: thermal diffusivity α, species mass diffusivity D_k, and kinematic viscosity ν. These quantities describe how fast temperature, species concentration, and momentum spread in the gas because of molecular motion. Dimensionless numbers compare their relative effects:

- **Lewis number**: is the ratio of the thermal diffusivity to the mass diffusivity of that species:

$$Le_k = \frac{\alpha}{D_k} = \frac{Sc_k}{Pr} \tag{2.6}$$

- **Schmidt number**: compares the diffusive transport of momentum with the mass diffusion of the species

$$Sc_k = \frac{\nu}{D_k} \tag{2.7}$$

- **Prandtl number**: compares the diffusive transport of momentum with thermal diffusivity:

$$Pr = \frac{\nu}{\alpha} \tag{2.8}$$

2.3 Governing Equations

2.3.1 Equations of fluid motion

As explained in [140], when the mean free path of the molecules is smaller than the smallest geometric scales of the flow field, the continuum hypothesis can be applied. An ensemble of molecules can then be represented by a fluid particle. This particle is a volume average of molecules. The flow field can then be described by the mass conservation equation (2.9) and the momentum conservation equation (2.10):

$$\frac{\partial \rho}{\partial t} + \frac{\partial \rho u_i}{\partial x_i} = 0 \tag{2.9}$$

$$\frac{\partial \rho u_j}{\partial t} + \frac{\partial \rho u_i u_j}{\partial x_i} = -\frac{\partial p}{\partial x_j} + \frac{\partial \tau_{ij}}{\partial x_i} + \rho \sum_{k=1}^{N} Y_k f_{k,j} \tag{2.10}$$

Here, $f_{k,j}$ is the volume force acting on species k in direction j, and p is the static pressure. The viscous tensor τ_{ij} that appears in Eq. (2.10) is defined as:

$$\tau_{ij} = -\frac{2}{3}\mu \frac{\partial u_k}{\partial x_k}\delta_{ij} + \mu\left(\frac{\partial u_i}{\partial x_j} + \frac{\partial u_j}{\partial x_i}\right) \tag{2.11}$$

Both the mass and momentum equations have the same form as in a non-reactive flow. However, in the momentum equation, the dependence of dynamic viscosity μ on temperature cannot be neglected in the presence of the large variations due to combustion. The same applies to density ρ because of gas dilation. Therefore, the local Reynolds number varies much more than in a non-reactive flow [123].

2.3.2 Species transport equation

In reactive flows, a large number of species may be involved. Therefore, an equation describing mass conservation for each species is required:

$$\frac{\partial \rho Y_k}{\partial t} + \frac{\partial \rho (u_i + V_{k,i}) Y_k}{\partial x_i} = \dot{\omega}_k \tag{2.12}$$

Here, $V_{k,i}$ is the i-component of the diffusion velocity V_k of species k, and $\dot{\omega}_k$ is the reaction rate of species k. The diffusion velocities V_k of the N species can be obtained by solving a system [141] which is difficult and costly to solve [142]. Therefore, the so-called Hirschfelder and Curtiss approximation [143] is generally used. This approximation is the best first-order solution to the exact system:

$$V_k X_k = -D_k \nabla X_k, \qquad D_k = \frac{1 - Y_k}{\sum_{j \neq k} X_j / D_{jk}} \tag{2.13}$$

The species transport equation can then be rewritten as:

$$\frac{\partial \rho Y_k}{\partial t} + \frac{\partial \rho u_i Y_k}{\partial x_i} = \frac{\partial}{\partial x_i} \left(\rho D_k \frac{W_k}{W} \frac{\partial X_k}{\partial x_i} \right) + \dot{\omega}_k \tag{2.14}$$

The diffusion coefficients D_k can often be linked to the thermal diffusivity D^T in many flames.

2.3.3 Enthalpy equation

The absolute enthalpy equation (sum of sensible and chemical enthalpy) reads:

$$\frac{\partial \rho h}{\partial t} + \frac{\partial \rho u_i h}{\partial x_i} = \frac{dp}{\partial t} - \frac{\partial q_i}{\partial x_i} + \tau_{ij} \frac{\partial u_j}{\partial x_j} + \dot{Q} + \rho \sum_{k=1}^{N} Y_k f_{k,j} V_{k,i} \tag{2.15}$$

Here, $\dot{Q}$ is a generic heat source term (not to be confused with the heat released by combustion). The term $\rho \sum_{k=1}^{N} Y_k f_{k,j} V_{k,i}$ is the power produced by the volume forces f_k acting on species k. The energy flux $\dot{q}$ has two contributions:

$$\dot{q} = \underbrace{-\lambda \frac{\partial T}{\partial x_i}}_{\text{heat conduction}} + \underbrace{\rho \sum_{k=1}^{N} h_k Y_k V_{k,i}}_{\text{species diffusion}} \tag{2.16}$$

The first term represents the conductive heat flux due to temperature gradients (Fourier's law). The second accounts for the diffusion of species with different enthalpies. En-

thalpy is a convenient variable because, at constant pressure, we can write:

$$du = \delta q - \delta w = \delta q - p\,dv \tag{2.17}$$

and

$$dh = du + p\,dv + v\,dp = \delta q + \underbrace{v\cancel{dp}}_{\text{dp = 0}} = \delta q. \tag{2.18}$$

If the combustion process is adiabatic, further simplifications are possible:

$$du = \cancel{\delta q} - \delta w = -p\,dv \tag{2.19}$$

$$dh = -p\,dv + p\,dv + v\,dp = 0, \quad \rightarrow \quad h = \text{const.} \tag{2.20}$$

The heat release due to combustion is given by the change in enthalpy between reactants and products. Before combustion, the enthalpy is mainly chemical. After combustion, it is mainly sensible. The system of equations is closed with the ideal gas equation of state:

$$\frac{p}{\rho} = \frac{R_0}{W}T \tag{2.21}$$

where R_0 is the universal gas constant and W is the mean molecular weight of the mixture.

2.3.4 Low Mach approximation

Many gas turbine combustors operate in the low Mach number regime. In this regime, velocities are smaller than 0.3 M, where M is the Mach number defined based on local fluid properties. Here, the acoustic component of the Navier-Stokes equations is decoupled from the basic flow physics. By reformulating the governing equations for this regime, it is possible to remove the CFL restriction imposed by the acoustic wave speed (that is, the local sound speed). In many applications, this allows an order of magnitude increase in the time step used [144]. A low Mach number reacting flow is characterized by small pressure variations, but large temperature and concentration gradients (and hence density changes). In these conditions, the density can change due to temperature variations, but remains independent of pressure. The non-dimensional flow variables are defined as [145]:

$$x_i = \hat{x}_i/L_{\text{ref}}, \quad t = \hat{t}u_{\text{ref}}/L_{\text{ref}} \tag{2.22}$$

$$\rho_i = \hat{\rho}/\rho_{\text{ref}}, \quad u_i = \hat{u}_i/u_{\text{ref}}, \quad p = \hat{p}/(\rho_{\text{ref}}u_{\text{ref}}^2) \tag{2.23}$$

$$\mu_i = \hat{\mu}/\mu(T_{\text{ref}}), \quad \lambda_i = \hat{\lambda}/\lambda(T_{\text{ref}}) \tag{2.24}$$

$$c_p = \hat{c}_p/c_p(T_{\text{ref}}), \quad c_v = \hat{c}_v/c_v(T_{\text{ref}}) \tag{2.25}$$

$$Y_k = \hat{Y}_k/Y_{k,\text{ref}}, \quad h = \hat{h}/(c_p(T_{\text{ref}})T_{\text{ref}}) \tag{2.26}$$

where the superscript '^' denotes a dimensional quantity while the subscript 'ref' denotes a reference quantity. The Prandtl, Reynolds and Mach number of the flow are defined with respect to the reference values:

$$Pr = \frac{\mu(T_{\text{ref}})c_p(T_{\text{ref}})}{\lambda(T_{\text{ref}})}, \quad Re = \frac{\rho_{\text{ref}} u_{\text{ref}} L_{\text{ref}}}{\mu(T_{\text{ref}})}, \quad M = \frac{u_{\text{ref}}}{\sqrt{\gamma\, T_{\text{ref}} R/\overline{W}}} \tag{2.27}$$

where R is the universal gas constant, $\overline{W}$ the mean molecular weight of the mixture and $\gamma = c_p(T_{\text{ref}})/c_v(T_{\text{ref}})$ the heat capacity ratio. The low Mach number equations are derived by expanding the non-dimensional flow variables as power series in $\varepsilon = \gamma M^2 \ll 1$ The expansions read:

$$\rho = \rho^0 + \varepsilon\rho^1 + \mathcal{O}(\varepsilon^2) \tag{2.28}$$
$$u_i = u_i^0 + \varepsilon u_i^1 + \mathcal{O}(\varepsilon^2) \tag{2.29}$$
$$T = T^0 + \varepsilon T^1 + \mathcal{O}(\varepsilon^2) \tag{2.30}$$
$$Y_k = Y_k^0 + \varepsilon Y_k^1 + \mathcal{O}(\varepsilon^2) \tag{2.31}$$
$$h = h^0 + \varepsilon h^1 + \mathcal{O}(\varepsilon^2) \tag{2.32}$$
$$p = \frac{\rho T}{\gamma M^2} = \frac{1}{\varepsilon} p^0 + p^1 + \mathcal{O}(\varepsilon) \tag{2.33}$$

Pressure is now divided into two parts: (i) the thermodynamic pressure p^0 and (ii) the dynamic pressure p^1. Since $\varepsilon = \gamma M^2 \ll 1$, the pressure in the material derivative term of the energy equation is mainly the thermodynamic pressure p^0. In addition, the spatially uniform nature of p^0 means that the pressure in the gradient term of the momentum equation is only the dynamic pressure p^1. Under the low Mach assumption, enthalpy loss due to viscous stress can be neglected [**110**, **123**]. The non-dimensional momentum and enthalpy equations without heat source terms now read:

$$\frac{\partial \rho^0 u_j^0}{\partial t} + \frac{\partial \rho^0 u_i^0 u_j^0}{\partial x_i} = -\frac{\partial p^1}{\partial x_j} + \frac{1}{Re}\frac{\partial \tau_{ij}^0}{\partial x_i} + \rho^0 \sum_{k=1}^{N} Y_k^0 f_{k,j} \tag{2.34}$$

$$\frac{\partial \rho^0 h^0}{\partial t} + \frac{\partial \rho^0 u_i^0 h^0}{\partial x_i} = \frac{dp^0}{\partial t} - \frac{1}{Re\, Pr}\frac{\partial}{\partial x_i}\left(\lambda \frac{\partial T^0}{\partial x_i}\right) \tag{2.35}$$

The thermodynamic pressure p^0 is constant in space, but not necessarily in time. If the computational domain is open to the atmosphere, then p^0 is constant both in time and space [**145**]. In the absence of external heat sources or sinks, deflagration is an adiabatic process. In this process, part of the reactants' formation enthalpy converts into higher sensible enthalpy of the products. For this reason, there is no source term in the absolute enthalpy equation:

$$\frac{\partial \rho h^0}{\partial t} + \frac{\partial \rho u_i^0 h^0}{\partial x_i} = -\frac{1}{Re\, Pr}\frac{\partial}{\partial x_i}\left(\lambda \frac{\partial T^0}{\partial x_i}\right) \tag{2.36}$$

The system is closed using the ideal gas law, obtained by inserting the expansion for ρ and T into the expansion of p:

$$\rho^0 = \frac{p^0}{T^0} \tag{2.37}$$

Density changes are therefore due only to temperature changes [123].

2.4 Non-premixed combustion

In most combustion systems, fuel and oxidizer streams are initially separated, either by design or by the nature of the process. When mixing between them is slower than chemical reactions, combustion is restricted to thin reaction zones located between the two streams [78]. A schematic of a counterflow diffusion flame configuration is illustrated in Fig. 2.1. A non-premixed flame therefore consists of three distinct regions: a fuel-rich zone, an oxidizer-rich zone, and a narrow reaction layer between them. As fuel and oxidizer move toward each other through molecular diffusion and convective transport, they are heated and eventually mix within this layer, where rapid reactions take place. The resulting combustion products and the heat released are then transported away from the reaction zone in both directions [78].

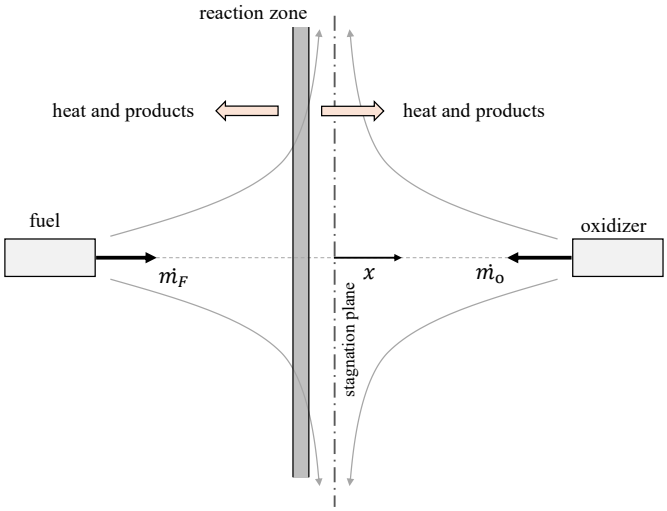

Figure 2.1: Schematic diagram of the counterflow diffusion flame configuration.

In real flames, reactions proceed at finite rates and the reaction zone has finite thickness, so complete consumption of reactants is not achieved. In many analyses, however, it is convenient to assume infinitely fast chemistry and treat the flame as an idealized reaction sheet. Under this assumption, fuel remains on the fuel side and oxidizer on the oxidizer side, both reaching zero concentration exactly at the sheet, so no unreacted species cross it [146]. The reaction sheet then acts as a sink for fuel and oxidizer and a source of heat and products. Combustion is governed by the rates at which reactants are transported to the sheet in stoichiometric proportions, which

also determine the heat release rate. In this limit, diffusion processes dominate over chemical kinetics, and flame properties can be predicted from transport and stoichiometry alone, without detailed reaction mechanisms. This diffusion-controlled limit is the classical Burke–Schumann regime, and the corresponding configurations are known as diffusion flames [146, 147].

2.4.1 Key parameters of non-premixed flames

In non-premixed flames, two parameters are crucial to describe the flame structure:

1. **Mixture fraction**:
   that measures the local fuel–oxidizer ratio. In its simplest form, it can be written as
   $$z = \frac{sY_F - Y_O + Y_O^2}{sY_F^1 + Y_O^2} \tag{2.38}$$
   where the subscripts F and O refer to fuel and oxidizer mass fractions, and the superscripts 1 and 2 denote the values in the fuel and oxidizer streams, respectively. The mixture fraction is zero in the pure oxidizer stream and one in the pure fuel stream. It can be interpreted as the fraction of mass locally originating from the fuel stream compared to the total mass, i.e. $z = \dot{m}_F/(\dot{m}_F + \dot{m}_O)$. A more general formulation was proposed by Bilger and is based on elemental mass fractions [148]:
   $$z = \frac{2\frac{Z_C}{W_C} + \frac{1}{2}\frac{Z_H}{W_H} + \frac{Z_O^2 - Z_O}{W_O}}{2\frac{Z_C^1}{W_C} + \frac{1}{2}\frac{Z_H^1}{W_H} + \frac{Z_O^2}{W_C}} \tag{2.39}$$
   where the elemental mass fraction of element j is defined as
   $$Z_j = W_j \sum_{k=1}^{N_s} \frac{a_{kj} Y_k}{W_k}, \tag{2.40}$$
   with W_j the molecular weight of element j, W_k the molecular weight of species k, and a_{kj} the number of atoms of element j in species k. The mixture fraction is often called a *passive scalar*, since its transport equation contains no chemical source term:
   $$\frac{\partial \rho z}{\partial t} + \frac{\partial \rho u_i z}{\partial x_i} = \frac{\partial}{\partial x_i}\left(\rho D_z \frac{\partial z}{\partial x_i}\right) \tag{2.41}$$
   Equation (2.41) holds under the assumption of unity Lewis number. In that case, the mixture fraction is conserved along the streamlines and remains independent of the progress variable c. For mixtures that contain hydrogen, where the unity Lewis number assumption is not valid, mixture fraction and progress variable become coupled and both transport equations must be corrected accordingly.

2. **Scalar dissipation rate**:
   which controls the mixing between fuel and oxidizer. It measures the local gradients of mixture fraction and the associated molecular diffusion:

$$\chi = 2D \left(\frac{\partial z}{\partial x_i} \frac{\partial z}{\partial x_i} \right) \tag{2.42}$$

   where D is an effective diffusion coefficient. The scalar dissipation rate increases with strain rate and quantifies the intensity of mixing at the flame, since large χ corresponds to strong mixture fraction gradients and enhanced molecular transport [123].

2.5 Premixed combustion

Premixed combustion occurs when fuel and oxidizer are perfectly mixed before ignition. One-dimensional laminar premixed flames are particularly important since they can be used to validate chemical mechanisms, study flame instabilities, and provide the basis for turbulent flame models such as the flamelet concept [123].
Figure 2.2 shows a schematic of a 1-D premixed flame together with its numerical solution (computed with Cantera [149]). Reactants enter from the left with velocity $u = s_L$, equal to the laminar flame speed. The reaction zone has thickness δ_L, where combustion takes place, and downstream of this zone fully burnt products are found. In the numerical solution, only fuel and oxidizer are present ahead of the reaction zone, and they are convected toward the flame by the flow. Within the reaction zone, both fuel and oxidizer are consumed, and the resulting strong gradients drive diffusive fluxes of fresh reactants into the flame. A similar behavior is observed for temperature and major products (e.g. CO_2): the temperature is low in the reactants and rises steeply across the flame due to heat release, while heat conduction transports energy upstream and helps to preheat the reactants. Radical diffusion and thermal conduction together shape the preheat zone structure. Once the ignition temperature is reached, reactions start and the flame propagates. In the downstream equilibrium zone, all fuel is consumed. For the lean methane–air mixture considered here, a finite amount of oxygen remains in the burnt gases because it is present in excess relative to the fuel.

2.5.1 Key parameters of premixed flames

Premixed flames are described by a set of key parameters that characterize their behavior and structure. These are:

- **Progress variable**:
  The completion of the chemical reaction that transforms reactants into prod-

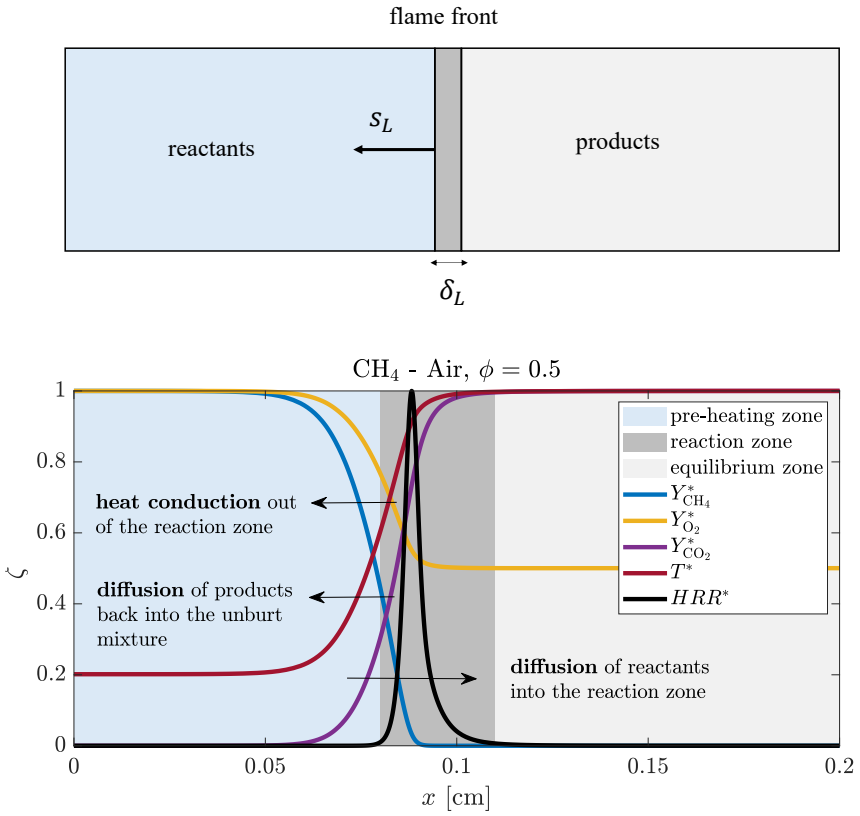

Figure 2.2: Schematic representation of a one-dimensional laminar premixed flame (top) alongside the numerical solution for a lean methane-air mixture computed using Cantera (bottom), with all variables normalized by their maximum values.

ucts can be described by a *progress variable*. In premixed flames, thermochemical variables are strongly correlated and can be expressed as functions of this progress variable. Under the assumption of unity Lewis number ($Le = 1$), the progress variable can be defined either in terms of temperature:

$$\theta = \frac{T - T^u}{T^b - T^u} \tag{2.43}$$

or in terms of a mass fraction, with the specific choice depending on the problem [123]:

$$c = \frac{Y_k - Y_k^u}{Y_k^b - Y_k^u} \tag{2.44}$$

where in both Eq. (2.43) and (2.44) the superscripts u and b refer to unburnt and burnt conditions, respectively.

- **Flame speed**:
  The flame speed is a central parameter in premixed combustion. The laminar flame speed s_L is the velocity at which a planar, one-dimensional flame propa-

gates towards the reactants, in the direction normal to the flame front. Defining the flame speed is not unique, and several equivalent definitions are used in the literature [123, 150, 151]. Three common definitions are:

1. **Absolute speed**, which is in the normal direction component:

$$s_a = \vec{w} \cdot \vec{n} = \frac{1}{|\nabla c|}\left(\frac{\partial c}{\partial t}\right) \tag{2.45}$$

   where $\vec{w}$ is the flame front speed and $\vec{n} = -\nabla c/|\nabla c|$ is the unit normal to the flame front pointing toward the burnt products.

2. **Displacement speed**, which measures the front speed relative to the flow:

$$s_d = (\vec{w} - \vec{u}) \cdot \vec{n} = \frac{1}{|\nabla c|}\left(\frac{\partial c}{\partial t} + \vec{u} \cdot \nabla c\right) \tag{2.46}$$

3. **Consumption speed**, which measures the rate at which the flame consumes reactants:

$$s_c = -\frac{1}{\rho^u Y_F^u}\int_{-\infty}^{+\infty} \dot{\omega}_F \, dn \tag{2.47}$$

   where ρ^u and Y_F^u are the density and fuel mass fraction on the unburnt side, and $\dot{\omega}_F$ is the fuel reaction rate.

- **Flame thickness**:
  Estimating a flame thickness is important in numerical simulations, because it helps to set the minimum mesh resolution needed to resolve the flame structure. There are different ways to define the premixed flame thickness:

  - A scaling law based on thermal diffusion and flame speed [78]:

$$\delta = \frac{\lambda}{\rho^u C_p s_L} = \frac{D^{T,u}}{s_L} \tag{2.48}$$

    where $D^{T,u}$ is the thermal diffusivity of the fresh gases. This approach often underestimates the actual thickness by a factor of about five [123].

  - A definition based on the temperature profile:

$$\delta_L = \frac{T^b - T^u}{\max\left|\frac{\partial T}{\partial x}\right|} \tag{2.49}$$

    which measures the ratio between the total temperature rise and the maximum temperature gradient in the flame. Fig. 2.3 shows graphically how the flame thickness is calculated using this approach. It can also be noted that, for the same equivalence ratio, the flame thickness of a premixed hydrogen–air mixture is much smaller than that of a methane–air mixture.

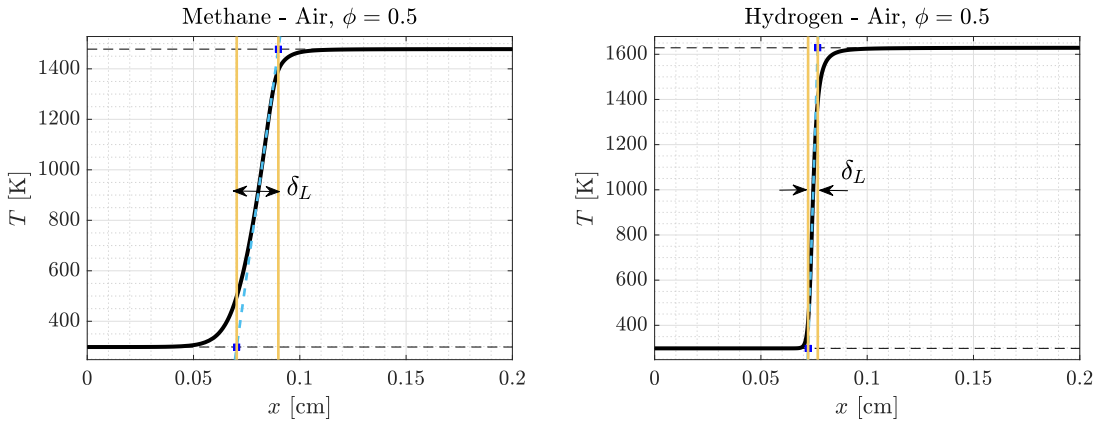

Figure 2.3: One-dimensional Cantera simulations of lean methane-air (left) and hydrogen-air (right) premixed flames, with laminar flame thickness δ_L determined from the temperature gradient.

2.5.2 Stretch effects

To study multi-dimensional flames, additional parameters must be introduced. One of these is the *flame stretch*, which represents the rate of change of a flame surface element A [152, 153]:

$$K = \frac{1}{A}\frac{dA}{dt} \tag{2.50}$$

Stretch effects can be written as the sum of two contributions: (i) *strain* effects, due to flow non uniformity along the flame surface, and (ii) *curvature* effects, due to the change of area caused by the curvature of the flame front. Flame stretch can then be expressed as

$$K = K_s + \kappa\, s_d = -\vec{n}\cdot\nabla\vec{w}\cdot\vec{n} + \nabla\cdot\vec{w} \tag{2.51}$$

where K_s is the tangential strain rate, κ the flame curvature, s_d the displacement flame speed, and $\vec{w}$ the flame front velocity. Equation (2.51) can be modified by using $\vec{w} = \vec{u} + s_d\vec{n}$. Following [123], we obtain:

$$K = \underbrace{-\vec{n}\cdot\nabla\vec{u}\cdot\vec{n} + \nabla\cdot\vec{u}}_{\text{strain}} + \underbrace{s_d\nabla\cdot\vec{n}}_{\text{curvature}} = \nabla_t\cdot\vec{u} + s_d\nabla_t\cdot\vec{n} \tag{2.52}$$

Flame stretch effects are important because stretch can influence flame temperature and burning rate. This happens through velocity gradients along the flame surface, which modify enthalpy and mixture fraction distributions [78]. The reaction rate and temperature may decrease or increase depending on the Lewis number. As shown in Fig. 2.4, if $Le > 1$ there is a critical stretch rate at which the burnt gas temperature T_b is reduced so much that burning is no longer possible. Extinction then occurs when the flame, if unrestrained, stands at a finite distance from the stagnation surface [78]. For $Le < 1$, increasing stretch raises T_b, so extinction cannot occur until the downstream boundary of the reaction zone reaches the stagnation surface and the flame

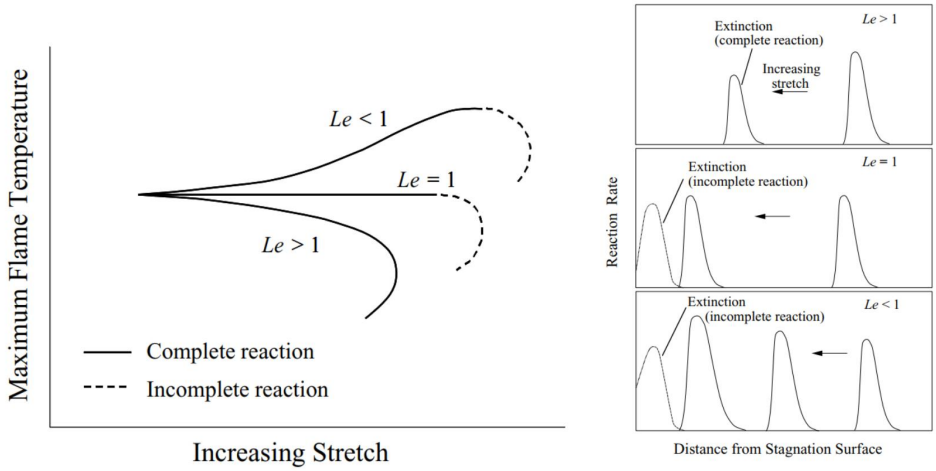

Figure 2.4: Influence of increasing stretch rate on maximum flame temperature (left) and reaction rates (right) for fuels with different Lewis numbers from [78].

motion becomes constrained. With further stretch, the residence time becomes too short to complete the reaction, and the reaction rate and flame temperature start to decrease, eventually leading to extinction [78]. For the diffusionally neutral case $Le = 1$, the flame temperature and reaction rate stay almost unchanged until the reaction zone touches the surface, after which incomplete reaction and extinction follow as the stretch rate increases [78]. When a flame is stretched, its flame speed can differ from that of an unstretched flame. The flame speed can then be written as

$$s_K = s_L - \mathcal{L}K \tag{2.53}$$

where $\mathcal{L}$ is the Markstein length [154, 155], a coefficient that measures the sensitivity of the flame speed to stretch. Negative values of $\mathcal{L}$ cause regions curving into the reactants ($\kappa > 0$) to propagate faster than the laminar flame, while regions curving into the products ($\kappa < 0$) propagate slower. In this case, initial perturbations of the flame surface grow and increase the local curvature, which leads to an instability, as observed for lean hydrogen–air flames [156]. Markstein lengths and unstretched flame speeds can be determined experimentally using spherically expanding flames. In this configuration, as the flame radius R increases, optical diagnostics provide the instantaneous flame speed and stretch rate, where $K = (2/R)\,dR/dt$ for a spherical flame. Other experimental techniques include (i) *stagnation point flames*, (ii) *flame tips*, and (iii) *spherical flames* [123].

Figure 2.5 shows Markstein lengths of different types of fuels and for premixed combustion of methane-hydrogen blends with air, for different hydrogen contents and equivalence ratios [25]. When the hydrogen content is high and the equivalence ratio is low the Markstein length becomes negative. This behavior is due to the high

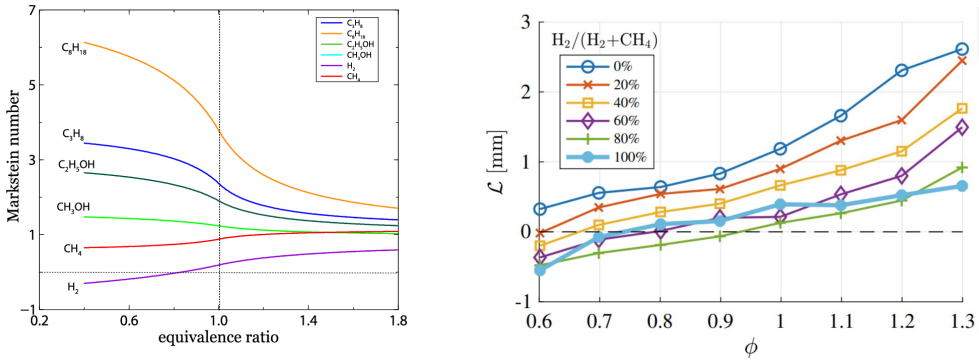

Figure 2.5: Markstein length versus equivalence ratio for various fuels (left) reprinted from[157] and hydrogen/methane-air blends (right) from [25].

molecular diffusivity of hydrogen. At the same time, accurate measurement of Markstein lengths is challenging, and the different methods mentioned above can give slightly different values [156].

2.5.3 Intrinsic flame instabilities

Laminar premixed flames can develop intrinsic instabilities at the flame front. Two main types are usually distinguished:

1. **Hydrodynamic instabilities:**
   These instabilities, also known as *Darrieus–Landau (DL) instabilities*, are caused by the density jump across the flame front [158]. The flow normal to the flame is accelerated by an amount $u_b - u_u = (\sigma - 1)s_L$, where u_b and u_u are the velocities of the burnt and unburnt gases, respectively, and $\sigma = \rho_b/\rho_u$ is the expansion ratio [157].

   The mechanism behind the DL instability is sketched in Fig. 2.6. Fresh gases enter the domain with a velocity $u_u \approx s_L$. A small perturbation of wavelength λ appears on the flame front. Across the flame, the tangential component of the flow velocity is conserved, while the normal component increases. This difference produces local acceleration or deceleration along the front and amplifies the initial perturbation for essentially all wavelengths [156].

2. **Thermodiffusive instabilities:**
   Laminar premixed flames can also exhibit *thermodiffusive* (TD) instabilities, controlled by the balance between molecular diffusion of reactants and heat diffusion [21, 157]. TD instabilities are observed, for example, in lean hydrogen–air flames, where they lead to cellular flame structures. From a physical point of view, they can be interpreted in terms of transverse diffusive fluxes of heat and reactants in a curved flame [159].

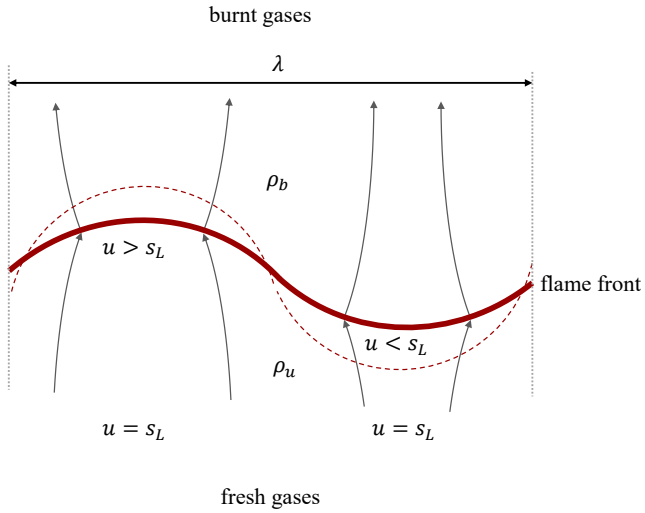

Figure 2.6: Schematic of the Darrieus-Landau (DL) instabilities mechanism. Reproduced from [156].

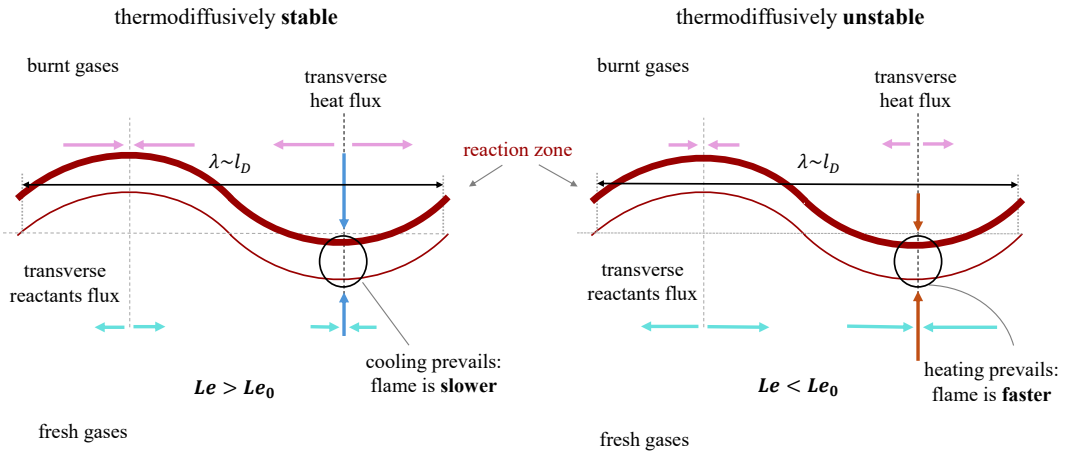

Figure 2.7: Illustration of thermodiffusive (TD) instabilities in a stable case ($Le > Le_0$) on the left and unstable ($Le < Le_0$) on the right. Reproduced from [156].

If the flame is curved, diffusive fluxes normal to the flame surface can be decomposed into longitudinal and transverse contributions. The longitudinal fluxes control the one-dimensional preheat zone, while the transverse fluxes, absent in a planar flame, grow with curvature as l_D/λ increases, where l_D is a characteristic diffusion length and λ the perturbation wavelength [156]. As sketched in Fig. 2.7, in a region convex towards the fresh mixture, the transverse heat flux tends to cool the reaction zone, whereas the transverse reactant flux tends to enrich it with fresh reactant. Depending on the Lewis number, one of these effects dominates. For $Le < Le_0$, the supply of fresh reactant is more effective than heat loss, which increases the local flame speed and amplifies the perturbation, leading to an instability.

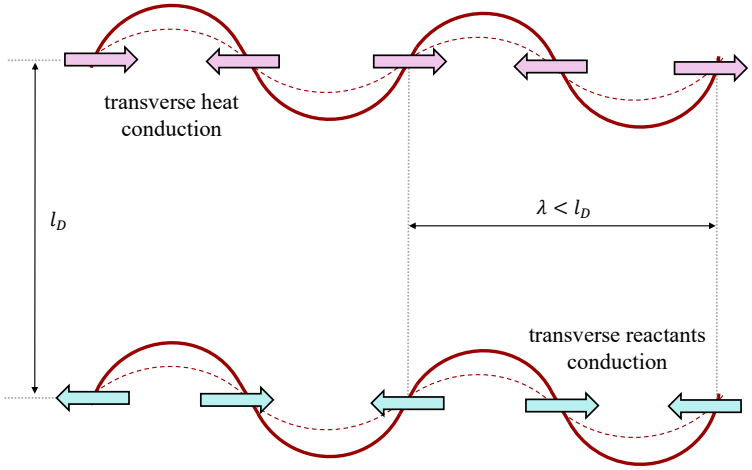

Figure 2.8: Stabilizing mechanism of instabilities for very low perturbation wavelengths. Reproduced from [156].

The thermodiffusive mechanism does not grow indefinitely as the wavelength decreases. For $\lambda < l_D$, the local transverse gradients of temperature and species become very large, which enhances transverse heat conduction and reactant diffusion. This effect damps the perturbation for any Lewis number, as sketched in Fig. 2.8. In this regime, transverse fluxes of fresh reactant can no longer sustain the reaction zone, and the thermodiffusive driving mechanism becomes ineffective [156].

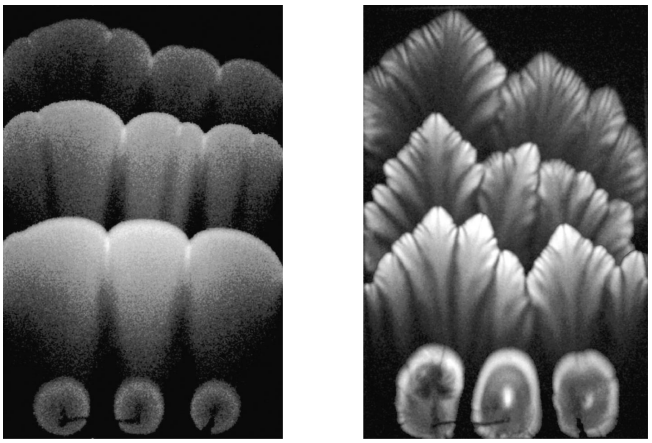

Figure 2.9: Sequences of images showing propagating flames in a Hele-Shaw cell for H_2-O_2-N_2 mixtures with different Lewis numbers: rich mixture ($Le \approx 1.6$) on the left and lean mixture ($Le \approx 0.34$) on the right from [160]

A visualization of hydrodynamic and thermodiffusive instabilities is shown in Fig. 2.9. These instabilities were observed in Hele-Shaw cells [160]. In these cells, flames

propagate between two parallel glass plates separated by a narrow gap. This setup creates a quasi two-dimensional configuration.
Figure 2.9.a shows a rich H_2–O_2–N_2 mixture where oxygen is the deficient reactant. The effective Lewis number is $Le \approx 1.6$. The flame shows large-scale cusps typical of hydrodynamic instability. No small-scale thermodiffusive wrinkling appears due to the high Lewis number [160]. In contrast, Fig. 2.9.b shows a lean H_2–O_2–N_2 mixture where hydrogen is the deficient reactant. Here the Lewis number is $Le \approx 0.34$. Thermodiffusive instabilities are clearly visible as small-scale wrinkling on top of large-scale flame fingers pointing towards the fresh mixture. Small extinction zones appear where the flame is concave towards the fresh gases. Conversely, where the flame is convex towards the fresh gases, brighter zones indicate higher reactivity due to better fuel supply to the reaction zone [160].

2.6 Turbulent combustion

Most flows in practical combustion devices are turbulent, characterized by the presence of rapid, random fluctuations of the flow velocity and scalar properties at a given point in space. Turbulence remains one of the most challenging and unsolved problems in physics. The complexity further increases when chemical reactions are also present. In the presence of chemical reactions, the complexity of turbulent flows takes on a new dimension. Turbulence is expected to generally increase the burning intensity by enhancing the mixing of reactants, the transport of heat and the flame front wrinkling and, hence, increasing the total flame surface area available for reaction to take place [123, 161]. Excessively intense turbulent eddies, however, can also cause local extinction in a turbulent flow, thereby adversely affecting the combustion efficiency [78]. Studying and modeling turbulent combustion processes is, therefore, an important issue to develop and improve practical systems. As combustion processes are difficult to handle using analytical techniques, numerical combustion for turbulent flames is a fast growing area. But numerical simulations of turbulent reacting flows remain complex because of (i) the different chemical time and length scales involved, (ii) the description of turbulence itself and (iii) the coupling between the latter and chemistry [123].

2.6.1 Turbulent premixed flames

In turbulent premixed combustion, as in the laminar case, fuel and oxidizer mix at the molecular level prior to ignition. However, the incoming flow is turbulent and the turbulent structures can wrinkle the flame front, thus increasing its surface area and global consumption rate. Unlike laminar flames, turbulent flames are characterized by a turbulent flame speed s_T and thickness δ_T, both distinct from laminar values.
Figure 2.10 illustrates a typical turbulent premixed flame. The turbulent flame speed

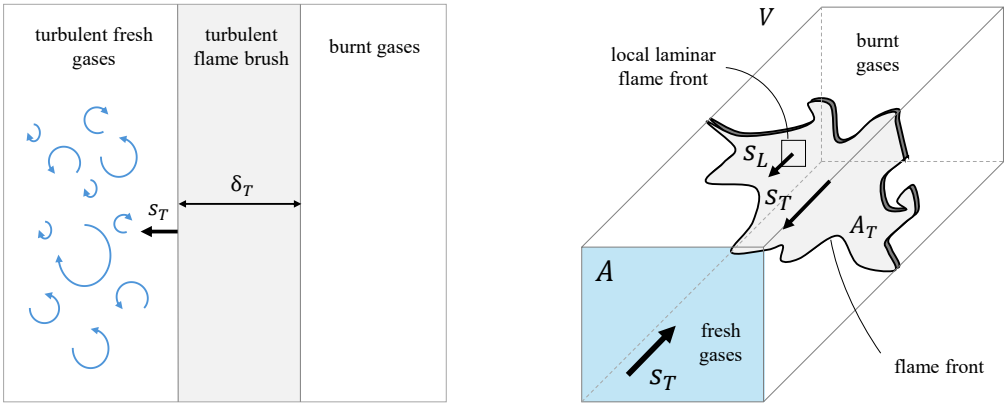

Figure 2.10: Schematic of turbulent premixed flame wrinkling.

follows from conservation of mass flux across the flame surface:

$$s_T = \frac{A_T}{A} s_L = \Theta s_L \tag{2.54}$$

where $\Theta = A_T/A$ represents the flame wrinkling factor, i.e., the ratio of actual flame surface area A_T to reference cross-sectional area A. This area increase due to turbulent wrinkling directly explains the enhanced burning rate. Generally, Θ grows with Reynolds number [162, 163], though limited by eventual quenching at extreme conditions where accurate prediction becomes challenging. In particular, combustion also modifies turbulence: the increase in temperature increases kinematic viscosity, potentially causing flow relaminarization [164], while density and velocity gradients across the flame generate vorticity [123].

2.6.2 Combustion regimes

The combustion behavior varies widely depending on the characteristic time and length scales of the process. Combustion models must therefore account for the different regimes that can occur. Turbulent combustion diagrams are commonly used to classify these regimes. These diagrams employ dimensionless numbers formed as ratios of turbulent and chemical scales and rely on rough estimates rather than exact derivations. The construction also depends on simplifying assumptions about turbulence, including (i) statistical homogeneity and isotropy, and (ii) representation of turbulence by a single root-mean-square (RMS) velocity fluctuation u' and integral length scale l_t. Under these assumptions, two key dimensionless numbers emerge:

- **Damköhler number**:
  The Damköhler number represents the ratio between the integral turbulent

time scale τ_t and the chemical time scale τ_c:

$$Da = \frac{\tau_t}{\tau_c} = \frac{l_t/u'(l_t)}{\delta/s_L} \tag{2.55}$$

Here, Da is defined for the largest eddies in the flow.

- **Karlovitz number**:
  The Karlovitz number represents the ratio between the chemical time scale τ_c and the Kolmogorov time scale τ_k:

$$Ka = \frac{1}{Da(\eta_k)} = \frac{\tau_c}{\tau_k} = \frac{u'(\eta_k)/\eta_k}{s_L/\delta} \tag{2.56}$$

  where η_k is the Kolmogorov length scale, and $Da(\eta_k)$ is the Damköhler number defined at the Kolmogorov scale.

Once these dimensionless numbers are defined, combustion regime diagrams can be introduced. The Borghi-Peters diagram [122] in Fig. 2.11 identifies several regimes:

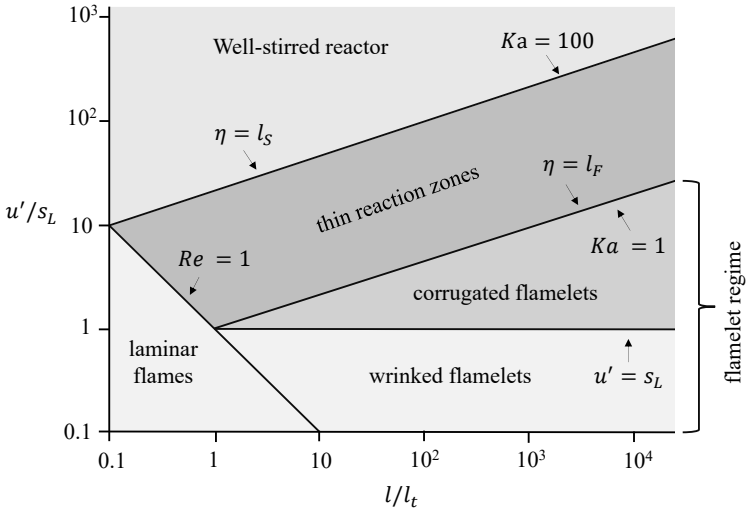

Figure 2.11: Borghi-Peters diagram of turbulent combustion regimes. Reproduced from [122].

- **Flamelet regime**:
  For $Ka < 1$ and $Da > 1$, the flame thickness is smaller than all relevant turbulent length scales. In this case, turbulence cannot alter the internal flame structure, and the flame behaves as an ensemble of laminar flamelets. Two sub-regimes can be distinguished:

  - **Wrinkled flamelet regime**, where $u' < s_L$. Turbulent motions can wrinkle the flame front but cannot cause strong flame front interactions.

  - **Corrugated flamelet regime**, where $u' > s_L$. Turbulence is strong enough to wrinkle the front and to induce interactions between flame sheets, which can create pockets of fresh and burnt gases.

- **Thin reaction zones**:
  This regime corresponds roughly to $1 < Ka \leq 100$. The smallest turbulent scales can modify the preheat zone and part of the flame structure. However, the inner reaction zone remains thicker than the Kolmogorov scale and is not fully disrupted.

- **Well-stirred reactor zone**:
  For $Da < 1$ and $Ka > 100$, turbulent mixing is very fast compared to chemistry. The mixture is nearly homogeneous at the smallest scales, and the overall reaction rate is limited by chemical kinetics rather than by transport. Here, eddies can penetrate the reaction zone modifying chemistry and mixing and, if mixing is too fast, local extinctions can occur.

2.7 Modeling

Engineering flows become unstable when the Reynolds number exceeds a critical value ($Re = UL/\nu$, where U and L represent characteristic velocity and length scales of the mean flow, and ν is kinematic viscosity). Below this threshold, the flow remains laminar. Above it, the flow becomes turbulent, characterized by chaotic motion and continuous velocity and pressure fluctuations throughout the domain. Accurate turbulence modeling is fundamental in computational fluid dynamics (CFD), as it directly determines the reliability of simulation results.

2.7.1 Turbulence modeling

The effect of turbulence is to bring fluid particles closer and enhance mass and momentum exchange. A schematic view of turbulence is shown in Fig. 2.12. The largest eddies extract energy from the mean flow, where inertial forces dominate over viscous forces. Their energy is then transferred to smaller and smaller eddies, until it is finally converted into thermal energy by viscous dissipation. The ratio between large and small scales is known as scale separation and increases with the Reynolds number of the flow.
To simulate a turbulent flow numerically, all scales from largest to smallest would need to be resolved in principle. In practice, computational constraints lead to different modeling strategies that resolve part of the spectrum and model the rest. Three primary approaches exist:

- **Direct Numerical Simulation (DNS):**
  The full instantaneous Navier–Stokes equations are solved without any turbu-

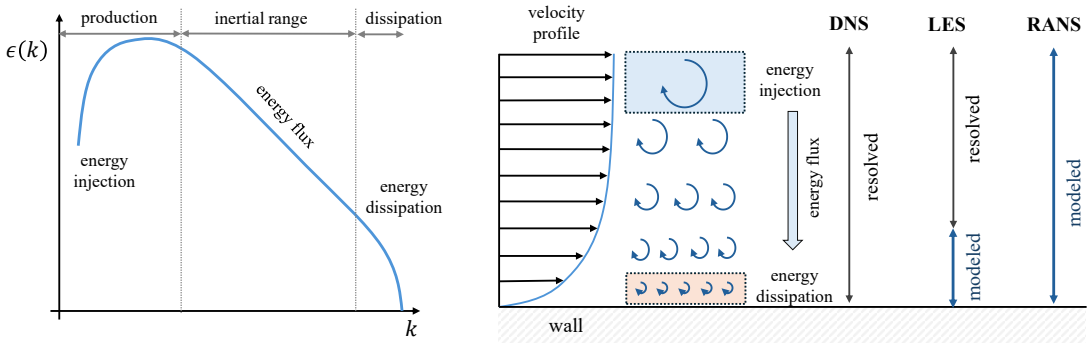

Figure 2.12: Turbulent kinetic energy spectrum (left) and schematic of turbulence modeling techniques (right).

lence model. Since no additional modeling assumptions are required, DNS provides the most accurate and detailed description of the flow. Its main limitation is the very high computational cost ($\propto Re^3$) and the large amount of data generated. As a result, DNS is restricted to simple, academic configurations, for example combustion in small canonical domains.

- **Reynolds-Averaged Navier–Stokes (RANS):**
  The governing equations are averaged and solved for the mean flow. Instantaneous quantities are decomposed using a Reynolds decomposition into a mean part and a fluctuating part: $\zeta(t) = \overline{\zeta}(t) + \zeta'(t)$, where the mean value is constant in time. The influence of turbulence on momentum and scalar transport is introduced through turbulence models. Unsteady RANS (URANS) extends this approach by allowing time-dependent variations of the mean fields. Thanks to their relatively low computational cost and the ability to reproduce the main flow features when properly calibrated, RANS models are widely used in engineering design. However, they rely on empirical closures and may fail to capture important details of complex turbulent flows, especially in reacting flows.

- **Large Eddy Simulation (LES):**
  A spatial filter is applied to the equations so that the large, energy-containing eddies are resolved directly, while the smaller scales are modeled. The subfilter scales are described using general assumptions about the behavior of small eddies, which are more universal and dominated by higher frequencies. LES is the approach adopted in this dissertation and will be discussed in more detail in the next section.

2.7.2 Large Eddy Simulation

In large eddy simulation, a low-pass filter is applied to the instantaneous Navier–Stokes equations, allowing the velocity field to be computed on a relatively coarse computational grid. The general form of the filtering operation is expressed as:

$$\overline{\zeta}(x,t) = \int_{-\infty}^{+\infty} \zeta(x',t)\, G(x-x';\Delta)\, dx' \tag{2.57}$$

where G denotes the filter kernel that satisfies the normalization condition $\int_{-\infty}^{+\infty} G(x-x';\Delta)\, dx' = 1$ [**114**]. This filtering process can be interpreted as a weighted spatial averaging, where the shape of the kernel defines the weighting distribution and its characteristic width determines the averaging scale. The chosen filter width strongly influences the fidelity of LES, as it dictates which turbulent scales are explicitly resolved and which are represented by a subgrid model. Various filter functions have been proposed, and their characteristics are well documented in the literature [**114**]. Two common filters are the Gaussian filter:

$$G(x-x') = \left(\frac{6}{\pi\Delta^2}\right)^{1/2} \exp\left(-\frac{6(x-x')^2}{\Delta^2}\right) \tag{2.58}$$

which peaks at $x' = x$ and decays rapidly with $|x-x'|$, and the box filter:

$$G(x-x') = \begin{cases} \frac{1}{\Delta^3}, & \text{if} \quad |x-x'| < \frac{\Delta}{2} \\ 0, & \text{otherwise} \end{cases} \tag{2.59}$$

which assumes a uniform value within a box of size Δ and drops sharply to zero for $|x-x'| > \Delta/2$. Density variations in the unresolved scales due to combustion are treated using the Favre (density-weighted) filtering [**165**]:

$$\widetilde{\zeta}(x,t) = \frac{\overline{\rho\,\zeta}(x,t)}{\overline{\rho}} \tag{2.60}$$

The instantaneous quantities $\zeta(x,t)$ are now decomposed into a resolved filtered mean $\widetilde{\zeta}(x,t)$ and an unresolved subgrid-scale fluctuation $\zeta''(x,t)$:

$$\zeta(x,t) = \widetilde{\zeta}(x,t) + \zeta''(x,t) \tag{2.61}$$

This decomposition resembles Reynolds averaging, though $\widetilde{\zeta}(x,t)$ represents a filtered random field, and the filtered fluctuation $\overline{\zeta''}(x,t)$ does not vanish in general. Applying the Favre filtering to the Navier–Stokes equations yields the LES governing equations:

$$\frac{\partial\overline{\rho}}{\partial t} + \frac{\partial\overline{\rho}\widetilde{u}_i}{\partial x_i} = 0 \tag{2.62}$$

$$\frac{\partial \overline{\rho}\widetilde{u_j}}{\partial t} + \frac{\partial \overline{\rho}\widetilde{u_i}\widetilde{u_j}}{\partial x_i} = -\frac{\partial \overline{p}}{\partial x_j} + \frac{\partial}{\partial x_i}\left[\overline{\tau}_{ij} - \overline{\rho}(\widetilde{u_i u_j} - \widetilde{u_i}\widetilde{u_j})\right] \tag{2.63}$$

$$\frac{\partial \overline{\rho}\widetilde{Y_k}}{\partial t} + \frac{\partial \overline{\rho}\widetilde{u_i}\widetilde{Y_k}}{\partial x_i} = \frac{\partial}{\partial x_i}\left[\overline{\rho}\widetilde{D}_k\frac{\partial \widetilde{Y_k}}{\partial x_i} - \overline{\rho}(\widetilde{u_i Y_k} - \widetilde{u_i}\widetilde{Y_k})\right] + \overline{\dot{\omega}}_k \tag{2.64}$$

$$\frac{\partial \overline{\rho}\widetilde{h}}{\partial t} + \frac{\partial \overline{\rho}\widetilde{u_i}\widetilde{h}}{\partial x_i} = -\frac{\partial}{\partial x_i}\left[\overline{\rho}\frac{\widetilde{\nu}}{Pr}\frac{\partial \widetilde{h}}{\partial x_i} + \overline{\rho}(\widetilde{u_i h} - \widetilde{u_i}\widetilde{h})\right] \tag{2.65}$$

Equation (2.65) assumes low-Mach number conditions and neglects radiation effects. The residual stress tensor τ_{ij}^r in the momentum equation is modeled via the eddy-viscosity approach, similar to RANS, but employing a subgrid-scale viscosity ν_{sgs}:

$$\widetilde{\tau}_{ij}^R = -\overline{\rho}(\widetilde{u_i u_j} - \widetilde{u_i}\widetilde{u_j}) = \frac{1}{3}\widetilde{\tau}_{kk}^R\delta_{ij} + \widetilde{\tau}_{ij}^r = -2\overline{\rho}\nu_{sgs}\left(\frac{1}{3}\widetilde{S}_{kk}\delta_{ij} - \widetilde{S}_{ij}\right) \tag{2.66}$$

The anisotropic component $\widetilde{\tau}_{ij}^r$ is typically represented using the Smagorinsky model [118, 166] or a transport equation for subgrid kinetic energy [167, 168]. Filtered diffusion fluxes of species and enthalpy are approximated as:

$$\overline{\rho D_\zeta \frac{\partial \zeta}{\partial x_i}} \approx \overline{\rho}\widetilde{D_\zeta}\frac{\partial \widetilde{\zeta}}{\partial x_i} \tag{2.67}$$

Subgrid turbulent fluxes follow the gradient-diffusion hypothesis:

$$\overline{\rho}(\widetilde{u_i\zeta} - \widetilde{u_i}\widetilde{\zeta}) = -D_{\zeta,t}\frac{\partial \widetilde{\zeta}}{\partial x_i}, \qquad D_{\zeta,t} = \begin{cases} \frac{\mu_{sgs}}{Sc_t}, & \widetilde{\zeta} = \widetilde{Y_k},\ k = 1, N \\ \frac{\alpha_{sgs}}{Pr_t}, & \widetilde{\zeta} = \widetilde{h} \end{cases} \tag{2.68}$$

where α_{sgs} is the subgrid thermal diffusivity. The turbulent Schmidt number Sc_t and Prandtl number Pr_t are typically near unity, although they can vary with local turbulence levels [169]. The filtered reaction rate $\overline{\dot{\omega}}_k$ appearing in Eq. (2.64) represents a highly nonlinear source term and poses one of the primary challenges in turbulent combustion LES.

2.7.3 Turbulent combustion modeling

In LES, the largest turbulent eddies are explicitly resolved while the smallest scales are modeled. Given that combustion occurs predominantly at the small scales, the flame front lies entirely within the subgrid region. Consequently, all the turbulence-chemistry interactions (TCI) must be represented through subgrid models. Various modeling approaches for premixed combustion have been reviewed and summarized in earlier studies [110, 123]. These approaches can be grouped into two main

classes, namely *geometrical*, which represent the flame as an infinitely thin propagating surface [110, 170], and *statistical* methods that characterize the flame structure by means of probability distributions of the thermochemical states. An overview of several established models within these frameworks is provided below.

- **Eddy Break Up (EBU):**
  This model assumes high Reynolds and Damköhler numbers. The flame front is described as an ensemble of pockets of fresh and burnt gases. The mean reaction rate is controlled by turbulent mixing between reactants and products, using a turbulent mixing time scale $\tau_t = k/\varepsilon$ based on the turbulent kinetic energy k and its dissipation rate ε. The original formulation was developed for RANS [171, 172] and later extended to LES [173, 174] by introducing a subgrid mixing time scale $\tau_{t,sgs} \approx k_{sgs}/\varepsilon_{sgs}$, with $\varepsilon_{sgs} = c_\varepsilon k_{sgs}^{3/2}\Delta$ and c_ε a model constant. In terms of a progress variable, the mean reaction rate can be written as:

$$\overline{\dot{\omega}}_c = -C_{\mathrm{EBU}}\,\overline{\rho}\,\frac{\widetilde{\sigma}_c}{\tau_{t,sgs}} \tag{2.69}$$

  where σ_c is the subgrid variance of the progress variable and C_{EBU} is a model constant, which in LES often depends on flow conditions and grid resolution. The subgrid variance requires modeling. Assuming an infinitely thin flame with infinitely fast chemistry, a bimodal distribution leads to $\widetilde{\sigma}_c = \widetilde{c}(1-\widetilde{c})$. The model is attractive because the reaction rate is expressed as a simple function of mean quantities, without extra transport equations. It is implemented in many commercial CFD codes. A primary limitation of this approach is that chemical kinetics are not explicitly resolved, limiting its applicability to the fast-chemistry regime. Additionally, the model tends to overestimate reaction rates in regions of intense shear and neglects the finite flame thickness [123].

- **Flame surface density (FSD):**
  Under the flamelet assumption, the mean reaction rate is expressed in terms of flame surface area. It is written as the product of the flame surface density Σ and the local consumption rate of flame area, $\rho_0\langle s_c\rangle_s$ [153, 175, 176]:

$$\overline{\dot{\omega}}_c = \rho_0\,\langle s_c\rangle_s\,\Sigma \tag{2.70}$$

  where ρ_0 is the fresh gas density and $\langle s_c\rangle_s$ is the average flame consumption speed along the surface. In this framework, TCI are mainly represented by the flame surface density, while the influence of detailed chemistry is embedded in $\langle s_c\rangle_s$. This separation is a key advantage of the model. The mean flame consumption speed can be obtained from laminar flame calculations and tabulated in a flamelet library. It is often expressed as a function of stretch rate

[177]:

$$\langle s_c \rangle_s = \int_0^{+\infty} s_c(K)\, P(K)\, dK \tag{2.71}$$

where $P(K)$ is the probability density of stretch along the flame surface, which is commonly approximated by a Dirac distribution. The flame surface density can be evaluated from algebraic relations or by solving a transport equation [110, 123, 151].

- **G-equation**:
  In this approach, the flame is treated as an infinitely thin interface that propagates with a prescribed burning velocity. The flame front is tracked using a level-set type transport equation, usually called the G-equation [122, 163]:

$$\frac{\partial \overline{\rho}\, \widetilde{G}}{\partial t} + \frac{\partial \overline{\rho}\, \widetilde{u}_i\, \widetilde{G}}{\partial x_i} = \rho_u\, \overline{s_T} \left| \frac{\partial \overline{G}}{\partial x_i} \right| \tag{2.72}$$

  where s_T is the turbulent flame speed and ρ_u is the unburnt gas density. The turbulent flame speed requires closure and is often modeled as

$$\overline{s_T} = s_L \left[1 + \alpha \left(\frac{\overline{u'_\Delta}}{s_L} \right)^n \right] \tag{2.73}$$

  where α and n are model constants and u'_Δ represents a subgrid scale velocity and can be estimated as $u'_\Delta \approx \Delta |\widetilde{S}| = \Delta \sqrt{|2 \widetilde{S}_{ij} \widetilde{S}_{ij}}$ where $\widetilde{S}_i j$ are the components of the resolved shear stresses . The G-equation approach does not rely on resolving thin flame elements explicitly. Instead, it treats the overall turbulent flame as a propagating surface without computing the detailed internal structure of the flame brush. This framework is particularly suitable for simulating large-scale systems where internal flame details are unnecessary [110, 178]. However, determining the turbulent flame speed $\overline{s_T}$ requires dedicated modeling. In this context, turbulent transport and flame propagation effects can be decoupled to accurately capture how turbulence influences s_d, the instantaneous displacement speed of the premixed flame front [163, 179].

- **Thickened flame model (TFM)**:
  In thickened flame models, the physical flame is artificially thickened while keeping the laminar flame speed unchanged. This allows the flame front to be resolved on coarser grids by introducing a thickening factor F [180]. The species transport equation is modified as:

$$\frac{\partial \rho Y_k}{\partial t} + \frac{\partial \rho u_i Y_k}{\partial x_i} = \frac{\partial}{\partial x_i} \left(\rho E F D_k \frac{\partial Y_k}{\partial x_i} \right) + \frac{E}{F} \dot{\omega}_k \tag{2.74}$$

  where E is an efficiency function computed from a subgrid-scale model. It

compensates for the loss of unresolved flame wrinkling and aims to preserve the correct flame propagation speed. The efficiency function is defined as the ratio between the wrinkling factor of the physical flame and that of the thickened flame, $E = \Theta_{\delta=\delta_l}/\Theta_{\delta=\delta_l F}$. An extension of the TFM where the thickening factor is adapted dynamically based on flow conditions can also be used [181, 182].

- **Filtered tabulated chemistry (FTACLES):**
The method relies on pre-filtered chemistry tables designed to match the LES grid resolution. One-dimensional laminar premixed flames are computed first, then filtered using a Gaussian kernel with width similar to the LES filter [183]. This ensures correct flame propagation speed when no subgrid turbulence is present, making the model consistent with DNS in laminar conditions. For turbulent cases, subgrid flame wrinkling is accounted for using a flame surface density correction that connects the filtered reaction rate to the resolved flame surface.

- **Filtered density function (FDF):**
Unlike geometrical approaches, FDF models adopt a statistical description of the flame. They represent subgrid thermochemical states using probability distributions [110, 123]. Turbulent mixing and flame wrinkling effects are captured through a subgrid filtered density function (FDF). Let $V = (Y_1, ..., Y_N, T)$ denote the local thermochemical state vector. The filtered density function $\overline{P}(V'; x, t)$ gives the probability of finding a specific state V' at position x and time t. The filtered chemical source term is then obtained as:

$$\overline{\dot{\omega}}_k(x,t) = \int_V \dot{\omega}_k(V')\,\overline{P}(V';x,t)\,dV' \tag{2.75}$$

The main challenge lies in determining the shape of $\overline{P}$, which requires modeling. Two main paths have been proposed: to presume the FDF shape or to solve a balance equation for the FDF [184, 185]:

  - **Presumed filtered density function (P-FDF):**
  In this approach, the FDF shape is assumed a priori [141]. A β-function is commonly used as it depends only on the first two statistical moments and can represent various shapes [126]:

$$\overline{P}(V';x,t) = \frac{(V')^{a-1}(1-V')^{b-1}}{\int_0^1 (V'')^{a-1}(1-V'')^{b-1}\,dV''} \tag{2.76}$$

  The shape parameters a and b are computed from the filtered mean $\widetilde{V}$ and

variance $\widetilde{V''^2}$:

$$a = \widetilde{V}\left(\frac{\widetilde{V}(1-\widetilde{V})}{\widetilde{V''^2}} - 1\right), \quad b = a\left(\frac{1}{\widetilde{V}} - 1\right) \tag{2.77}$$

P-FDF methods are typically combined with tabulated chemistry approaches like flamelet models [135]. In these cases, the full thermochemical state V is reduced to two controlling variables (e.g., mixture fraction z and progress variable c). Four statistical moments are then needed: the filtered means and variances of both variables [123]. This approach will be detailed in the next chapter.

- **Transported filtered density function (T-FDF)**:
  Instead of assuming a specific shape for the filtered density function, the T-FDF approach solves a transport equation directly for the FDF [127]. This class of methods represents the subgrid probability distribution using multiple stochastic samples. These samples evolve through modeled stochastic differential equations and represent either local states tracked by Lagrangian particles (LSPM) [114, 184] or Eulerian fields defined on the computational grid (ESF) [186–188]. In this formulation convection and micro-mixing require closure models while the chemical source terms appear in closed form without approximation. Further details on this method are presented in the next chapter.

- **Conditional moment closure (CMC):**
  CMC focuses on specific mixture states rather than the full composition space [189, 190]. In premixed flames, it considers states between fresh gases and burnt products. In non-premixed combustion, it examines states between fuel and oxidiser streams [110]. For diffusion flames, balance equations are derived and solved for conditional species mass fractions $\langle\overline{\rho Y_k}|z'\rangle$, which represent the mean mass fraction of species k conditioned on a specific mixture fraction value $z = z'$ [123]. The unconditional filtered mean is then recovered by integrating over the mixture fraction PDF:

$$\overline{\rho}\,\widetilde{Y}_k = \int_0^1 \langle\overline{\rho Y_k}|z'\rangle\, P(z')\, dz' \tag{2.78}$$

  This method is appealing because it reduces the dimensionality of the chemistry problem. However, it requires closure models for the conditional balance equations. Additionally, equations must be solved for many conditioning values z', which leads to high computational cost [123].

3 Methods

In this chapter the details of the combustion models and subgrid closures employed for the present study are discussed.

3.1 Flamelet-based model

As outlined in the previous chapter, flamelet-based models are applicable when chemical time scales are much shorter than turbulent time scales, so that turbulence is unable to alter the inner flame structure. In this study, we a flamelet model with a presumed filtered density function (FDF), has been adopted both with and without accounting for differential diffusion effects.
The primary benefit of flamelet models lies in their significantly lower computational cost compared to approaches that transport all species individually. Here, the thermochemical states of the reacting mixture are captured through a library of one-dimensional laminar flamelets, computed a priori, and parameterized by a reduced set of controlling variables. These 1-D flames are then convoluted with a β-FDF to incorporate turbulence effects, and the results are stored in a lookup table. The model application differs slightly when applied to non-premixed or premixed and partially premixed combustion.

3.1.1 Non-premixed combustion

In non-premixed combustion, the thermochemical states depend solely on the mixture fraction. As noted in the previous chapter, the scalar dissipation rate plays a crucial role in quantifying the mixing rate between fuel and oxidizer. This study employs the steady diffusion flamelet model (SDM) to evaluate the model's performance in a diffusion flame. Counterflow 1-D laminar diffusion flames are used to generate the flamelet manifold, with the scalar dissipation rate varied by changing the inlet velocities in the counterflow setup (see Fig. 2.1).

The scalar dissipation rate χ serves as the key non-equilibrium parameter [191]. χ is a function of the mixture fraction, but can, as shown by Peters [122], be parametrized by its value at stoichiometric mixture χ_{st}. Therefore, χ_{st} acts as an external parameter that imposes strain on the flamelet and defines its structure. Starting with a low mass flow, several flamelets can be calculated by incrementally increasing the mass flow and also the imposed strain until the extinction limit is reached. Once the solution of the flamelet equations is known for a sufficient number of χ_{st}, the temperature as well as the species mass fractions can be tabulated as a function of mixture fraction and scalar dissipation rate at stoichiometry [192]. Results from the 1-D flames are pre-integrated using the joint FDF of mixture fraction and scalar dissipation rate. A β-FDF is used to model the mixture fraction distribution, while a Dirac function $P(\chi_{st}) = \delta(\chi_{st} - \widetilde{\chi}_{st})$ is used for χ_{st}, to neglect its fluctuations. Statistical independence allows the joint FDF to be written as: $P(z, \chi_{st}; \widetilde{z}, \widetilde{\sigma}_z, \overline{\chi}_{st}) = P(z; \widetilde{z}, \widetilde{\sigma}_z) P(\chi_{st}; \widetilde{\chi}_{st})$. Filtered thermochemical quantities $\widetilde{\zeta}(\widetilde{z}, \overline{\chi}_{st})$ are then obtained via:

$$\widetilde{\zeta}(\widetilde{z}, \overline{\chi}_{st}) = \int_0^1 \zeta(z, \chi_{st}) P(z, \chi_{st}; \widetilde{z}, \widetilde{\sigma}_z, \widetilde{\chi}_{st})\, dz\, d\chi_{st} \tag{3.1}$$

The mixture fraction variance $\widetilde{\sigma}_z$, required for table lookup, is computed algebraically: $\widetilde{\sigma}_z = C_{var} L_s^2 |\partial \widetilde{z} / \partial x_i|^2$ [193], where $C_{var} = 0.5$ and the subgrid length $L_s = \min(0.41d, C_s \Delta)$ incorporates wall distance d, Smagorinsky constant C_s, and local grid size Δ [191]. The mean scalar dissipation rate follows an algebraic expression in LES:

$$\widetilde{\chi}_{st} = C_\chi \frac{\mu_t + \mu}{\overline{\rho} S c_t} \left| \frac{\partial \widetilde{z}}{\partial x_i} \right|^2 \tag{3.2}$$

with $C_\chi = 2$ a model constant [194].

3.1.2 Partially premixed combustion

For partially premixed combustion, the lookup table is created by tabulating the thermochemical quantities as functions of the progress variable c, mixture fraction z, and their variances σ_c and σ_z. The progress variable is defined based on water vapor mass fraction $c = Y_{\mathrm{H_2O}} / \psi_{max}(z)$, while z follows the Bilger's mixture fraction formulation [148]. For hydrogen the Bilger's mixture fraction can be written as:

$$z = \frac{\frac{1}{2W_H}(z_H - z_{H,o}) - \frac{1}{W_O}(z_O - z_{O,o})}{\frac{1}{2W_H}(z_{H,f} - z_{H,o}) - \frac{1}{W_O}(z_{O,f} - z_{O,o})}, \tag{3.3}$$

where z_k is the elemental mass fraction of species k and the subscripts f and o indicate the fuel and oxidizer streams respectively. This approach relies on two key assumptions: all relevant thermochemical states can be represented by a limited number of controlling variables, and these variables are statistically independent.

Consequently, the joint FDF $P(c,z;\widetilde{c},\widetilde{z},\widetilde{\sigma_c},\widetilde{\sigma_z})$, modeled as a β-FDF [126, 183], can be written as the product of marginal FDFs $P(c;\widetilde{c},\widetilde{\sigma_c})$ and $P(z;\widetilde{z},\widetilde{\sigma_z})$ [110, 195, 196], simplifying the lookup table construction. In the baseline formulation, the Favre-filtered transport equations for c and z take the form:

$$\frac{\partial\overline{\rho}\widetilde{c}}{\partial t}+\frac{\partial\overline{\rho}\widetilde{u}_i\widetilde{c}}{\partial x_i}=\frac{\partial}{\partial x_i}\left[\left(\overline{\rho D_c}+\frac{\mu_t}{Sc_t}\right)\frac{\partial\widetilde{c}}{\partial x_i}\right]+\overline{\dot{\omega}}_c \tag{3.4}$$

$$\frac{\partial\overline{\rho}\widetilde{z}}{\partial t}+\frac{\partial\overline{\rho}\widetilde{u}_i\widetilde{z}}{\partial x_i}=\frac{\partial}{\partial x_i}\left[\left(\overline{\rho D_z}+\frac{\mu_t}{Sc_t}\right)\frac{\partial\widetilde{z}}{\partial x_i}\right] \tag{3.5}$$

where $\overline{\rho D_c}=\overline{\rho D_z}=\widetilde{\mu}/Sc$, with the laminar Schmidt number Sc taken equal to the turbulent value $Sc_t=0.7$. The filtered chemical source term $\overline{\dot{\omega}}_c$ in Eq. (3.4) is retrieved from the lookup table as [110, 197, 198]:

$$\overline{\dot{\omega}}_c(\widetilde{c},\widetilde{z},\widetilde{\sigma_c},\widetilde{\sigma_z})=\overline{\rho}\int_0^1\int_0^1\frac{\dot{\omega}_c(c,z)}{\rho(c,z)}P(c,z;\widetilde{c},\widetilde{z},\widetilde{\sigma_c},\widetilde{\sigma_z})\,dc\,dz+\overline{\dot{\omega}}_{np} \tag{3.6}$$

with $\dot{\omega}_c(c,z)$ taken from the 1-D laminar flamelet solutions. The progress variable is normalized to $\widetilde{c}\in[0,1]$, while z spans the flammability limits, i.e. $\widetilde{z}\in[z_{\text{lean}},z_{\text{rich}}]$. Variances follow bounded ranges using a bimodal prescription: $\widetilde{\sigma_c}\in[0,\widetilde{c}(1-\widetilde{c})]$ and $\widetilde{\sigma_z}\in[0,\widetilde{z}(1-\widetilde{z})]$. Due to the use of a normalized progress variable, a correction term $\overline{\dot{\omega}}_{np}$ accounts for non-premixed combustion contributions and is calculated as [86, 199]:

$$\overline{\dot{\omega}}_{np}(\widetilde{z},\sigma_z)=\overline{\rho}\widetilde{c}\widetilde{\chi}_z\int_0^1\frac{1}{\psi_{\max}(z)}\frac{d^2\psi_{\max}(z)}{dz^2}P(z;\widetilde{z},\sigma_z)\,dz \tag{3.7}$$

where $\psi_{\max}(z)$ normalizes the progress variable. The scalar dissipation rate of mixture fraction $\widetilde{\chi}_z=\widetilde{D}\nabla\widetilde{z}\cdot\nabla\widetilde{z}+\widetilde{\varepsilon}_z$ combines resolved and modeled subgrid contributions, with $\widetilde{\varepsilon}_z=c_z(\nu_t/\Delta^2)\sigma_z$ ($c_z=2$ [121]), $\Delta=V^{1/3}$, and V the local cell volume. To access the four-dimensional lookup table for $\overline{\dot{\omega}}_c$, transport equations for the variances $\widetilde{\sigma}_c$ and $\widetilde{\sigma}_z$ are solved:

$$\frac{D\overline{\rho}\widetilde{\sigma_c}}{Dt}=\frac{\partial}{\partial x_i}\left[\left(\overline{\rho D_c}+\frac{\mu_t}{Sc_t}\right)\frac{\partial\widetilde{\sigma_c}}{\partial x_i}\right]-2\overline{\rho}\widetilde{\varepsilon_c}+2\frac{\mu_t}{Sc_t}\left(\frac{\partial\widetilde{c}}{\partial x_i}\frac{\partial\widetilde{c}}{\partial x_i}\right)+2(\overline{c\dot{\omega}_c}-\widetilde{c}\overline{\dot{\omega}}_c) \tag{3.8}$$

$$\frac{D\overline{\rho}\widetilde{\sigma_z}}{Dt}=\frac{\partial}{\partial x_i}\left[\left(\overline{\rho D_z}+\frac{\mu_t}{Sc_t}\right)\frac{\partial\widetilde{\sigma_z}}{\partial x_i}\right]-2\overline{\rho}\widetilde{\varepsilon_z}+2\frac{\mu_t}{Sc_t}\left(\frac{\partial\widetilde{z}}{\partial x_i}\frac{\partial\widetilde{z}}{\partial x_i}\right) \tag{3.9}$$

In both variance equations, the first term in the RHS accounts for molecular and subgrid turbulent diffusion, the second term models the dissipation of subgrid variance, and the third captures variance production from the interaction between subgrid fluctuations and resolved gradients. The final term in Eq. (3.8) provides a chemical source (or sink) for subgrid variance, where the term $\overline{c\dot{\omega}_c}$ is computed a priori and tabulated together with the other thermochemical variables. Unlike the mixture fraction, the subgrid scalar dissipation rate of the progress variable $\widetilde{\varepsilon}_c$ requires a

specialized model. Here, it is computed as [196, 200]:

$$\widetilde{\varepsilon}_c = \left[1 - \exp\left(\frac{-0.75\Delta}{\delta_{th}}\right)\right]\left[(2K_c - \tau C_4)\frac{s_L}{\delta_{th}} + C_3'\frac{\epsilon_k}{k}\right]\frac{\widetilde{\sigma}_c}{\beta_c} \tag{3.10}$$

where s_L, δ_{th}, and τ denote the laminar flame speed, thermal flame thickness, and heat release factor, respectively, all extracted from the flamelet library. The remaining coefficients are non-dimensional constants; further details appear in [86, 196]. The modeling parameter β_c, which reflects influences of flame curvature, diffusion, and reaction rates, exhibits scale dependence. In this work, β_c is determined dynamically following the approach of [200, 201]. The energy equation is solved in terms of sensible enthalpy:

$$\frac{\partial \overline{\rho}\widetilde{h}}{\partial t} + \frac{\partial \overline{\rho}\widetilde{u}_i\widetilde{h}}{\partial x_i} = \frac{\partial}{\partial x_i}\left[\left(\overline{\rho D_h} + \frac{\mu_t}{Pr_t}\right)\frac{\partial \widetilde{h}}{\partial x_i}\right] \tag{3.11}$$

Although heat losses are neglected, enthalpy is transported to improve predictions of multi-stream mixing. Filtered temperature follows from the mean-value theorem: $\widetilde{T} = T_0 + (\widetilde{h} - \Delta\widetilde{h}_0)/\widetilde{C_p^{\text{eff}}}$, with reference temperature $T_0 = 273.15\,\text{K}$, formation enthalpy $\widetilde{h}_0$, and effective specific heat $\widetilde{C_p^{\text{eff}}}$. Mixture density closes the system via the ideal gas law: $\overline{\rho} = p_0\widetilde{W}/(R_0\widetilde{T})$, where $\widetilde{W}$ is the filtered mean molecular weight and p_0 the operating pressure.
Figure 3.1 illustrates the flamelet model workflow.

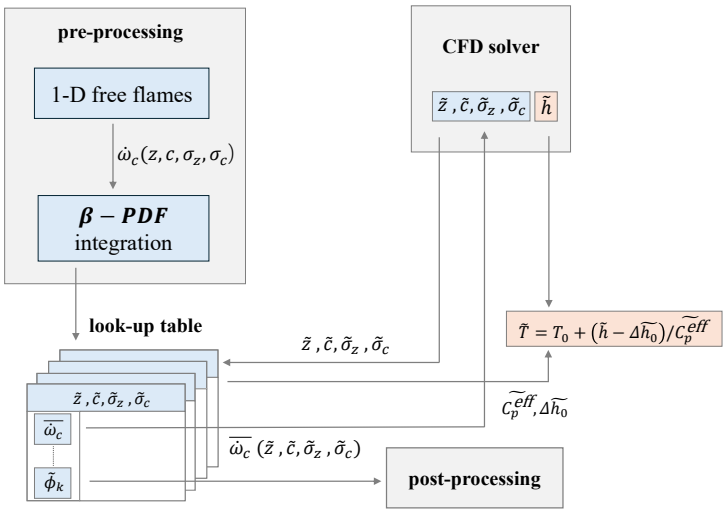

Figure 3.1: Schematic block diagram of a flamelet-based model using four controlling variables.

In hydrogen-air flames, the unity Lewis number assumption breaks down, necessitating modifications to the baseline flamelet model. The following section details the adopted extensions.

Differential diffusion modeling

In LES, differential diffusion requires correcting the diffusive transport of controlling variables, since local equivalence ratio changes couple with flame curvature at resolved scales. The model used here was first proposed in [202] and later adapted for LES [203]. This approach expresses controlling variables as linear combinations of species mass fractions:

$$c = \sum_{k=1}^{N_s} \mathcal{C}_k Y_k \tag{3.12}$$

$$z = \sum_{k=1}^{N_s} \mathcal{Z}_k Y_k \tag{3.13}$$

where N_s denotes the total number of species and $\mathcal{C}_k$, $\mathcal{Z}_k$ represent constant coefficients specific to each species. The diffusive flux of a generic controlling variable ζ can then be expressed as:

$$j_\zeta = -\sum_{k=1}^{N_s-1} \frac{\mathcal{A}_k - \mathcal{A}_{N_s}}{Le_k} \frac{\lambda}{C_p} \frac{\partial Y_k}{\partial x_i} \tag{3.14}$$

where $\mathcal{A}_{N_s}$ corresponds to the coefficient of the most abundant species (N_2 in the present study). The preceding relation provides the diffusive flux of the controlling variable ζ, defined as any linear combination of species mass fractions, under the assumption of constant Lewis numbers across species. This formulation requires storing mass fraction gradients for all species in the lookup table. To circumvent this, the approach in [202] assumes a Lewis number specific for each species but constant in space, shifting the summation over species k inside the gradient operator. The resulting expression for the controlling variable diffusive flux becomes considerably simpler to evaluate:

$$j_\zeta = -\frac{\lambda}{C_p} \frac{\partial}{\partial x_i} \underbrace{\left(\sum_{k=1}^{N_s-1} \frac{\mathcal{A}_k - \mathcal{A}_{N_s}}{Le_k} Y_k \right)}_{\beta_\zeta} \tag{3.15}$$

With this formulation of the diffusive flux, only the gradient of one additional tabulated quantity β_ζ needs to be computed. In the present study, the progress variable depends solely on water vapor, so the coefficient $\mathcal{C}_{H_2O} = 1/\psi_{\max}(z)$, while all other $\mathcal{C}_k = 0$. The quantity β_c for the progress variable adopts the general form:

$$\beta_c = \frac{Y_{H_2O} - Y_{H_2O}^{\text{reac}}}{Le_{H_2O}\, \psi_{max}(z)} \tag{3.16}$$

A similar procedure can be followed for the enthalpy equation, where the heat flux can be written as:

$$\dot{q} = \underbrace{-\lambda \frac{\partial T}{\partial x_i}}_{\text{heat conduction}} - \underbrace{\left(\sum_{k=1}^{N_s-1} \frac{\lambda}{C_p} \frac{h_k - h_{N_s}}{Le_k} \frac{\partial Y_k}{\partial x_i} \right)}_{\text{species diffusion}} \tag{3.17}$$

where the first term represents the heat conduction flux while the second term is the redistribution of enthalpy associated to the different diffusion of species. The heat flux can be then rewritten as:

$$\dot{q} = -\frac{\lambda}{C_p} \underbrace{\left(C_p - \sum_{k=1}^{N_s-1} \frac{c_{p_k} - c_{p_{N_s}}}{Le_k} Y_k \right)}_{\beta_{h_1}} \frac{\partial T}{\partial x_i} - \frac{\lambda}{C_p} \frac{\partial}{\partial x_i} \underbrace{\left(\sum_{k=1}^{N_s-1} \frac{h_k - h_{N_s}}{Le_k} Y_k \right)}_{\beta_{h_2}} \tag{3.18}$$

where c_{p_k} denotes the specific heat capacity at constant pressure of species k. The two terms in the RHS of the above equation capture differential diffusion contributions to the heat flux: the first arises from local redistribution of specific heat and enthalpy, while the second stems from species diffusion within the mixture. The complete set of modified LES transport equations for the controlling variables and enthalpy then reads:

$$\frac{D\overline{\rho}\widetilde{c}}{Dt} = \frac{\partial}{\partial x_i} \left(\frac{\mu_t}{Sc_t} \frac{\partial \widetilde{c}}{\partial x_i} \right) + \frac{\partial}{\partial x_i} \left(\overline{\rho} \widetilde{D} \frac{\partial \widetilde{\beta}_c}{\partial x_i} \right) + \overline{\dot{\omega}}_c \tag{3.19}$$

$$\frac{D\overline{\rho}\widetilde{z}}{Dt} = \frac{\partial}{\partial x_i} \left(\frac{\mu_t}{Sc_t} \frac{\partial \widetilde{z}}{\partial x_i} \right) + \frac{\partial}{\partial x_i} \left(\overline{\rho} \widetilde{D} \frac{\partial \widetilde{\beta}_z}{\partial x_i} \right) \tag{3.20}$$

$$\frac{D\overline{\rho}\widetilde{\sigma}_c}{Dt} = \frac{\partial}{\partial x_i} \left[\left(\overline{\rho D_c} + \frac{\mu_t}{Sc_t} \right) \frac{\partial \widetilde{\sigma}_c}{\partial x_i} \right] - 2\overline{\rho}\widetilde{\varepsilon}_c + 2\frac{\mu_t}{Sc_t} \left(\frac{\partial \widetilde{c}}{\partial x_i} \frac{\partial \widetilde{c}}{\partial x_i} \right) + 2(\overline{c\dot{\omega}_c} - \widetilde{c}\overline{\dot{\omega}}_c) \tag{3.21}$$

$$\frac{D\overline{\rho}\widetilde{\sigma}_z}{Dt} = \frac{\partial}{\partial x_i} \left[\left(\overline{\rho D_z} + \frac{\mu_t}{Sc_t} \right) \frac{\partial \widetilde{\sigma}_z}{\partial x_i} \right] - 2\overline{\rho}\widetilde{\varepsilon}_z + 2\frac{\mu_t}{Sc_t} \left(\frac{\partial \widetilde{z}}{\partial x_i} \frac{\partial \widetilde{z}}{\partial x_i} \right) \tag{3.22}$$

$$\frac{D\overline{\rho}\widetilde{h}}{Dt} = \frac{\partial}{\partial x_i} \left(\frac{\mu_t}{Pr_t} \frac{\partial \widetilde{h}}{\partial x_i} \right) + \frac{\partial}{\partial x_i} \left(\overline{\rho} \widetilde{D} \widetilde{\beta_{h_1}} \frac{\partial \widetilde{T}}{\partial x_i} + \overline{\rho} \widetilde{D} \frac{\partial \widetilde{\beta_{h_2}}}{\partial x_i} \right) \tag{3.23}$$

The filtered coefficients $\widetilde{\beta}_\zeta$ and the filtered diffusivity $\widetilde{D}$ appearing in the above equations are retrieved from precomputed flamelet solutions, after tabulation through pre-integration.

3.2 Transported FDF approach

In reacting flows, multiple scalars are involved, making the joint PDF $\mathcal{F}(\psi;x,t)$ of the complete scalar set $\psi=[\psi_1,...,\psi_{N_s}]$ relevant. This joint FDF is defined as the product of the marginal FDFs $P_\zeta=\delta(\psi_\zeta-\phi_\zeta)$ for each scalar ζ, where δ represents the Dirac delta function:

$$\mathcal{F}(\psi;x,t)=\prod_{\zeta=1}^{N_s}\delta[\psi_\zeta-\phi_\zeta(x,t)] \tag{3.24}$$

where ψ_ζ denotes the composition space of the scalar ϕ_ζ. The joint FDF, denoted $\widetilde{P}_{sgs}$, accounts for the effects of subgrid-scale fluctuations on species formation rates. It is defined as the filtered product of the fine-grained FDFs for each scalar (i.e. the molar concentrations of chemical species and enthalpy):

$$\widetilde{P}_{sgs}=\frac{1}{\overline{\rho}}\int_V \rho G(x-x',\Delta(x))\mathcal{F}(\psi;x',t)\,dx' \tag{3.25}$$

The above equation represents the probability of observing values of a scalar ζ in the interval $\psi_\zeta<\phi_\zeta<\psi_\zeta+d\psi_\zeta$ within the filter volume, which is $\widetilde{P}_{sgs}(\psi;x,t)d\psi$. An exact equation for the evolution of $\widetilde{P}_{sgs}$ can be derived following [204–206]:

$$\begin{aligned}\frac{\partial\overline{\rho}\widetilde{P}_{sgs}(\psi)}{\partial t}+\frac{\partial\overline{\rho}\widetilde{u}_j\widetilde{P}_{sgs}(\psi)}{\partial x_i}-\underbrace{\sum_{\zeta=1}^{N_\zeta}\frac{\partial}{\partial\psi_\zeta}\left[\overline{\rho}\dot{\omega}_\zeta(\psi)\widetilde{P}_{sgs}(\psi)\right]}_{\textbf{chemical reaction}\ \text{(closed)}}=\\ \underbrace{\frac{\partial}{\partial x_i}\left[\overline{\rho}\left(\frac{\overline{\nu}}{Sc}+\frac{\nu_t}{Sc_t}\right)\frac{\partial\widetilde{P}_{sgs}(\psi)}{\partial x_i}\right]}_{\textbf{sgs convection}\ \text{(gradient closure)}}\\ \underbrace{-\sum_{\zeta=1}^{N_\zeta}\sum_{\beta=1}^{N_\beta}\frac{\partial^2}{\partial\psi_\zeta\partial\psi_\beta}\left(\overline{\rho}\overline{D}\overline{\frac{\partial\phi_\zeta}{\partial x_i}\frac{\partial\phi_\beta}{\partial x_i}}\Big|_{\boldsymbol{\phi}=\boldsymbol{\psi}}\widetilde{P}_{sgs}(\psi)\right)}_{\mathcal{M}(\psi;x,t);\ \textbf{sgs micro-mixing}\ \text{(LMSE closure)}}\end{aligned} \tag{3.26}$$

The advantage of using this equation is that now the chemical source term $\dot{\omega}_\zeta$ appears in a closed form and does not require any further modeling. However, the last term of the RHS, which represents the molecular mixing (or micro-mixing) requires further modeling. A common practice is to use the Linear Mean Square Estimation (LMSE) closure [207–209]:

$$\mathcal{M}(\psi;x,t)=\frac{\overline{\rho}}{2\tau_{sgs}}\sum_{\zeta=1}^{N_s}\frac{\partial}{\partial\psi_\zeta}\left[(\psi_\zeta-\widetilde{\phi}_\zeta(x,t))\widetilde{P}_{sgs}(\psi)\right] \tag{3.27}$$

where the subgrid mxing time scale τ_{sgs} is calculated as [**210**]

$$\frac{1}{\tau_{sgs}} = C_D \frac{\mu + \mu_t}{\overline{\rho}\Delta^2} \tag{3.28}$$

where C_D is the micro-mixing constant of 2 in LES [**187**, **211**, **212**]. Eq. (3.26) can be solved using a Lagrangian particle method or a Reynolds-averaged Eulerian formulation. The latter approach is adopted in the present work.

3.2.1 Eulerian stochastic fields approach

The transport equation for $\widetilde{P}_{sgs}$ (Eq. (3.26)) derived in the previous section involves too many independent variables for practical numerical solution. Instead, a stochastic approach is employed, representing $\widetilde{P}_{sgs}(\psi)$ through an ensemble of stochastic Eulerian fields $\xi^n_\zeta(x,t)$ for each scalar ζ. Eq. (3.25) can then be rewritten as:

$$\widetilde{P}_{sgs}(\psi;x,t) = \frac{1}{N}\sum_{n=1}^{N}\frac{1}{\overline{\rho}}\int_V \rho\, G(x-x'),\Delta(x)) \times \prod_{\zeta=1}^{N_s}\delta\left[\psi_\zeta - \xi^n_\zeta(x,t)\right] dx' \tag{3.29}$$

where N is the number of stochastic fields and $n \in [1,N]$ and $\zeta \in [1,N_s]$. A set of stochastic differential equations equivalent to Eq. (3.26) can be derived following [**186**]:

$$\begin{aligned} d\overline{\rho}\,\xi^n_\alpha + \frac{\partial(\overline{\rho}\widetilde{u}_i\xi^n_\alpha)}{\partial x_j}dt = {} & \underbrace{\overline{\rho}\,\dot{\omega}^n_\alpha(\underline{\xi}^n)dt}_{\textbf{chemical source term}} + \underbrace{\frac{\partial}{\partial x_j}\left[\overline{\rho}\left(\frac{\overline{\nu}}{Sc}+\frac{\nu_t}{Sc_t}\right)\frac{\partial \xi^n_\alpha}{\partial x_j}\right]dt}_{\textbf{sgs convection term}} \\ & + \overline{\rho}\underbrace{\sqrt{2\frac{\mu_t}{\overline{\rho}Sc_t}}\frac{\partial \xi^n_\alpha}{\partial x_j}dW^n_j(t)}_{\textbf{stochastic term}} \\ & - \underbrace{\frac{\overline{\rho}}{2\tau_{sgs}}(\xi^n_\alpha - \widetilde{\phi}_\alpha)dt}_{\textbf{micro-mixing term (LMSE)}} \end{aligned} \tag{3.30}$$

The third term on the RHS represents a stochastic term that varies for each field but remains independent of spatial location x. Consequently, it has no influence on the filtered values $\widetilde{\xi^n_\zeta}$ when a sufficiently large number of fields is employed:

$$\lim_{N\to\infty}\sum_{n=1}^{N}\sqrt{2\frac{\mu_t}{\overline{\rho}Sc_t}}\frac{\partial \xi^n_\alpha}{\partial x_j}dW^n_j(t) = 0 \tag{3.31}$$

The laminar diffusivity was originally included in the stochastic term of Eq. (3.30) by [**186**]. Hereby the latest formulation is used [**127**], which only includes the sub-grid contribution. This prevents unphysical fluctuations of the scalar gradients due to

the stochastic term in purely laminar regions of the flow field. The solutions of the stochastic fields equation are continuous, differentiable and smooth on the scale of the filter width in space, and continuous but not differentiable in time. These solutions are not to be mistaken with any particular realization of the real field, but rather form an equivalent stochastic system in the sense that all the one-point moments resulting from the stochastic differential equations system and from the solutions of Eq. (3.30) will be identical, so that mean $\widetilde{\phi}_\zeta$ and sgs-variance $\widetilde{\sigma}^{sgs}_{\phi_\zeta}$ of the scalar ϕ_ζ can be obtained as:

$$\widetilde{\phi}_\zeta = \frac{1}{N}\sum_{n=1}^{N}\int_{\psi_\zeta=-\infty}^{\psi_\zeta=+\infty} \psi_\zeta \delta(\psi_\zeta - \xi_\zeta^n)\, d\psi_\zeta = \frac{1}{N}\sum_{n=1}^{N}\xi_\zeta^n \tag{3.32}$$

$$\widetilde{\sigma}^{sgs}_{\phi_\zeta} = \sqrt{\frac{1}{N}\sum_{n=1}^{N}\int_{\psi_\zeta=-\infty}^{\psi_\zeta=+\infty} \psi_\zeta^2 \delta(\psi_\zeta - \xi_\zeta^n)\, d\psi_\zeta - \widetilde{\phi}_\zeta^2} = \sqrt{\frac{1}{N}\sum_{n=1}^{N}\xi_\zeta^n - \widetilde{\phi}_\zeta^2} \tag{3.33}$$

A great advantage of this method is that, due to the Eulerian properties of the stochastic fields, conventional LES solver can be used, and thus, stochastic fields can be easily incorporated into any existing code. However, care has to be taken regarding the choice of the discretization scheme. Further details on this topic can be found in [212]. In this model differential diffusion effects are taken into account by setting a diffusion coefficient D_k different for each species, which depends on the Lewis number of each species k assumed to be constant:

$$D_k = \frac{\lambda}{\rho C_p Le_k} \tag{3.34}$$

4 Test Cases

In this chapter, the test cases considered in this work are presented. Two cases are analyzed, referred to as the *NTNU* case and the *HYLON* case. The HYLON case is examined only in the initial phase of the study and is therefore discussed with less detail, while the NTNU case represents the core of the investigation. Two CFD solvers are employed: *Ansys Fluent 2023 R1*, used to assess the baseline flamelet-based models described in Sec. 3.1.1 and 3.1.2 of Chapter 3 for different regimes of hydrogen-air flames, and the open-source code *OpenFOAM*, which is adopted for most of the simulations carried out in this work.

4.1 NTNU case

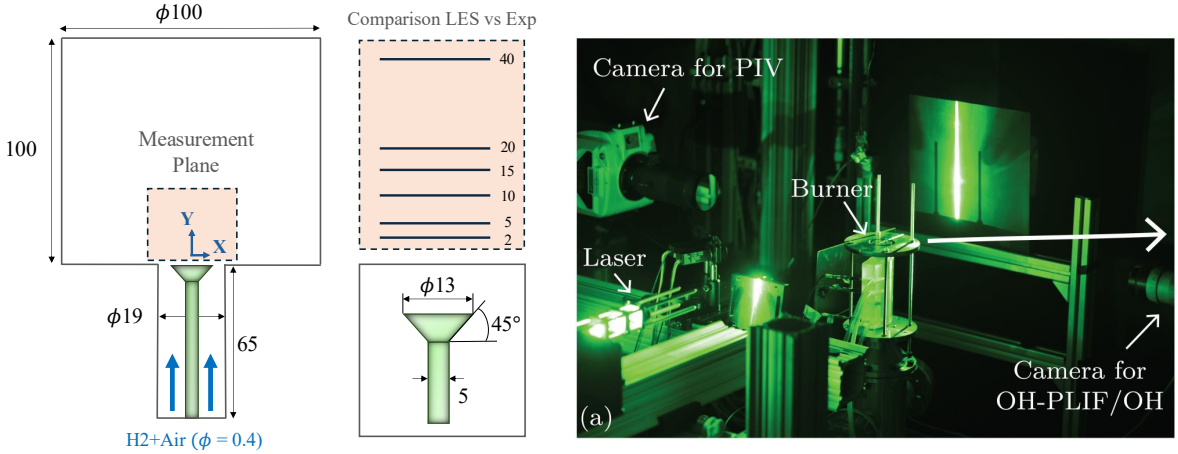

Figure 4.1: Schematic of the NTNU premixed hydrogen burner: vertical cross section passing through the bluff-body axis (left) and picture of the experimental setup (right) from [91]. All dimensions are reported in mm.

The premixed flame configuration studied at the Norwegian University of Science and Technology (NTNU) consists in a bluff-body stabilized burner. A schematic of the geometry is shown in Fig. 4.1. The conical bluff body has a diameter $d_b = 13$ mm and half-cone angle $\alpha = 45°$. The hydrogen-air mixture is injected through an annular duct surrounding the bluff-body holder. The external diameter of the inlet duct is $d_i = 19$ mm, whereas the bluff-body holder has a diameter of 5 mm. The burner downstream of the bluff body operates with no confinement. Therefore, the flame develops in a free environment at ambient pressure and temperature.
The bluff body's holder is centered by a set of three transversal cylinders (of diameter 2 mm each) that are placed at a distance of 65 mm upstream of the bluff-body top surface. The location of these cylinders is sufficiently far upstream not to affect the flame dynamics [**213–215**]. Regarding the operating conditions, the hydrogen-air mixture is injected at room temperature, $T_{amb} = 25°$C. The mass flow rates of hydrogen and air are equal to $\dot{m}_{H_2} = 2.92 \times 10^{-5}$ kg/s and $\dot{m}_{air} = 2.258 \times 10^{-3}$ kg/s, respectively. The equivalence ratio is kept constant at $\phi = 0.4$. Given that $LHV = 120$ MJ/kg, the hydrogen flow rate supplied to the rig results in a thermal power of the burner equal to $P_{\text{th}} = 3.5$ kW. The operating conditions have been summarized in Tab. 4.1.

ϕ	T^u [K]	$\dot{m}_{H_2}$ [kg/s]	$\dot{m}_{air}$ [kg/s]	P_{th} [kW]
0.4	298.15	2.92×10^{-5}	2.258×10^{-3}	3.5

Table 4.1: NTNU operating conditions. From left to right: equivalence ratio, inlet mixture temperature, hydrogen mass flow rate, air mass flow rate and theoretical burner power.

4.2 HYLON case

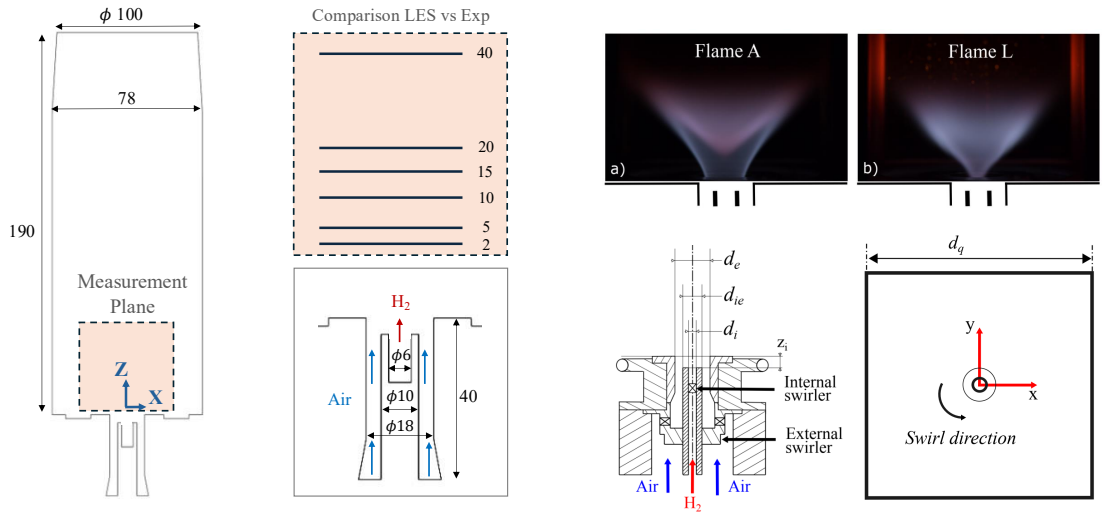

Figure 4.2: Schematic of the HYLON non-premixed hydrogen burner: vertical cross section passing through the swirler axis (left) and images of the flame obtained in the experiments (right) from [90]. Hydrogen and air are injected through two separate ducts (blue for air and red for hydrogen). Both streams are swirled and before the combustion chamber there is a zone to enhance the mixing between the two streams.

The non-premixed flame studied in this work is the HYLON burner (HYdrogen LOw NOx) dual swirl injector investigated at the Insitut de Mécanique des Fluides de Toulouse (IMFT). A schematic of the configuration is shown in Fig. 4.2.
The burner is characterized by two swirling coaxial ducts for the separate injection of hydrogen and air with dimension $d_{air} = 18$ mm and $d_{H_2} = 4$ mm, respectively. The combustion chamber has the following dimensions: side $h_c = 78$ mm, length $L_c = 150$ mm and outflow diameter $d_o = 73$ mm. A gap of $z_i = 4$ mm between the exit of the hydrogen nozzle and the entry of the combustion chamber enhances the mixing between the two streams. Two different operating conditions are investigated in this work: Flame A, which is attached to the hydrogen nozzle, and Flame L which is lifted above the fuel injector. The flow and fuel quantities for these operating conditions are reported in Table 4.2.

Flame	$\dot{m}_{air}$ [kg/s]	$\dot{m}_{H_2}$ [kg/s]	T_{air} [K]	T_{H_2} [K]	P_{th} [kW]	p [Pa]
A	2.41×10^{-3}	3.2×10^{-5}	298	298	3.89	101325
L	6.03×10^{-3}	8.0×10^{-5}	298	298	9.73	101325

Table 4.2: HYLON operating conditions for the two flames investigated in this work.

5 Investigation of Premixed and Non-Premixed Hydrogen Flames Using LES with Flamelet Models

In this chapter numerical investigations of premixed and non-premixed hydrogen flames are performed with the main aim of assessing the capability of large-eddy simulations and flamelet models to predict the main characteristics of the reactive field. Both the two test cases presented in Chapter 4 are investigated here. Simulations of the premixed burner are performed using the Flamelet Generated Manifold approach, whereas the two types of flames realized in the non-premixed burner are studied using the Steady Diffusion Flamelet and the Flamelet Generated Manifold. Numerical results are compared with the available experimental data for flow and flame characterization.

5.1 Introduction

The International Workshop on Measurement and Computation of Turbulent Flames (TNF) [216] has recently released three test cases featuring pure hydrogen premixed and non-premixed flames, providing detailed measurements to enhance understanding of combustion processes in practically relevant configurations and to serve as validation for combustion models. Numerical simulations play a pivotal role in combustor design, such as downselecting burner geometries or performing optimization studies. In highly unsteady and anisotropic flows, exemplified by vortex breakdown in swirling configurations, large-eddy simulations (LES) enable accurate resolution of the mixing field by explicitly capturing energy-containing scales. Reacting flows introduce chemical timescales that interact with turbulence, particularly in low-Damköhler number (Da) flames where time-resolved flame structure descriptions with detailed chemistry are essential for reliable predictions [112]. Conversely,

if the chemical time scales are small compared to the time scales associated to turbulence ($Da \gg 1$), a flamelet description of the flame structure has been proven to provide accurate predictions. Moreover, if the flame works in a flamelet regime, complex detailed combustion mechanisms can be used to build a flamelet library without increasing the computational cost. Although numerical methods have been extensively assessed and validated for hydrocarbon fuels, when it comes to hydrogen, which is characterized by a significantly different behavior compared to hydrocarbon fuels, such detailed validation of the numerical tools has not been performed yet. Aniello et al. [217] applied the Dynamic Thickened Flame model (DTFLES) to the non-premixed IMFT flame, demonstrating predictive capability across investigated regimes. Ballotti et al. [218] extended this approach with a dynamic thickening strategy for high-fidelity CFD in multi-regime combustion on the same rig. For the premixed NTNU flame, Kutkan et al. [219, 220] employed flamelet models with CH4/H2-air blends, although under different operating conditions and minor geometric variations. Thickened flame approaches have also been used to investigate ignition dynamics on the NTNU burner [97, 221, 222]. Very recently, both the test cases were investigated by Liu et al [223, 224] using a transported probability density function with the Eulerian stochastic fields (ESF) approach, including also differential diffusion effects for the premixed case. These efforts highlight model potential but underscore gaps in pure hydrogen validation across regimes. This work systematically assesses the capability of flamelet-based models in their baseline form presented in Chapter 3 for industrial hydrogen flames. The objectives of the present work are twofold: (i) evaluate flame structure and flow field predictions in premixed and non-premixed flames by comparing LES time-averaged axial and radial velocities with experimental velocity measurements, and by comparing LES time-averaged heat release rate (HRR) and OH mass fraction with experimental OH*-chemiluminescence and OH-PLIF data, respectively; (ii) validate dynamic behavior, including RMS velocity fluctuations and lift-off in lifted flames. The chapter proceeds with the description of numerical methods and setup, results and discussion, followed by conclusions.

5.2 Numerical Methods

Numerical simulations are performed using the large eddy simulation (LES) approach combined with flamelet-based models. Both flamelet models are available in the standard distribution of ANSYS Fluent R23.1, which is the code employed in this work. The reduced GRI-MECH 3.0 mechanism with 10 species and 29 reactions is used for the combustion chemistry in both cases [225]. The flamelet tables are constructed by integrating the results of one-dimensional laminar flame simulations, carried out in ANSYS Fluent, with a β-FDF. The computational domains and grids for the two configurations are created with ICEM CFD R19, and the corresponding

numerical setups are described in detail in the following sections.

5.2.1 NTNU case

The computational domain begins immediately downstream of the three cylinders positioned 65 mm upstream of the bluff-body plane. The open region above the bluff-body is represented as a cylindrical volume with diameter $d = 100$ mm and height $h = 100$ mm, as illustrated schematically in Fig. 5.1.

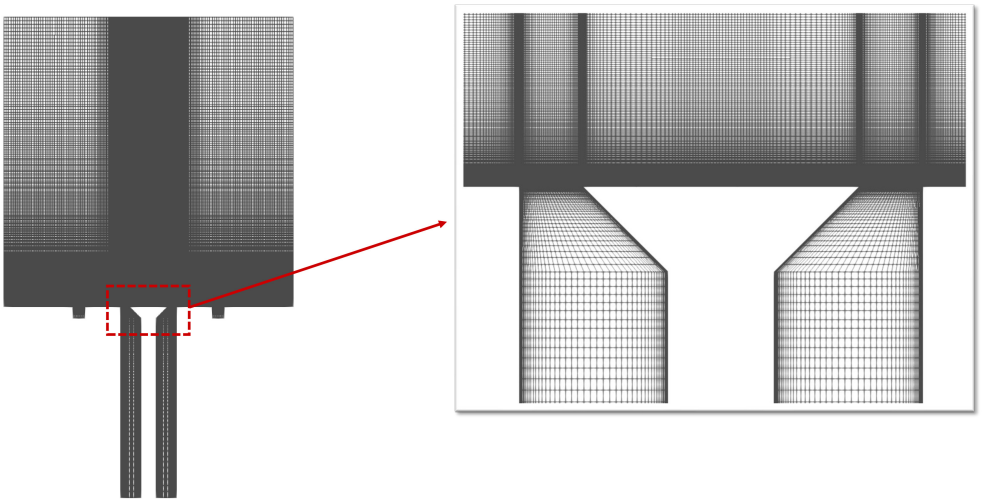

Figure 5.1: NTNU computational domain. A structured hexahedral mesh was employed, with refinement near the walls to adequately resolve the boundary layers.

The domain is discretized using a structured grid comprising 8 million hexahedral cells. The near-wall mesh ensures $y^+ < 1.0$ at all solid boundaries. Boundary conditions employed in the simulations are summarized in Table 5.1, with the corresponding boundary locations indicated in Fig. 5.2. This figure also identifies the measurement locations used for validation against experimental data: green lines denote positions analyzed for both cold and reactive flows, while blue and red lines correspond to cold-flow and reactive-flow comparisons, respectively. A bulk mass flow rate of $\dot{m} = 0.00229$ kg/s is prescribed at the mixture inlet, representing the sum of air ($\dot{m}_{\text{air}}$) and hydrogen ($\dot{m}_{\text{H}_2}$) mass flow rates reported in Table 4.1. The inlet mixture fraction $Z = 0.0125$ is determined from the experimental theoretical power. Both non-reacting (cold) and reacting flow simulations are conducted using a time step of $\Delta t = 1 \times 10^{-7}$ s to maintain a Courant number below unity. For the reactive case, the Flamelet Generated Manifold (FGM) model, described in Sec. 3.1.2, is employed,

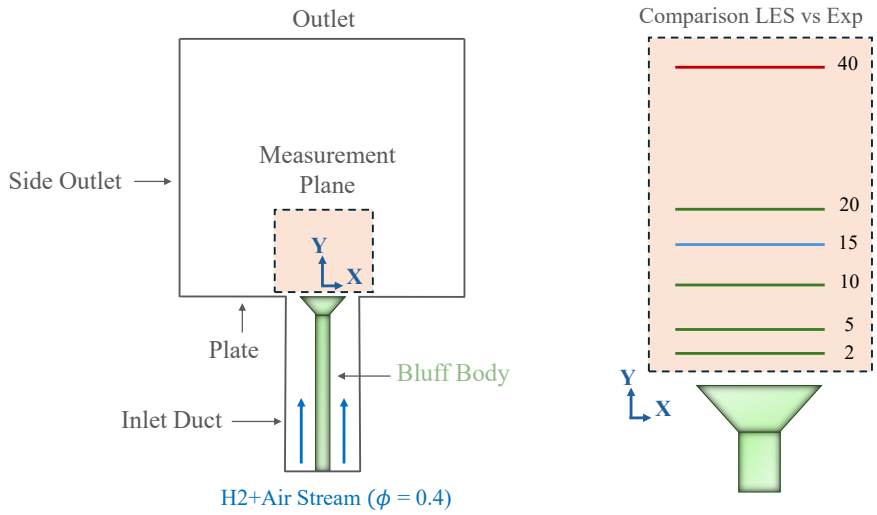

Figure 5.2: Boundary patches and locations at which comparison between experimental data and computations is performed for the NTNU test case. Green lines correspond to locations used for both cold and reactive flow simulations, while blue and red lines are locations used for the assessment of only cold or reactive flow simulations, respectively.

with the lookup table generated from one-dimensional freely propagating premixed laminar flames in Ansys Fluent.

NTNU Boundary Conditions	
H2+Air Stream	Mass Flow Inlet
Bluff Body	No-Slip Wall
Inlet Duct	No-Slip Wall
Plate	No-Slip Wall
Side Outlet	Pressure Outlet
Outlet	Pressure Outlet

Table 5.1: Boundary conditions used for the investigation of the NTNU case.

To evaluate the capability of the simulation to capture the flow topology, time-averaged and root-mean-square (RMS) profiles of axial and radial velocity components are compared against experimental measurements. The capability of the model to predict the flame structure was assessed through comparisons with experimental data on OH-PLIF and OH*-Chemiluminescence. These two quantities were compared with the time-averaged OH mass fraction and the time-averaged heat release rate (HRR), respectively. The HRR is computed following the formulation proposed by [220]:

$$\widetilde{\mathrm{HRR}} = \overline{\dot{\omega}}_c \, \mathrm{LHV}_{\mathrm{H_2}} \, \widetilde{Z}, \tag{5.1}$$

where $\overline{\dot{\omega}}_c$ denotes the filtered source term of the progress variable, $\mathrm{LHV}_{\mathrm{H_2}}$ is the lower heating value of hydrogen, and $\widetilde{Z}$ is the filtered mixture fraction.

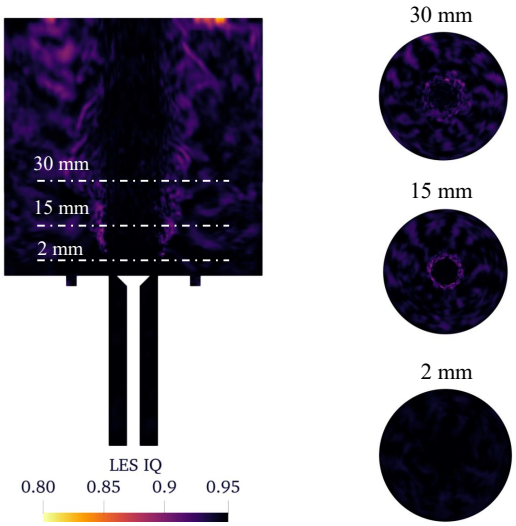

Figure 5.3: Contour plots of the Celik index assessing LES quality in the reactive flow simulation for the NTNU test case.

Mesh suitability for LES is verified by confirming that at least 80% of turbulent kinetic energy is resolved [226]. The resolved turbulent kinetic energy fraction is quantified using the Celik quality index [227]:

$$\mathrm{LES_{IQ}} = \frac{1}{1 + 0.05\left(\frac{\nu+\nu_{\mathrm{SGS}}}{\nu}\right)^{0.53}} \tag{5.2}$$

where ν is the molecular kinematic viscosity and ν_{SGS} the subgrid-scale kinematic viscosity. Contour plots of the Celik index for the NTNU reactive case appear in Fig. 5.3, shown for an x-y plane through the bluff-body centerline and three transverse planes at distinct axial locations.
Results confirm that more than 80% of the turbulent kinetic energy is resolved across the entire computational domain in the reactive simulation.

5.2.2 HYLON case

The computational domain for the HYLON test case comprises the burner geometry downstream of the hydrogen and air injection location. This domain was discretized with a structured mesh of 5 million cells, shown in Fig. 5.4. The swirler ducts are excluded from the domain. Velocity profiles at the air and fuel inlets are derived from preliminary RANS simulations of the injector alone, performed on an unstructured polyhedral mesh (see also Fig. 5.4) employing the k-ω SST turbulence model. For the RANS simulation, profiles of the x, y, and z velocity components, along with turbulent kinetic energy k and specific dissipation rate ω obtained from the swirler precursor simulations, are then mapped as inlet boundary conditions to the full burner domain. Once the RANS simulation has converged, its results are used to initialize the LES simulation. Time-averaged statistics are then collected after the RANS solu-

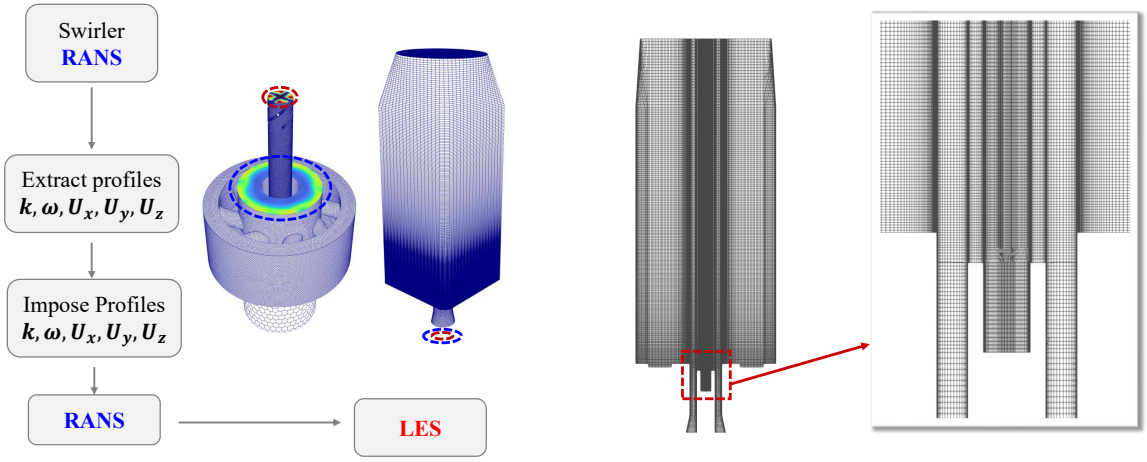

Figure 5.4: HYLON Computational Domain

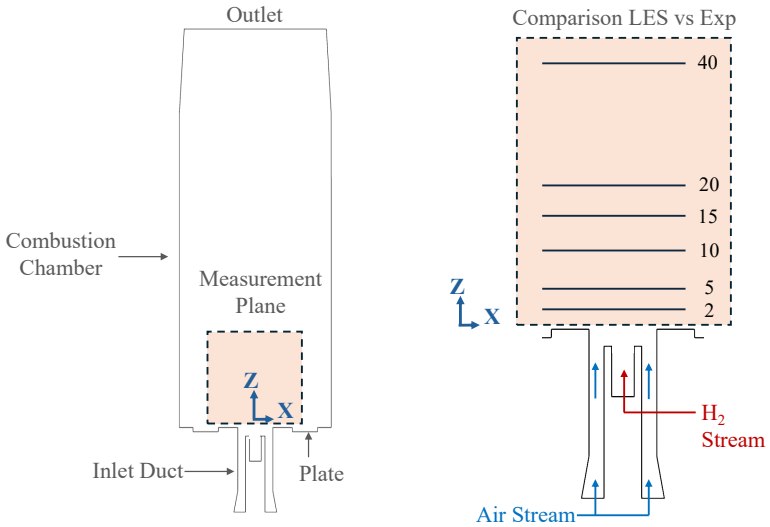

Figure 5.5: Boundary patches and locations at which comparison between experimental data and computations is performed for the HYLON test case.

tion has been completely flushed out. No turbulent inflow generator is employed for the LES simulations, following the same approach as in Liu et al. [223], who reported no significant differences compared to fully turbulent inlet conditions.

For the simulation of this burner, the SDM model (described in Sec. 3.1.1) was used for Flame A, whereas the FGM model was used for Flame L. This choice was made because, as explained by [87], the lifted flame evolves mainly in the partially premixed regime where the FGM model performs better than an approach for non-premixed flames only. Large-eddy simulations were carried out using a time step of 1×10^{-7} s. Table 5.2 provides the boundary conditions together with the corresponding boundaries shown in Fig. 5.5.

Validation against experiments is conducted using time-averaged and root-mean-

HYLON Boundary Conditions	
H2 Stream	Velocity Inlet (profile)
Air Stream	Velocity Inlet (profile)
Combustion Chamber	No-Slip Wall
Inlet Duct	No-Slip Wall
Plate	No-Slip Wall
Outlet	Pressure Outlet

Table 5.2: HYLON Boundary Conditions

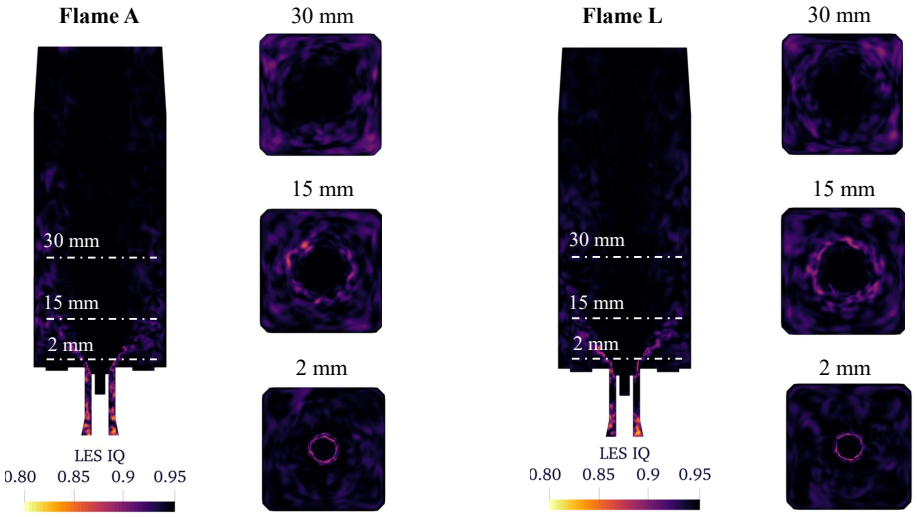

Figure 5.6: HYLON contour plot of the Cèlik criterium for LES quality in the reactive flow of the anchored flame (left) and lifted flame (right).

square (RMS) profiles of axial and radial velocity components. Figure 5.5 identifies the extraction locations for experimental data in both cold and reactive flow simulations. Additionally, OH* chemiluminescence measurements are compared against the time-averaged OH* mass fraction from LES. An analysis of the resolved and modeled turbulent kinetic energy in the reactive flow simulation for both flame A and L is reported in Fig. 5.6.This analysis demonstrates that more than the 80% of the kinetic energy was solved throughout the computational domain.

5.3 Results and Discussion

5.3.1 NTNU case

Time-averaged and RMS profiles of axial and radial velocity components at various axial locations are compared against experimental data in Figs. 5.7 and 5.8. The simulations show good overall agreement with measurements, accurately capturing the peak values of both time-averaged axial and radial velocity components as well as

the RMS fluctuations. Furthermore, by comparing the axial velocity of the cold and reactive cases (see Fig. 5.8), an increase in the extent of the inner recirculation zone (IRZ) due to the combustion process can be observed.

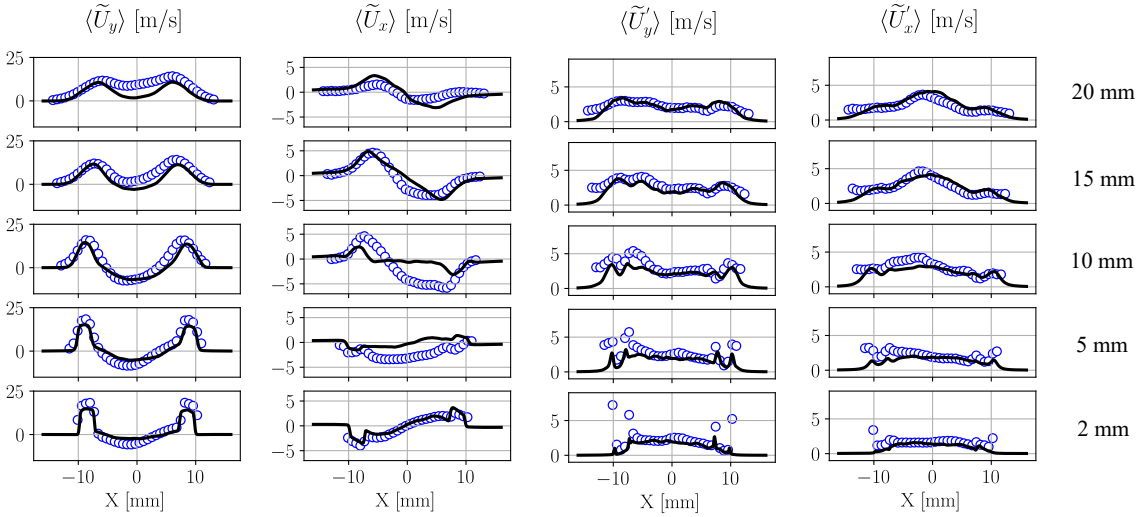

Figure 5.7: NTNU cold flow simulation (LES: ━, Exp: o)

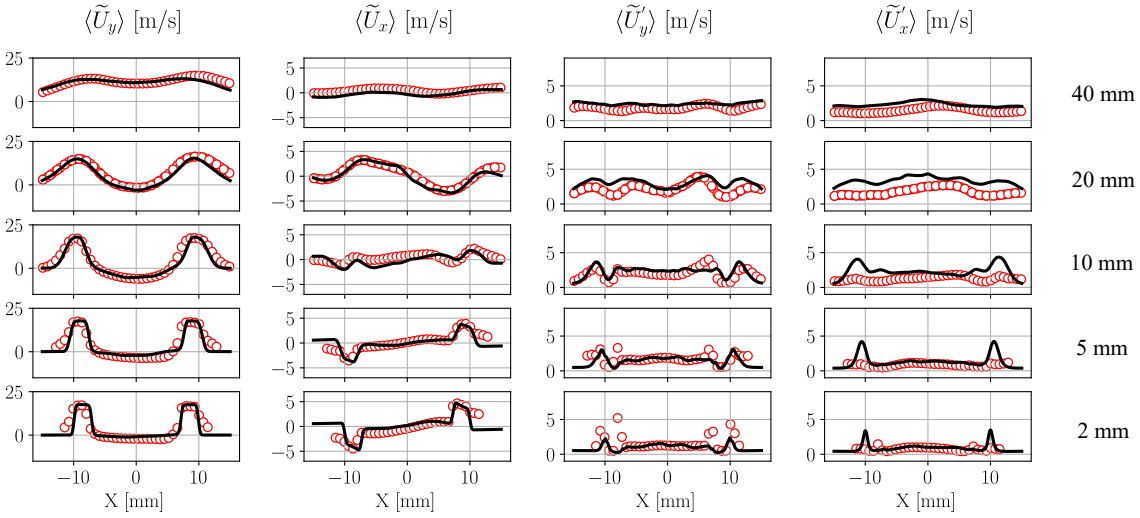

Figure 5.8: NTNU reactive flow simulation (LES: ━, Exp: o)

Regarding velocity fluctuations, the LES accurately reproduces the evolution of RMS values for both axial and radial components in the cold flow. In the reactive case, however, the RMS of the radial velocity component in the shear layer is overpredicted, with a similar discrepancy observed in the central region at an axial height of 20 mm as also observed in [224]. These fluctuations in reacting flows arise from the strong coupling between flow dynamics and density/composition variations induced by combustion. Capturing such unsteadiness remains challenging across different modeling frameworks. While the proposed approach reliably predicts time-

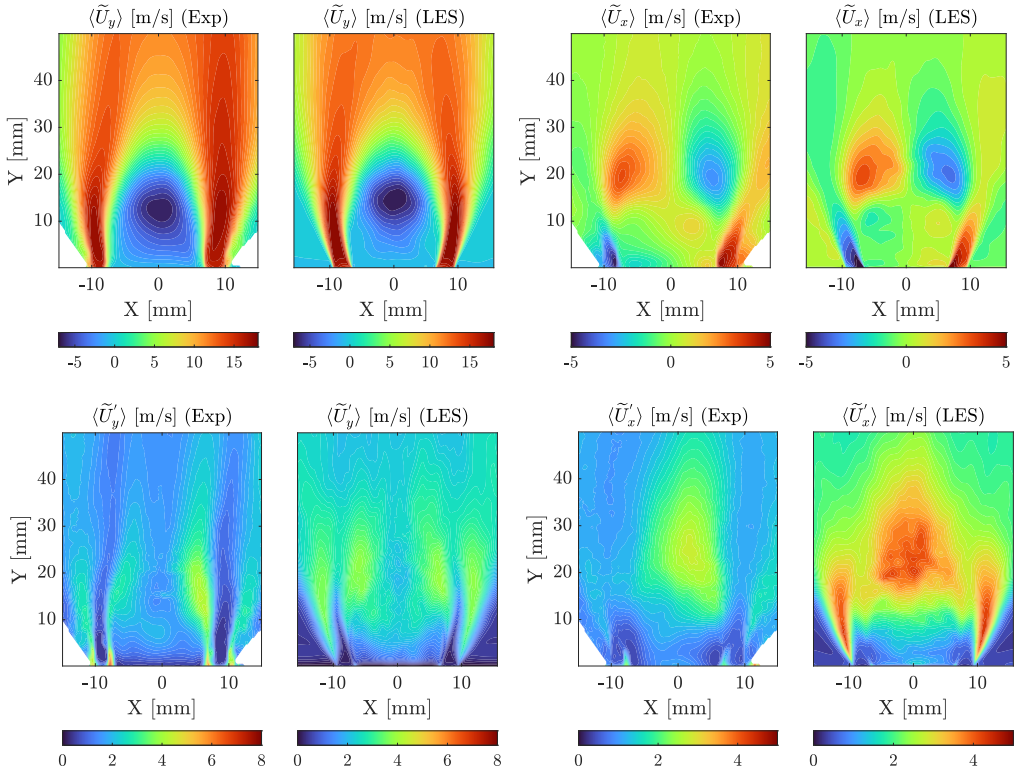

Figure 5.9: Contour plot of time averaged and RMS velocities compared to the experimental data.

averaged flow features, further refinements may be needed to improve fluctuation predictions. Figure 5.9 presents time-averaged velocity components and RMS fluctuations in a cross-sectional plane through the bluff-body centerline, compared against experimental data. Consistent with the centerline profiles, mean velocity components are captured with good accuracy. The RMS fluctuations, however, exhibit overprediction both in the shear layers at the bluff-body and annular duct edges, and in the central wake region downstream of the bluff-body. Similar trends have been reported in other studies of bluff-body stabilized flames, e.g., Ref. [228].

Regarding the prediction of the flame structure, Fig. 5.10 shows a comparison between the experimental data of OH* Chemiluminescence and the time averaged normalized heat release rate (HRR). Figure 5.10 also shows a comparison between the experimental data for OH-PLIF and the time averaged OH mass fraction. The flame predicted by the simulation appears thinner and longer than the one observed in the experiments. It is worth noting that the FGM model in its basic formulation implemented in ANSYS FLUENT does not include the effects of stretch and differential diffusion. As discussed by Klarmann et al. [229], the shape of the flame can be more accurately predicted if these effects are included in the construction of the look-up table. Moreover, as found by Liu et al [224], considering differential diffusion effects leads to a more diffusive transverse distribution of OH as in the measurements. Future work will involve implementing more accurate models that can account for the

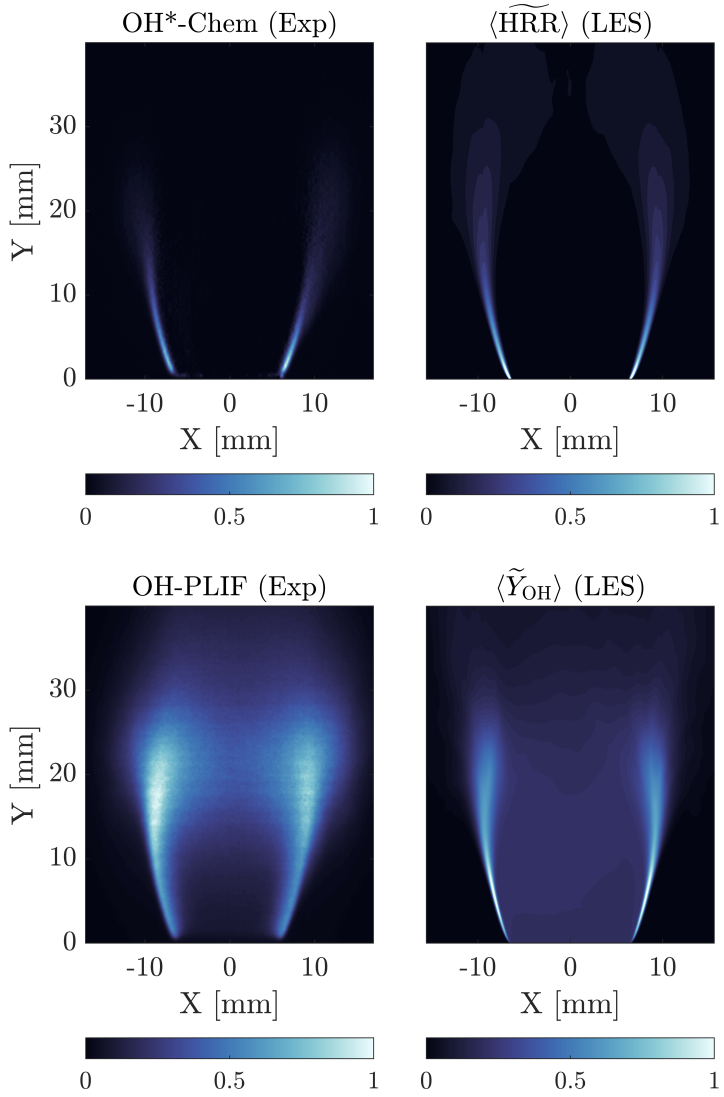

Figure 5.10: Top: comparison between OH* Chemiluminescence and time-averaged normalized HRR. Bottom: comparison between OH PLIF and time averaged OH mass fraction.

effects of stretch and differential diffusion models in order to compare the different approaches. To further investigate the flame characteristics, the Takeno Index [230] was used to differentiate regions of the flame burning in premixed or non-premixed mode. Fig. 5.11 shows the instantaneous contour plot of the flame index. A value of +1 indicates premixed combustion, while a value of -1 corresponds to non-premixed combustion. The combustion regime is fully premixed over the entire flame region and this allows the FGM model to perform at its best since the look-up table was built with premixed flamelets.

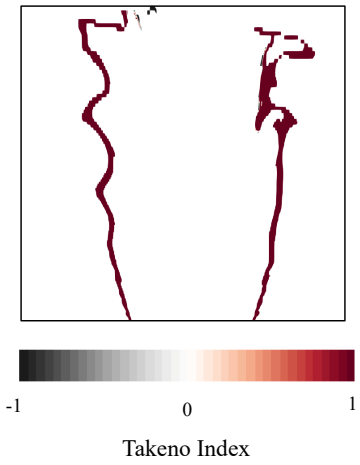

Figure 5.11: Instantaneous contour plot of the Takeno Index. A value of +1 indicates premixed combustion, while a value of -1 corresponds to non-premixed combustion.

5.3.2 HYLON case

Figures 5.12 and 5.13 show the comparison between experimental and numerical velocity components for cold and reactive flows, respectively. Results show that the model is able to predict the axial and radial velocity components in both operating conditions. This means that the shape of the IRZ as well as the swirled motion are captured by the model. The RMS of the velocity fluctuations is also well predicted both for the radial and axial velocity components. These results suggest that the LES framework used in the present study is able to capture the variations in the velocity flow field between the cold and reactive flow, caused by the thermal expansion of gases.

Table 5.3 compares experimental outlet gas temperatures with time-averaged LES predictions from the present work and the ones reported by Aniello et al. [217]. The LES-flamelet model overpredicts the temperature for Flame A, while predictions for Flame L closely match the experimental value. Enthalpy losses are neglected in this study due to the absence of detailed thermal boundary conditions from experiments, particularly at the fuel injector lip. Radiative heat transfer is also omitted. To identify

Flame	T_{exp} [K]	T_{TF} (Aniello et al.) [K]	T_{CFD} [K]
A	1138	1010 (-11%)	1338 (+17%)
L	1280	1100 (-16%)	1246 (-2.6%)

Table 5.3: Mean temperature at the burner's exhaust for the HYLON test case. Mean temperature of gases at the outlet: T_{exp} indicates the temperature measured in the experiment; T_{CFD} are the results from the simulations performed in the present work; T_{TF} indicates the results obtained by Aniello et al. [217].

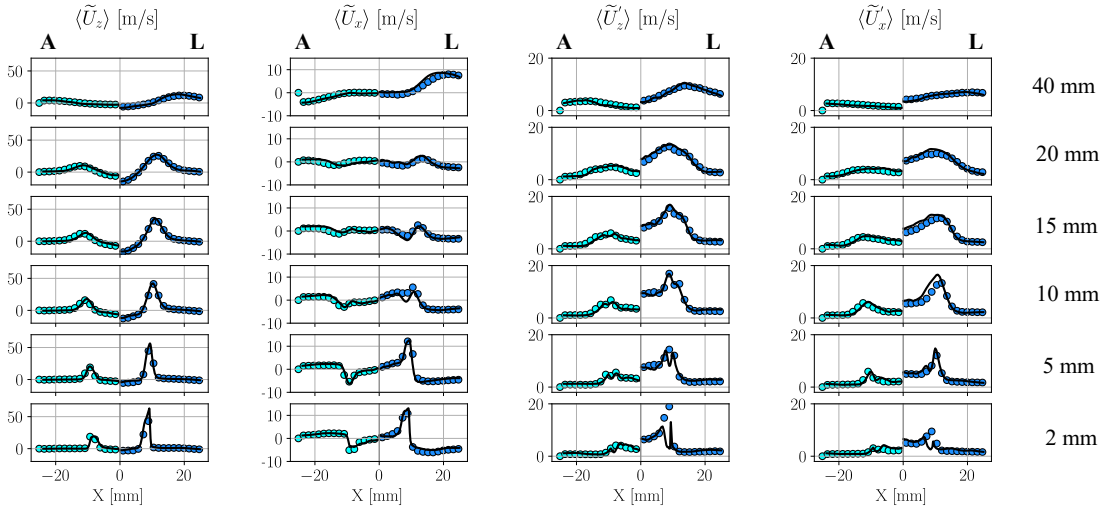

Figure 5.12: HYLON cold flow simulation of both A (left) and L (right) configuration (LES: ━, Exp: circles).

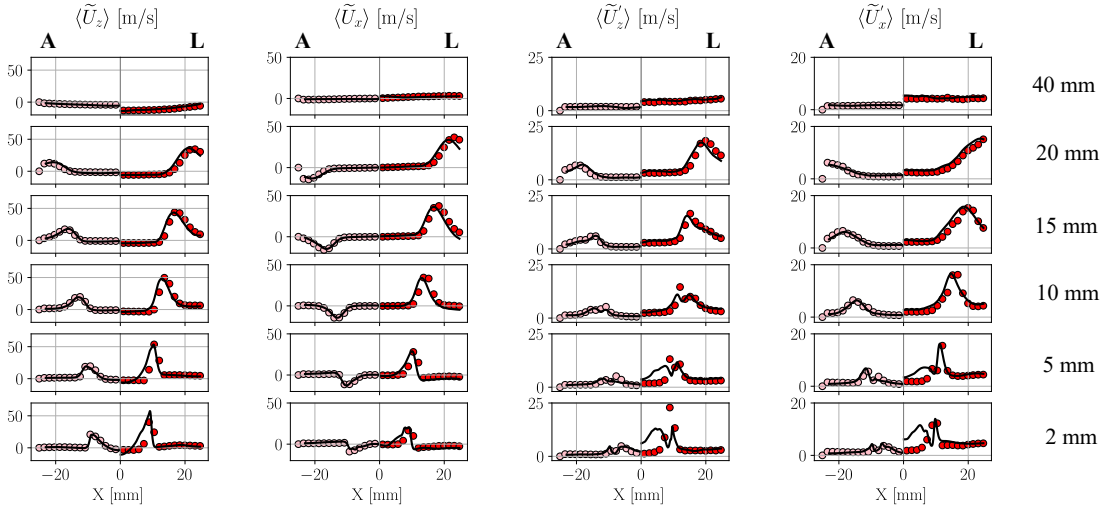

Figure 5.13: HYLON reactive flow simulation of both A (left) and L (right) configuration (LES: ━, Exp: circles)

local combustion regimes, an instantaneous contour plot of the Takeno index is presented in Fig. 5.14. Unlike the NTNU configuration, the HYLON flame exhibits multiple regimes, encompassing both premixed and non-premixed combustion. This mixed-mode behavior complicates predictions, as flamelet tables are constructed using either premixed or non-premixed manifolds alone. The coexistence of multiple regimes along the flame front can degrade accuracy when relying on a single-mode lookup table [231]. Combined with inherent flamelet model limitations, such as the presumed PDF approximation and reduced fidelity near walls [232], these effects likely contribute to the temperature discrepancies observed for the attached flame.

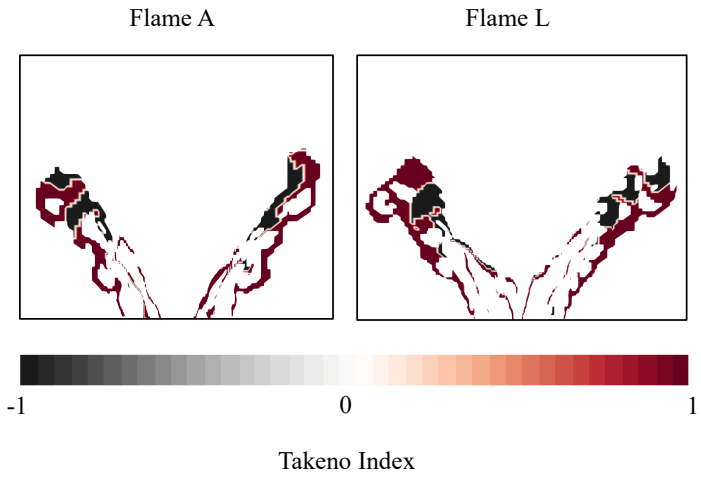

Figure 5.14: Instantaneous contour plot of the Takeno Index for both the flames A (left) and L (right). A value of +1 indicates premixed combustion, while a value of -1 corresponds to non-premixed combustion.

As far as the flame structure is concerned, Fig. 5.15 shows a comparison between measurements and numerical predictions of OH*. Overall, the model is able to correctly predict the shape of the visible flame, reproducing the regions of high heat release rate along the shear layer. The absence of OH* in the recirculation region of Flame A is also well predicted. For Flame L, the model successfully predicts a thicker flame, a larger region of high heat release rate extending further downstream of the fuel injector, and the presence of OH* in the region above the injector. However, some discrepancies between experiments and simulations are observed regarding the extent of the area with OH* presence and the angle between the burner axis and the line where a greater release of OH* is observed (see Fig. 5.15).
As discussed in [87], where the LES-TFUP model is presented, a lifted flame can move upstream only if two conditions are met: (i) a flammable mixture fraction line Z_0, that represent the edge flame propagation line, between the flame and the injector exists and (ii) the mixture fraction Z_0 is located, from the flame to the injector lip, in a zone where the projection of the local velocity u_t along this line is lower than its propagation velocity s_d. The edge flame speed s_d on the Z_0 line is calculated as follows:

$$s_d = {s_l}^0 \left(\frac{\rho_u}{\rho_b} \right)^{1/2} \tag{5.3}$$

where ${s_l}^0$ is the maximum laminar flame speed and ρ_u/ρ_b is the volumetric expansion ratio of the gas through the flame for Z_0. The mixture fraction Z_0 in most cases is equal to Z_m associated to the maximum laminar burning velocity and maximum

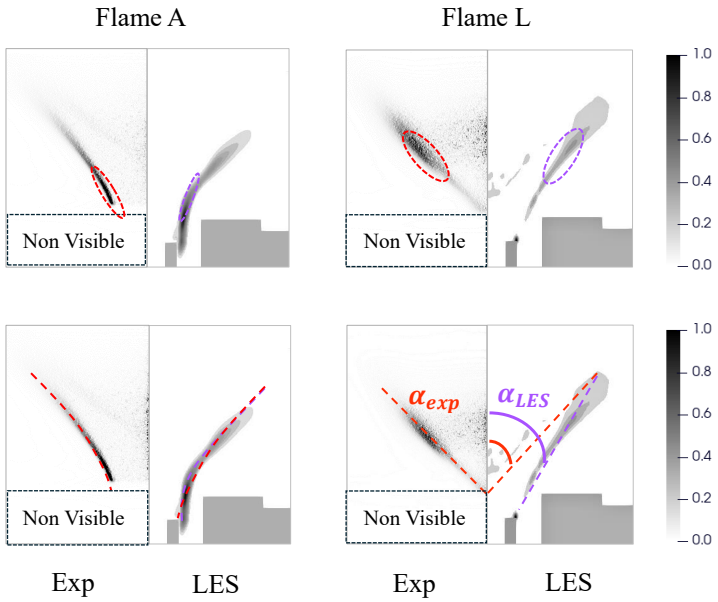

Figure 5.15: Comparison between the experimental data (- - -) and the time-averaged OH* mass fraction (- - -). In the two figures at the top the zones with the largest release of energy due to combustion are highlighted. The figures below show a comparison of the opening angle of the flame α between the experimental data α_{exp} and numerical results α_{LES}.

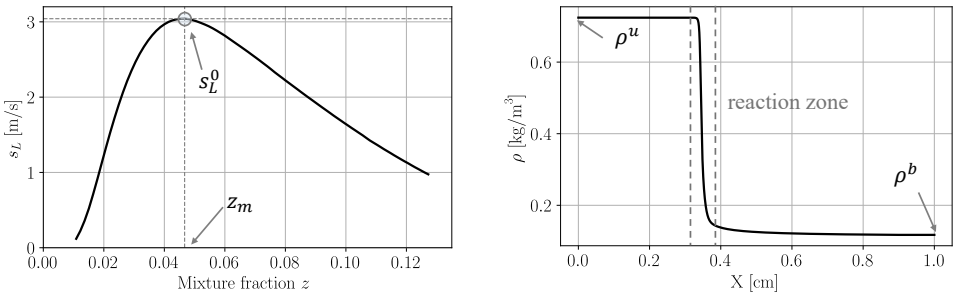

Figure 5.16: Cantera simulations of the freely propagating premixed flames for the calculation of the s_d. The top figure on shows the calculation of the maximum burning laminar velocity $s_l{}^0$. The figure below shows the calculation of the volumetric expansion ρ_u/ρ_b of the gases due to the combustion process for a freely propagating premixed flame with a mixture fraction of Z_m .

triple flame speed. These quantities have been calculated with Cantera [149] using a freely propagating hydrogen flame and the reduced GRI mech 3.0 (9 species 29 reactions).

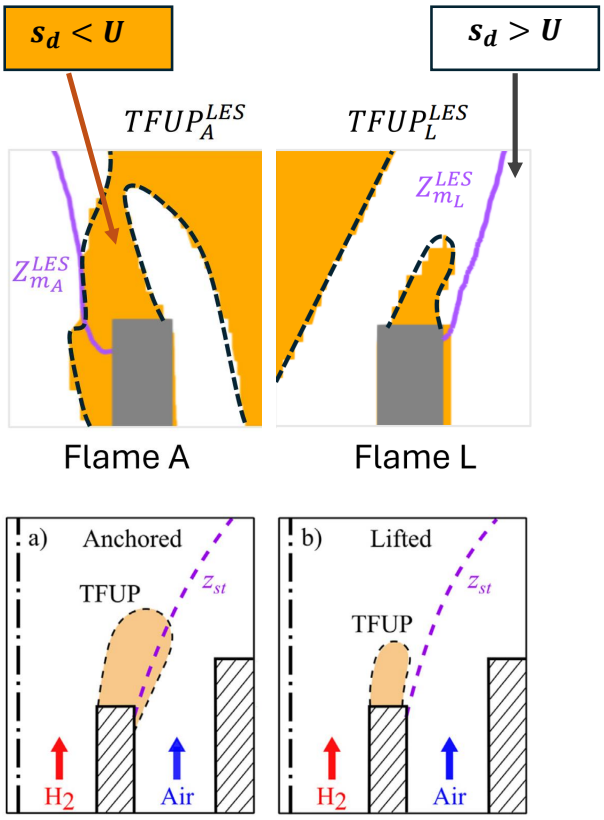

Figure 5.17: TFUP model proposed by Marragou et al [87] (bottom) together with the results of LES simulation (top). The purple line (—) represents the isoline of the mixture fraction at which the maximum laminar burning velocity occurs. The TFUP is colored in orange and represents the zone of the flow where the mean axial velocity is lower than the triple flame speed s_d.

First, the laminar flame speed was calculated for different compositions of the mixture to determine the maximum laminar flame speed, obtaining a value of 3.04 m/s as shown in figure 5.16.a. From the value of maximum laminar flame speed and the mixture fraction at which this value occurs ($Z_m = 0.047$), another freely propagating flame at the mixture fraction Z_m was simulated to find the volumetric expansion ratio of the gas ρ_u/ρ_b, obtaining a value of 5.91 as highlighted in figure 5.16.b. The edge flame speed s_d is at this point calculated and equal to 7.39 m/s. Once this value is determined, it becomes possible to verify whether the conditions for obtaining a lifted flame are satisfied. As shown in Fig. 5.17, the purple line, representing the isocontour of Z_m, intersects the TFUP region for Flame A and slightly intersects the TFUP region near the fuel injector external wall, not allowing the flame to fully detach from the fuel injector wall (as also observed in Fig. 5.15). This calculation illustrates how the LES predictions align with experimental observations regarding the occurrence of an anchored or lifted flame. However, predicting the flame lift-off remains challenging

and further improvements on the model and thermal boundary conditions may be needed.

5.4 Summary and Conclusions

Premixed and non-premixed hydrogen flames were investigated using LES and flamelet models with the main aim of assessing the capability of the simulations to predict the flame structure and characteristics of the reacting field in two different regimes. Numerical results show that the flamelet models are able to capture with good accuracy both the turbulent field and flame structure. In the premixed configuration, results demonstrate that the LES-FGM approach provides a good prediction of the flow field measured in the experiment. The agreement between experimental and numerical data is better in the reactive case compared to the isothermal conditions. In addition, the model is able to capture the flame location and shape, although some discrepancies arise in the prediction of the thickness of the flame brush. As far as the non-premixed flame is concerned, results show a better agreement with the experimental data compared to the premixed case. The model is able to predict the velocity field in both the non-reactive and reactive flow, with only some discrepancies in the prediction of the velocity fluctuations in the inner recirculation zone. The flamelet models used in these simulations are able to predict the shape of the flame and the peak location of heat release rate. Considering the prediction of the flame shape, the simulation has turned out more accurate for the anchored configuration than for the lifted one. Conversely, the most accurate prediction of the averaged static temperature at the exhaust was obtained for the lifted flame. The outcomes of this study comprehensively validate LES and flamelet methods, contributing to a more informed selection of numerical frameworks for industrial simulation scenarios.

6 Investigation of Differential Diffusion and Strain Coupling in LES of Hydrogen Premixed Flames

In the previous chapter, premixed and diffusion flames were investigated. However, differential diffusion effects were not included, as the model implemented in ANSYS Fluent did not account for such effects. Since molecular diffusion effects associated with different Lewis numbers are crucial in lean premixed hydrogen flames, the model described in Chapter 3, implemented in the open-source code OpenFOAM by Ferrante et al. [203], is employed here to investigate the NTNU case. In this chapter large eddy simulations with flamelet-based thermochemistry are used to investigate the behavior of a premixed hydrogen-air flame stabilized by a bluff-body. Validation against experimental data is carried out first to demonstrate the model's ability to predict both velocity field and flame structure. The capability of the model in predicting differential diffusion effects is then assessed, in particular regarding the coupling between differential diffusion, tangential strain and curvature, and their effect on mixture fraction redistribution and reaction rate variation.

6.1 Introduction

Among the most widely used closures for turbulence-flame interaction in premixed flames, flamelet-based methods have found broad application in LES of hydrocarbon combustion, providing a good compromise between computational expense and predictive fidelity. These approaches, however, were primarily derived assuming equal diffusivities across species and thus fail to account for differential diffusion effects and their interaction with stretch effects that are crucial in hydrogen flames even under moderate straining [161]. Flamelet formulations can accommodate one-dimensional phenomena, like preferential mixture enrichment ahead of

the flame, through targeted modifications to the transport equations for mixture fraction, progress variable, and enthalpy in LES. Capturing two-dimensional strain and curvature impacts, however, remains considerably more challenging [202, 233, 234].

Recent research has focused intensively on developing and analyzing canonical combustion test cases to enhance the understanding of hydrogen flame physics and inform combustion modeling. Key examples include the lifted partially premixed jet in hot coflow [235], low-swirl burner setups explored in [236, 237], the HYLON swirl-stabilized burner [238, 239], and NTNU unconfined bluff-body configuration [91]. The NTNU burner stands out for investigating differential diffusion coupled with stretch effects, given its lean premixed hydrogen flame subject to both strain and curvature. In its confined counterpart, recent work has highlighted the role of preferential diffusion in ignition processes [97] and the impacts of stretch combined with heat losses on hydrogen-mixed flames [219, 220]. Nevertheless, the coupled dynamics between differential diffusion and stretch, especially its tangential strain component, and their implications for flamelet-based approaches, are still not fully understood.

This study examines the NTNU unconfined configuration using a flamelet model coupled with a presumed filtered density function (FDF) closure recently adapted to incorporate differential diffusion [203]. This adaptation extends the laminar flamelet approach from [202] to LES within a presumed FDF structure. The resulting model has been shown to capture fluctuations in the local equivalence ratio at the resolved scale that arise from the combined influence of differential diffusion and flame curvature, driven by turbulence and thermodiffusive instabilities. Whether it can also account for tangential strain effects, however, remains unresolved.

Given that strain and curvature dominate premixed hydrogen flames alongside differential diffusion, combustion models must accurately capture their combined influence. This raises the question of whether an unstrained, one-dimensional flamelet database, as opposed to a database including strained flamelets, is sufficient to capture the influence of strain on flame dynamics. While the one-dimensional nature of an unstretched flamelet suggests that this may not be feasible, the answer is not straightforward. At the macroscopic level, and similarly to a curved flame, the thermochemical state of a strained flame is governed by the balance between convection and diffusion. A modeling framework for LES that can reproduce this balance might, in principle, recover the correct thermochemical state starting from an unstretched flamelet manifold.

For hydrocarbon flames, previous studies [240] demonstrate that strained flamelets prove unnecessary when most strain is resolved directly, even with local extinction [196, 199]. For hydrogen premixed flames, Berger et al. [138] showed that mixture fraction as a control variable enhances thermochemical state representation in turbulent jet flames more than curvature, stretch, or strain. Conversely, the *a priori* DNS analysis by Böttler et al. [241] indicated that strain and curvature vari-

ations in flamelet tables span the full thermochemical range, although deviations from unstretched (mixture-fraction-based) libraries mainly affected minor species, with major species, temperature, and reaction rates showing smaller errors. Recently, Berger et al. [242] evaluated an LES flamelet model with preferential diffusion using unstretched premixed flamelets at varying equivalence ratios; their findings confirm that such manifolds capture differential diffusion effects and their interaction with front curvature (from thermodiffusive instabilities), turbulence, and turbulence-driven strain.
In view of these findings, it remains uncertain whether, in configurations dominated by intense strain, the combined influence of strain, curvature, and differential diffusion on the spatial distribution of mixture fraction and peak reaction rate can be represented solely through the resolved strain in LES when employing a database of unstretched flamelets. In contrast to the slot-burner flame examined in [242], the bluff-body stabilized flame considered here is characterized by relatively high mean strain rates compared to curvature, and therefore provides a suitable test case to assess the applicability of unstretched flamelet libraries in such regimes.
The objectives of this work are therefore twofold: (i) to validate the flamelet model for the NTNU unconfined configuration against the available experimental measurements (PIV and OH* chemiluminescence) and to carry out a detailed numerical characterization of the flame; and (ii) to evaluate the model performance in capturing, at the resolved scale, the effects of differential diffusion and strain on flame behavior when relying on a flamelet database constructed from unstrained premixed flamelets with varying equivalence ratio.

6.2 Numerical Methods

The computational domain starts downstream of the three cylinders positioned 65 mm upstream of the bluff-body base. The open region around the bluff body is represented as a cylinder with diameter $d = 100$ mm and height $h = 100$ mm. The domain employs 2.5 million hexahedral cells, with boundary layer refinement to maintain $y^+ < 1$. In the reaction zone, cell sizes vary from 35 μm minimum to 400 μm maximum, averaging about 100 μm and equivalent to roughly 6.5 cells across the laminar flame thickness. Mesh quality was evaluated via the Cèlik criterion [227] to ensure that at least 80% of turbulent kinetic energy across the domain was captured. Fig. 6.1 (right) displays a cut plane of the mesh and applied boundary conditions.
The Favre-filtered Navier Stokes equations under low-Mach approximation are solved using the finite volume method in OpenFOAM-v9. A constant time step of 3×10^{-7} s is used to ensure the Courant number remains below 0.5 in every cell of the computational domain. The Pressure Implicit with Splitting of Operators (PISO) algorithm is selected for the pressure-velocity coupling and an implicit Euler scheme is used for the temporal discretization. The thermochemical database is built on a

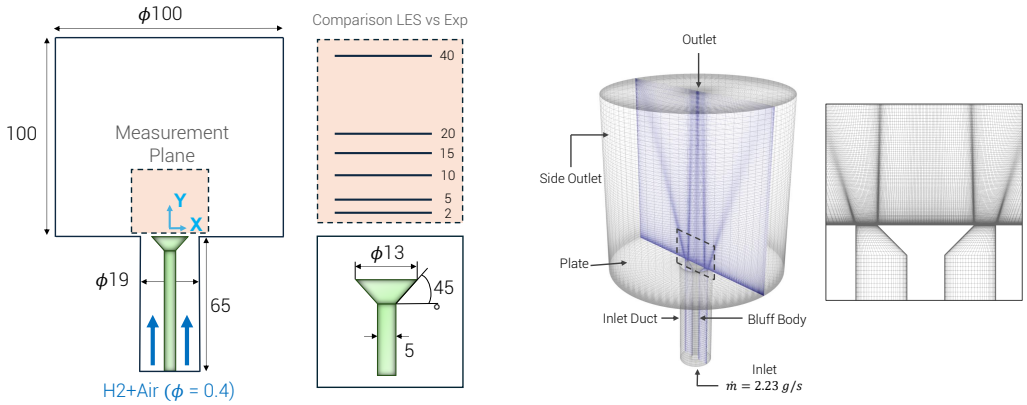

Figure 6.1: Schematic of the NTNU premixed hydrogen burner (left), and corresponding numerical mesh and boundary conditions (right). All dimensions are reported in mm.

set of freely propagating premixed hydrogen-air 1D flamelets at atmospheric pressure, with reactants temperature of 300 K and the mixture fraction in the reactants spanning the flammability range $z \in [0.007,\ 0.17]$. The 1D flamelets solutions are computed using the one-dimensional solver CHEM1D [243] and the Burke mechanism [244] (11 species and 21 reactions) is used as reaction mechanism. The 4D flamelets database needed for the FDF approach is discretized with $n_c = 100$ equispaced points between 0 and 1 for the progress variable space, and $n_{\sigma_c^2} = 50$ points between 0 and $\widetilde{c}(1-\widetilde{c})$ for its subgrid variance space. The filtered mixture fraction space spans the flammability range, and a total of $n_z = 98$ equispaced points is used. A total of $n_{\sigma_z^2} = 15$ points are used for the mixture fraction subgrid variance, spanning exponentially the range $[0, \widetilde{z}(1-\widetilde{z})]$. Boundary conditions are assigned as follows and highlighted in Fig. 6.1. At the domain inlet, a mass flow rate of $\dot{m} = 0.00229$ kg/s with a value of mixture fraction of $z = 0.0125$ is imposed, which corresponds to the nominal theoretical power $P_{\text{th}} = 3.5$ kW. Zero normal velocity gradients and total pressure corresponding to the atmospheric pressure are prescribed at the outlet(s) of the computational domain. The simulation is initialized with a mixture fraction equal to zero (representing air at 300 K) throughout the entire domain. Once the flow has convected the mixture fraction field downstream the bluff-body, a patch with progress variable $c = 1$ is imposed near the bluff-body to ignite the mixture.

6.3 Results and Discussion

6.3.1 Validation and flame structure

Comparisons between LES and experimental measurements of time-averaged and RMS axial and radial velocity components at various streamwise (axial) locations for the non-reactive and reactive flow are shown in Fig. 6.2 and Fig. 6.3 respectively. For the reactive case, both the cases with and without differential diffusion are reported,

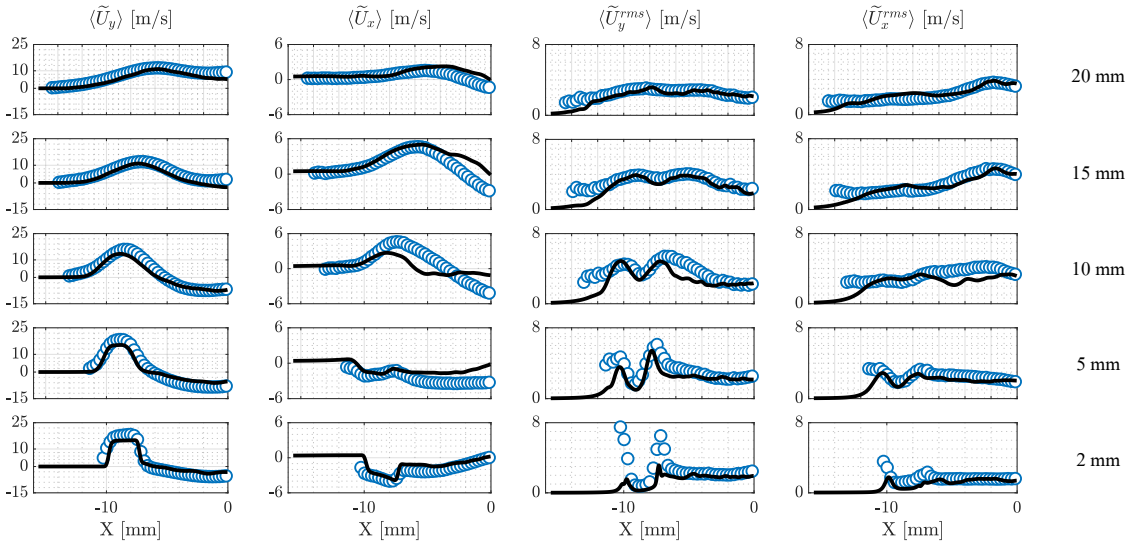

Figure 6.2: Radial profiles of axial and radial velocity, and their RMS, at different axial locations for the non reactive flow. (LES: ━, Exp ○)

showing no significant differences in mean velocity flow field and RMS between the two models.

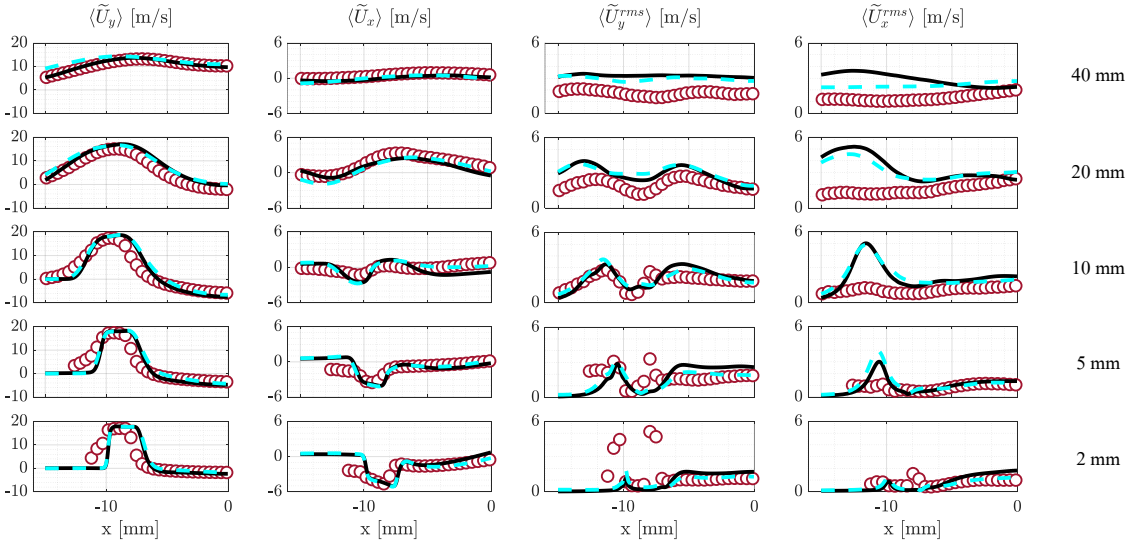

Figure 6.3: Radial profiles of axial and radial velocity, and their RMS, at different axial locations for the reactive flow. (LES with $\mathrm{Le}_k = 1$: ━, LES with $\mathrm{Le}_k \neq 1$: ┈┈, Exp ○)

The simulations results align well with the experimental data, particularly in capturing the peaks of both velocity components and RMS fluctuations. However, some overestimation of the RMS of radial velocity is observed in the region of the shear layer around a height of 20 mm as also observed in [224]. This could be related to the fact that subgrid scales are affected by thermal dilatation effect in the flame normal direction, which is not taken into account in the estimation of these RMS. This argument is further suggested by the fact that the RMS of radial velocity was ob-

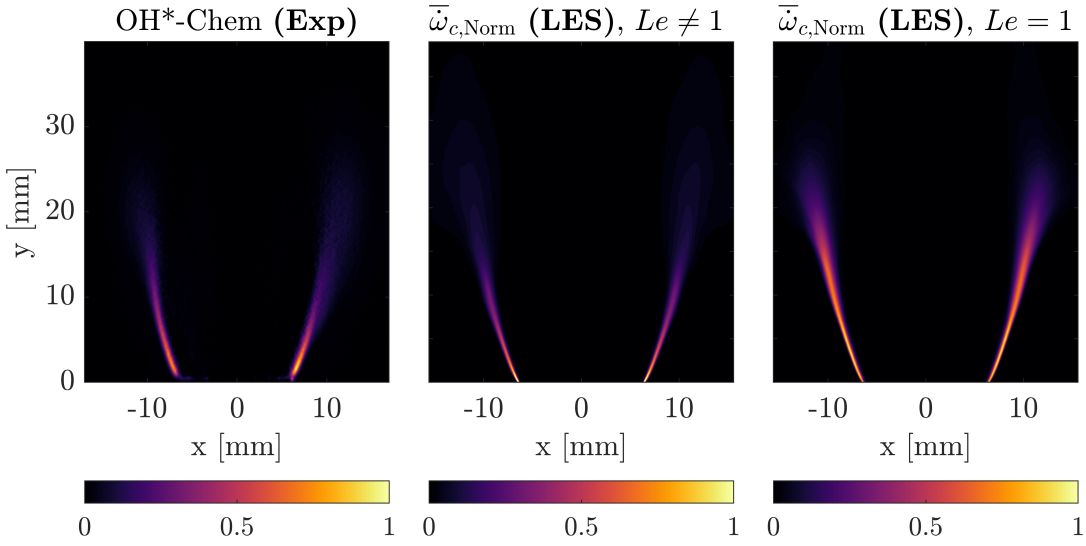

Figure 6.4: OH*-Chemiluminescence from experiments [245] (left) and midplane contours of tome averaged progress variable reaction rate obtained from LES results with (centre) and without (right) differential diffusion effects. All plots are normalized: experimental results have been normalized by their respective maximum OH*-Chem value, while the numerical results have been normalized by the maximum value of the $Le = 1$ case.

served to better match the experimental measurements in the non-reacting case as it can be observed in Fig. 6.2. Also, comparisons of OH*-Chem measurements with time averaged reaction rate from LES, shown in Fig. 6.4, indicate that the LES accurately predicts both the shape and length of the flame. It can be further observed that the location of highest reaction rate moves towards the edge of the bluff-body when differential diffusion effects are included in the model, and the comparison with experimental data improves in this case.

Further insight on the effects of differential diffusion is presented next. For an unstretched premixed flame, a decrease in mixture fraction is expected in the preheat zone ahead of the flame, followed by a re-increase in the flame region [**138**, **246**]. This behavior, categorized in the Introduction as a one-dimensional effect, is captured by the LES with differential diffusion model, as demonstrated in Fig. 6.5 by the presence of a region of mixture fraction with values around $\tilde{z} = 0.011$, which are lower than the nominal value $\tilde{z} = z_{nom} = 0.0125$. In fact, since the resolved curvature in this region is small and the positive resolved strain in the same region would increase the mixture fraction when compared to an unstrained case [**246**], the observed low values of $\widetilde{z}$ necessarily imply that one-dimensional effects of differential diffusion are captured in the LES. Besides, the LES with differential diffusion model also predicts a significant increase in mixture fraction in the post flame region ($\tilde{c} > 0.5$), above its nominal value. This increase is only possible due to the combined effects of stretch and differential diffusion (positive strain and curvature), as documented in previous studies

[138, 234, 246]. This implies that the LES with unstretched flamelets thermochemistry can, at least qualitatively, mimic this interplay between resolved stretch and differential diffusion (multi-dimensional effect as categorized in the Introduction). As a consequence of this enrichment, the LES also predicts superadiabatic temperatures, with peaks around $\tilde{T} = 1800$K observed in the region of the flame anchoring point (Fig. 6.5, right). These peaks are found to correspond to values of progress variable $\tilde{c} > 0.85$. Consistently, a redistribution of the reaction rate field is predicted with respect to the unity Lewis number case, with higher values concentrated close to the flame anchoring point, also resulting in a shorter flame as observed with reference to Fig. 6.4. The above analysis highlights significant effects of differential diffusion in the studied configuration. Nevertheless, it has not yet been clarified how the balance between strain and curvature is affecting the interplay between stretch and differential diffusion, and how the current modeling framework based on unstretched flames thermochemistry is capturing this interplay. Insights on this aspect are provided in the next section.

6.3.2 Average resolved stretch effects

In premixed flames, differential diffusion effects are tightly coupled with flame stretch K. This can be split into contributions of flame front curvature k_f and flame tangential strain S_t as follows:

$$K = S_t + k_f s_d. \tag{6.1}$$

In particular, flame curvature induced either by turbulence or by intrinsic thermodiffusive instabilities, is positively correlated with variations in mixture fraction, such that a convex curvature towards the reactants causes mixture enrichment upstream of the flame, while a cusp (concave towards reactants) produces a mixture fraction decrease [141, 247]. Similarly, positive flame tangential strain produces a mixture enrichment when coupled with differential diffusion [246]. The contours in Fig. 6.6 indicate a region of intense positive tangential strain rate $\langle \tilde{S}_t \rangle \approx 7500\,1/\mathrm{s}$ being generated at the edge of the bluff body, where the flame anchors, due to the shear between the inlet flow and the recirculation region of hot gases.

The same figure reports radial profiles of mean flame tangential strain in progress variable space at different axial locations. As one would expect, tangential strain decreases when moving downstream. Its peak location, found for mean progress variable values $\langle \tilde{c} \rangle > 0.8$, is also found to shift towards the product side as one moves downstream. The effect of mean resolved strain on mixture fraction is also visible in Fig. 6.6. Consistently with the study in [246], higher levels of strain observed near the bluff body base limit the (one-dimensional) differential diffusion effects on mixture fraction decrease in the low progress variable region, and enhance its re-increase for higher values of $\widetilde{c}$. This re-increase results in an overshoot of mixture

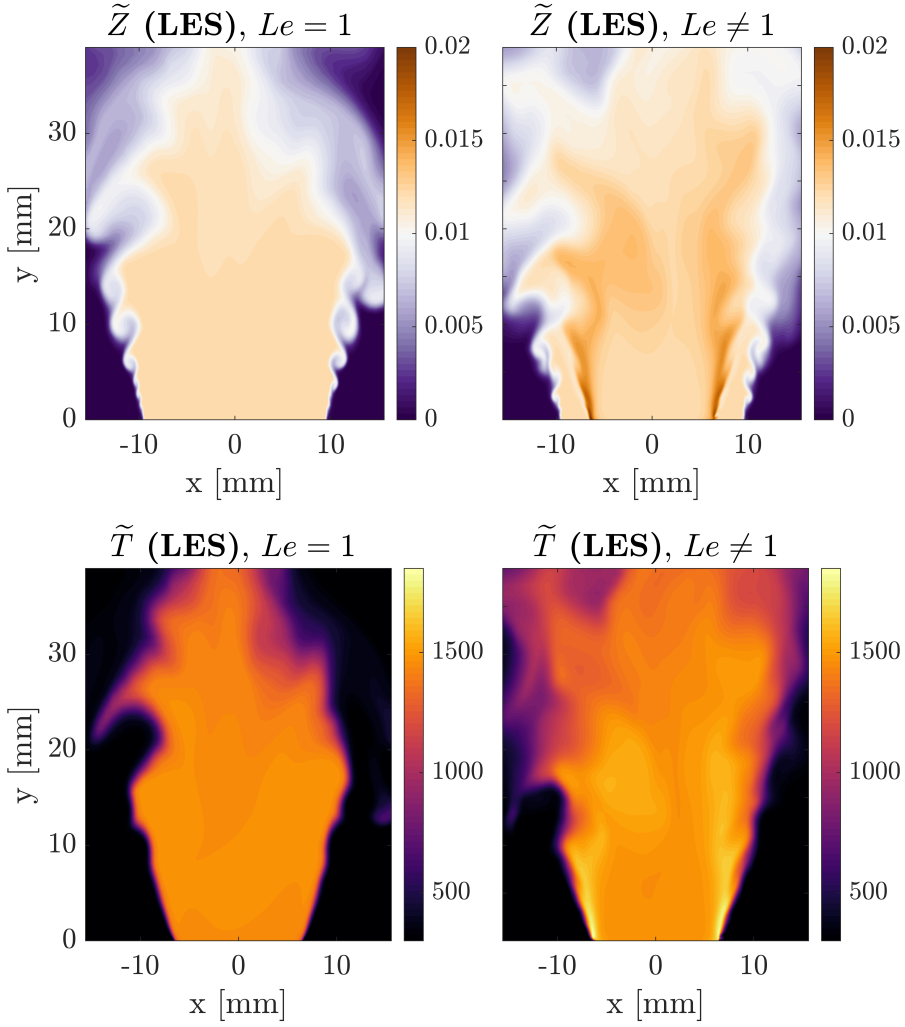

Figure 6.5: Midplane contours of instantaneous filtered mixture fraction (left) and temperature (right) obtained from the LES without (Le $=$ 1) **and with** (Le $\neq$ 1) **differential diffusion model.**

.

fraction above 50% in the region of higher strain, when compared to the nominal value. This in turns induces superadiabatic temperatures of the order of $\langle\tilde{T}\rangle \sim 2000$ K. This phenomenon, which is linked to the relative magnitude of convective transport with respect to diffusive transport of mixture fraction due to differential diffusion in strained flames, is thus correctly captured by the LES at the resolved level. In the present configuration, unlike what was observed by Berger et al. [138], strain appears to be the main responsible for mixture fraction variations, dominating over curvature effects. The comparison with the present bluff-body reacting dynamics further suggests that thermodiffusive instabilities, which played a major role in the slot burner [138, 203] for a similar equivalence ratio and massflow rates, are somewhat suppressed by the significant strain at the bluff-body base, consistently with [246, 248]. Figure 6.6 also indicates that not only the peak reaction rate, but also the

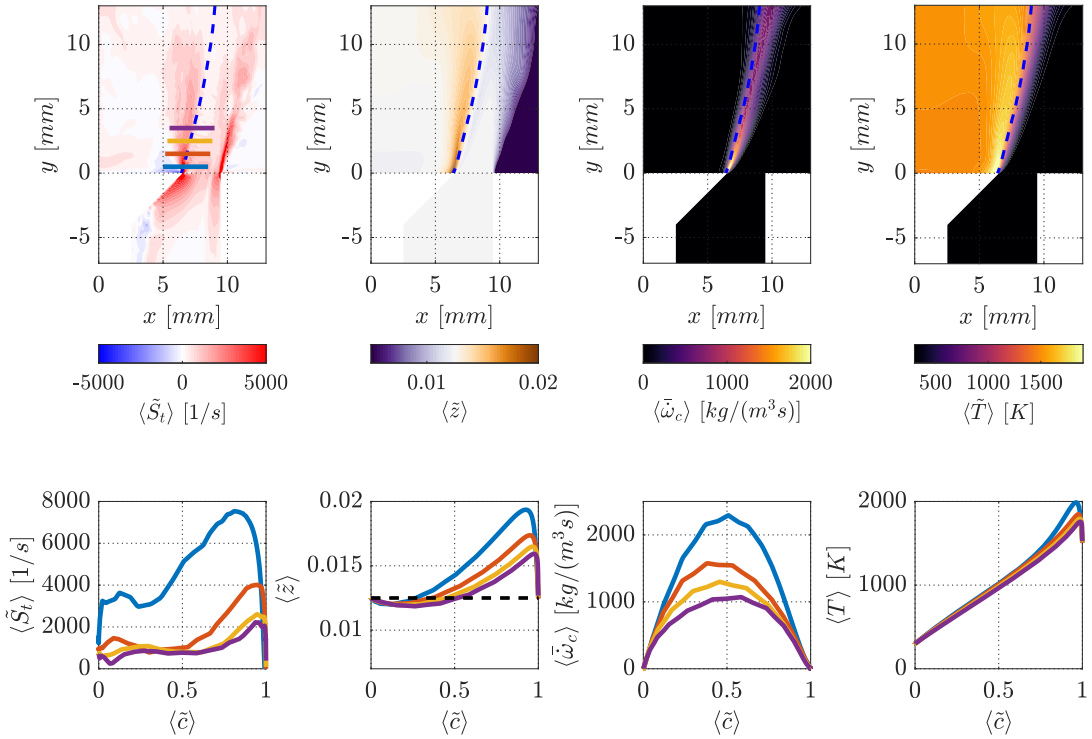

Figure 6.6: Top row, from left to right: Midplane contours of mean resolved tangential strain rate $\langle\tilde{S}_t\rangle$, mean mixture fraction, $\langle\tilde{z}\rangle$, mean progress variable reaction rate, $\langle\bar{\dot{\omega}}_c\rangle$, and mean temperature $\langle\tilde{T}_c\rangle$ obtained from LES with differential diffusion model. Isoline of mean progress variable $\langle\tilde{c}\rangle = 0.8$ is marked as a blue dashed line (····). Bottom row, from left to right: profiles of the same average quantities along the flame at the 4 axial locations marked in the A1 contour plot: $y = 0.5$ mm (—), $y = 1.5$ mm (—), $y = 2.5$ mm (—), $y = 3.5$ mm (—). The dashed line indicates the nominal mixture fraction value $z = 0.0125$.

extent of the area underneath the curve (which is proportional to the consumption speed in physical space), increases in correspondence of regions of higher tangential strain rates (see radial profiles). This is an expected effect of reacting mixtures at negative Markstein lengths [161], and suggests that capturing the correct redistribution of mixture fraction might be sufficient, in the context of flamelets combustion modeling, to predict the correct increase in reaction rates. This is further confirmed by the fact that the flame shape and length, thus the burning speed, is in very good agreement with the experimental observations (see Fig. 6.4), which is not the case without differential diffusion modeling. On the other hand, one has to keep in mind that strain effects on reaction rate are also linked to enthalpy and radicals redistribution through the flame front as indicated in the *a priori* analysis of [241]. In the latter, however, errors were observed to remain below 10% in terms of major species, temperature, density and reaction rates when using an unstretched flamelets database as compared to strained flamelets, with larger errors for minor species. Unfortunately, minor species mass fractions are not available in the experimental database for comparisons. Note that errors on minor species are commonly expected within flamelets

based approaches even for hydrocarbon flames, where additional transport equations and methods are often used to improve the accuracy of their predictions (e.g. see [249]). The above results suggests that effects of strain in lean hydrogen flames can be accurately predicted with unstretched flamelets thermochemistry, at least as long as most of the strain is resolved.

6.3.3 Reacting states

Figure 6.7 illustrates the joint probability density function of progress variable reaction rate $\bar{\dot{\omega}}_c$ and progress variable $\tilde{c}$ at a random timestep. Only points on the flame with $\bar{\dot{\omega}}_c > 1$ are considered.

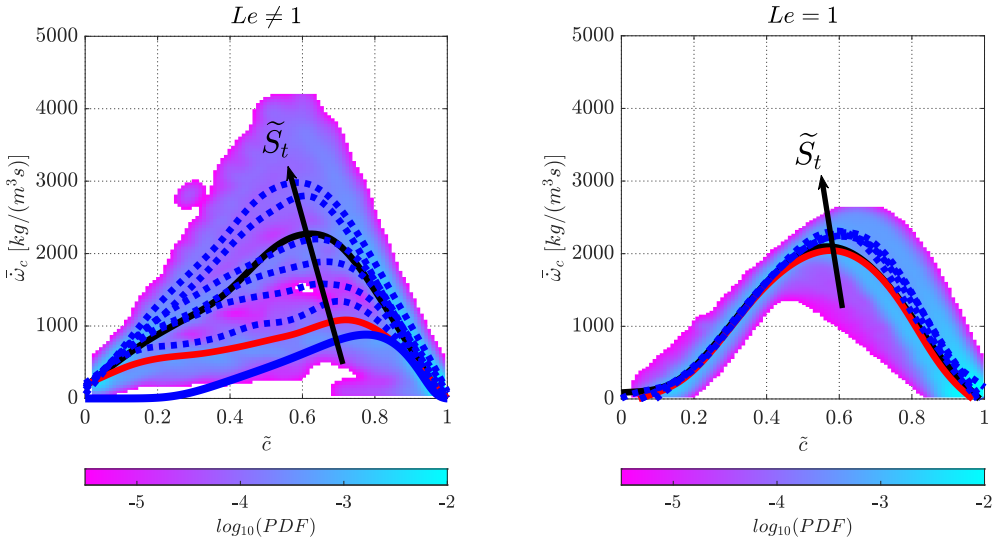

Figure 6.7: Joint probability density function of progress variable reaction rate versus progress variable at a random timestep. Both cases with (left) and without (right) differential diffusion are shown. Solid lines represent global conditional average $\langle\bar{\dot{\omega}}|\widetilde{c}\rangle$ (━), conditional average restricted to unstretched reacting states $\langle\bar{\dot{\omega}}|\widetilde{c}, \widetilde{K} = 0\rangle$ (━), and the reaction rate for an unstretched 1D premixed laminar flamelet at the same equivalence ratio (━). Dashed lines indicate the conditional averages at fixed levels of tangential strain S_t.

Consistently with what observed by Berger et al. [138] for a jet flame at the same equivalence ratio, differential diffusion effects (left) result in reaction rate values higher than those found in an unstretched 1D laminar flame, which is due to the effect of stretch on local enrichment.
Since these states are significantly more abundant than states associated to mixture fraction leaning, the global conditional average, $\langle\bar{\dot{\omega}}|\widetilde{c}\rangle$, is also significantly larger than the one associated to unstretched samples only (red line), highlighting the significant effect of stretch on the reaction rate. Note that the latter curve still presents values larger than those for the unstretched laminar 1D flamelet (black curve), due to diffusion of mixture fraction from the enriched pockets in the nearby regions of non-zero stretch. Figure 6.7 (left) also indicates that increasing levels of tangential strain

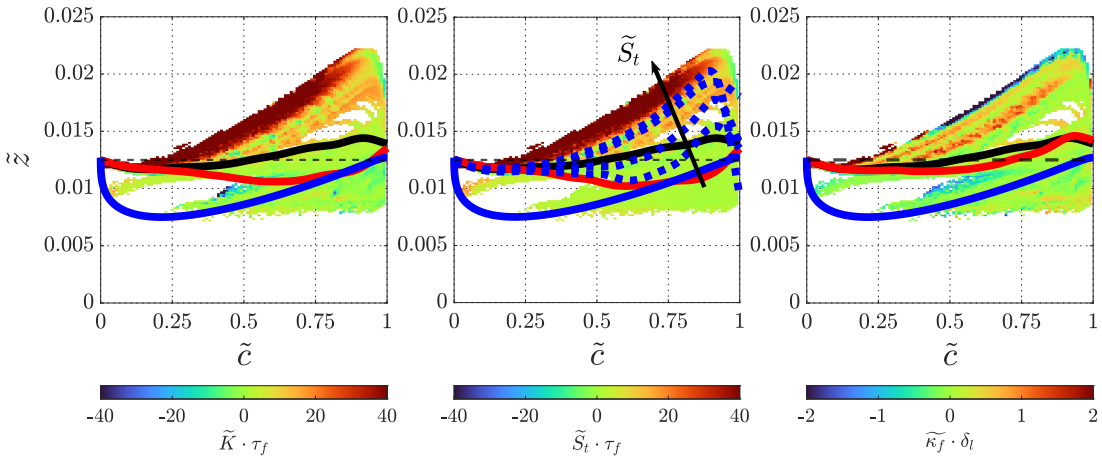

Figure 6.8: Scatter plots of mixture fraction versus progress variable in the flame region. Colours represent mean resolved normalized stretch (left), strain rate (center), and curvature (right). Global conditional averages $\langle\widetilde{z}|\widetilde{c}\rangle$ are marked as solid black line (━). The nominal mixture fraction is marked with a black dashed line (┈). The mixture fraction from 1D unstretched premixed flamelet at the same equivalence ratio is plotted with a solid blue line (━). Red lines (━) indicate conditional averages obtained considering points at zero stretch, strain and curvature, respectively. The dashed lines (┈) represent increasing levels of strain rate.

(dashed lines) yield an increase of conditional reaction rate, in agreement with the trends observed in [246]. These effects are completely absent when considering the case without differential diffusion (Figure 6.7, right), where the global conditional average matches the one obtained using unstretched samples only.

Also, as expected, increasing levels of resolved strain does not affect the conditional reaction rate. Figure 6.8 shows scatter plots of filtered mixture fraction $\widetilde{z}$ versus filtered progress variable $\widetilde{c}$, at a random timestep, colored by mean stretch, strain and curvature respectively. Global conditional averages as well as conditional averages obtained only using samples at zero stretch, strain or curvature are also shown. Stretch and tangential strain are normalized by the chemical time scale τ_f, and curvature is normalized by the laminar flame thickness δ_f, whose values correspond to those of a laminar one-dimensional premixed flame at the nominal inlet equivalence ratio. The plot on the left indicates a strong correlation between positive values of stretch and mixture enrichment. The global conditional average of mixture fraction versus progress variable shows the typical profile of a strained premixed 1D flamelet in counterflow configuration [246], as already observed in Fig. 6.6, with an initial decrease in mixture fraction with respect to the nominal value followed by a reincrease and eventual overshoot. The conditional average of unstretched reacting state, $\langle\widetilde{z}|\widetilde{c}, \widetilde{K} = 0\rangle$ (red line), is observed to align with the mixture fraction profile for

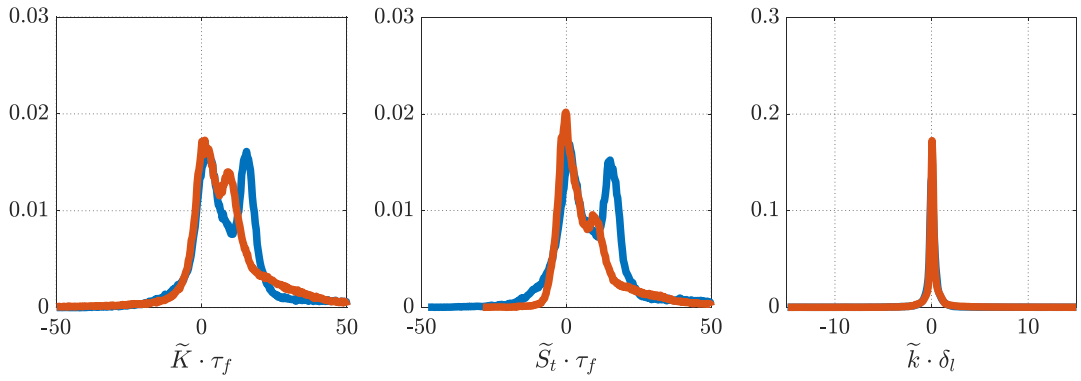

Figure 6.9: Probability density function of resolved stretch, strain and curvature, showing the comparison between the unity Lewis number case (—) and with differential diffusion (—).

an unstretched 1D premixed flamelet (blue line), confirming that stretch is driving this deviation. Consistently with Fig. 6.7 and the results in [**138**], the values on the "unstretched" conditional average curve are higher than those for the unstretched 1D flamelet. The two rightmost graphs in Fig. 6.8 further reveal that stretch effects are primarily driven by tangential strain in the present configuration, whereas curvature has a less pronounced influence. One can notice that the conditional average at zero curvature, $\langle \widetilde{z}|\widetilde{c}, \widetilde{\kappa}_f = 0\rangle$ (red line, rightmost graph), aligns with the global conditional average (black line), consistently with results in [**138**]. Furthermore, the conditional average at zero strain, $\langle \widetilde{z}|\widetilde{c}, \widetilde{S}_t = 0\rangle$ (red line in the central graph), appears to align with the unstretched conditional mean (red line in the left graph). This milder influence of curvature effects, as compared to previous studies, is due to the fact that the positive tangential strain itself at the flame anchoring location might be limiting the onset of thermodiffusive instabilities (observed instead in [**138**]), thus limiting the occurrences of strongly curved flame fronts [**246**, **248**]. As a final remark, Fig. 6.8 (central graph) further illustrates the conditional mean at zero curvature for increasing strain levels. This confirms the argument for Fig.6.7 that increasing strain intensifies the local enrichment, as observed in [**246**] for laminar strained flamelets, leading in turn to the increase of reaction rate.

To further characterize the influence of stretch, in Figure 6.9 the probability density functions of resolved stretch, tangetial strain and flame curvature, with and without differential diffusion, are shown. One can notice that curvature has a zero mode (although the mean remains slightly positive due to a mild skewness to the right), which is believed to be the result of only turbulent eddies motion. On the contrary, the PDF of strain indicates the presence of two peaks, which are believed in turn to correspond to the effect of turbulent eddies and to the applied strain in the shear

region where the flame anchors (positive mode). This distribution is thus different to that observed in [138] where only a peak around zero strain was observed. It is interesting to note that the presence of differential diffusion causes an increase in the value of tangential strain associated with this second peak (strain itself intensifies), as well as an increased number of occurrences at this value. This is linked to the stabilization of the flame closer to the bluff-body edge characterized by higher strain levels and an overall shortening of the flame, and indicates that the hydrogen flame 'chases' the high strain region.

6.4 Summary and Conclusions

Large-eddy simulations with a flamelet-based combustion model, recently developed to account for preferential diffusion effects, have been used to investigate the coupling between preferential diffusion and stretch in bluff-body stabilized lean premixed hydrogen flames subject to relatively high levels of flame tangential strain. The LES has been firstly validated against available experimental data of velocity and OH^*, showing that computational results are accurate. The preferential diffusion model was shown to be able to predict the local redistribution of mixture fraction in regions of non-zero strain and curvature. This redistribution was observed to cause the shift of the reaction source term peak towards the flame anchoring point, resulting in an increased flame-tangential strain and a shorter flame compared to the unity Lewis number case. Furthermore, the model captured the increase in reaction rate caused by positive strain by the sole use of unstretched flamelets thermochemistry. These findings demonstrate in the LES context that the considered differential diffusion model, based on an unstretched flamelets database, is effective in mimicking the peculiar physics of lean premixed hydrogen flames that exhibit coupling between stretch and differential diffusion, particularly in a configuration characterized by significant flame-tangential strain rate. This requires most of the strain and curvature to be resolved and the use of an appropriate correction for mixture fraction and progress variable. The insights provided within this work thus represent a step forward the definition of modeling strategies for highly-resolved LES simulations of lean premixed hydrogen flames.

7 Investigation of tangential strain rate impact on NO emissions

In Chapter 6, the effects of differential diffusion and their coupling with stretch were investigated. The results demonstrated the importance of including these effects in lean premixed hydrogen–air flames. In particular, strain was shown to induce a redistribution of the mixture fraction, leading to locally higher equivalence ratios and, consequently, to the formation of superadiabatic temperatures. These effects cannot be captured unless the flamelet model is properly modified to include corrections in the mixture fraction, progress variable, and enthalpy equations. Moreover, the model was shown to capture an increase in the progress-variable reaction rate at high strain levels near the bluff-body edge, reproducing the typical behavior of mixtures characterized by a negative Markstein length, such as ultra-lean hydrogen–air flames. Flamelet models are applicable when chemical time scales are much smaller than turbulent time scales, as discussed in Chapter 2. In this regime, turbulence can wrinkle and stretch the flame without affecting its inner structure, allowing it to be approximated as an infinitely thin surface composed of an ensemble of laminar flamelets. However, when slow chemistry must be accounted for, flamelet models may fail to provide reliable predictions since using the tabulated value at $c = 1$ would correspond to considering NO at chemical equilibrium, therefore leading to overprediction [135, 250]. NO formation is difficult to predict because it occurs on much slower time scales than the main combustion process. As a result, in premixed combustors, the residence time is often not sufficient for NO to reach its equilibrium value. Instead, its final concentration is governed by the local thermochemical history of the flow. In addition, NO formation is strongly dependent on temperature and mixture composition, making it highly sensitive to fluctuation induced by turbulence. Since NO concentrations are much lower than major species concentrations, even small inaccuracies in temperature or mixture composition can lead to large errors in their prediction. Several approaches have been proposed to address this limitation in flamelet models [135, 195, 250, 251]. Nevertheless, no modeling strategy

has yet been developed to consistently include strain effects in flamelet frameworks for slow-forming species such as NO.
To overcome these limitations and investigate NO emissions, a transported filtered density function (FDF) approach with Eulerian stochastic fields (described in Chapter 3) is employed, as it represents one of the most accurate combustion models for LES. The main objective of this chapter is to investigate NO emissions and their dependence on the flame tangential strain rate. Previous studies [246, 252, 253] have shown that increasing the tangential strain rate can lead to a reduction in NO emissions. Therefore, this work aims to assess whether such trends can also be observed in a practical premixed configuration. To this end, simulations are performed at three different inlet conditions, where the mass flow rates of the premixed fuel and oxidizer are increased to systematically vary the tangential strain rate and analyze its effect on flame dynamics and NO formation. It is worth noting that the amount of NO_2 is significantly smaller than that of NO, and the former can therefore be neglected in the present analysis [136]. Consequently, the trends discussed for NO can be considered representative of the overall NO_x formation.

7.1 Introduction

Hydrogen holds tremendous potential as an energy carrier and has emerged as a promising alternative to conventional fossil fuels [156]. In particular, the use of hydrogen in premixed combustion configurations offers the potential for high efficiency and low greenhouse gas emissions. However, the strong reactivity, low ignition energy, and high diffusivity of hydrogen pose significant challenges in controlling flame stability [24–26], making hydrogen more prone to flashback in premixed configurations [254]. Therefore, a fundamental understanding of the physics of hydrogen flames is essential for the design and optimization of future combustion technologies. Moreover, hydrogen combustion can cause high temperatures, leading to high levels of NO_x when air is the oxidizer. Although NO_x formation can be reduced by using lean premixed and partially-premixed combustion [255], the aforementioned challenges are further compounded at these conditions due to occurrence of intrinsic instabilities and their synergy with turbulence [138] typical of practical configurations. Large eddy simulation (LES) has emerged as a powerful tool for capturing the unsteady dynamics of turbulent reacting flows. LES resolves the large energy-carrying eddies of the turbulent flow field, while the effects of the smaller sub-grid scales (SGS) is modeled. However, the success of LES in reactive flow simulations heavily depends on the accurate representation of sub-grid scale turbulence–chemistry interactions (TCI), which are modeled [114] and remain one of the central challenges in the field. To address the challenge of modeling turbulence–chemistry interaction (TCI), a number of strategies have been developed [110, 121, 256]. Flamelet-based formulations, such as the Flamelet Progress Variable

(FPV) and Flamelet Generated Manifold (FGM) approaches, are widely adopted in LES of gas turbine combustors and laboratory flames owing to their computational efficiency [135]. However, for hydrogen flames, preferential diffusion effects become significant and must be incorporated by means of additional correction terms in the evolution equations of the controlling variables [202, 257–259]. Thickened Flame (TF) models constitute another commonly used LES strategy, in which the flame front is artificially thickened to allow resolution on the computational mesh, while a subgrid efficiency function accounts for unresolved wrinkling [180, 260, 261]. Yet, when applied to hydrogen combustion, TF models may introduce inaccuracies due to the enhanced sensitivity to stretch caused by thickening and their inability to represent thermodiffusive instabilities. Recent efforts to mitigate these limitations in hydrogen flames can be found in [217, 262, 263]. Among these models the transported filtered density function (T-FDF) method, presented in Chapter 3, is well known for its accuracy. In this study, the ESF approach within the context of LES has been employed to investigate the behavior of a premixed hydrogen–air flame stabilized by a bluff-body burner (NTNU burner), whose description is given in Chapter 4. The same test case was previously investigated in Chapters 5 and 6 using the flamelet approach with and without including differential diffusion effects. In this work, particular attention is devoted to analyze the coupling between differential diffusion and tangential strain rate and the effects that the latter plays on the local flame structure and NO formation. The tangential strain rate is changed by varying the inlet mass flow rate. As discussed in previous work [132, 133], hydrogen addition has been shown to delay the extinction tangential strain rate, proving that hydrogen is able to sustain very high tangential strain rate levels. A recent study [246] further demonstrated that NO_x emissions can be reduced by increasing the tangential strain rate on the flame front. The study employed a laminar counterflow configuration and it is the objective of this study to extend the work to a 3-D turbulent premixed hydrogen-air flame in a real scenario. Similar effects on the reduction in NO_x emissions linked to tangential strain rate effects were observed for a turbulent diffusion flame in [264]. The influence of stretch effects on NO_x emissions has been experimentally investigated by Drake et al. [265] showing that the net NO_x formation rates are affected by flame stretch due to changes in peak flame temperature, superequilibrium O atom concentrations, NO destruction reactions, and N_2O formation reactions. In this study, to complement and extend these findings, a practical premixed configuration is investigated and an extensive description of the relation with NO emission and tangential strain rate is provided. The objectives of the present study are: (i) to demonstrate the capabilities of ESF-based transported FDF models to predict the coupled strain-differential diffusion effects in lean premixed hydrogen-air flames; and (ii) to investigate the impact that an increase in flame-tangential strain rate has on NO emissions. The first objective is addressed by comparing the experimental measurements against the time-averaged results obtained by LES. The second objective is addressed by first demonstrating that tangential strain effects are

predominant over curvature. Subsequently, the level of tangential strain on the flame is increased by increasing the inlet mass flow rate and then correlated to NO emissions.

7.2 Case study and operating conditions

The test case considered here corresponds to the NTNU burner introduced in Chapter 4, under the same nominal operating conditions as the experimental setup. A detailed description of the configuration is provided in Chapters 5 and 6. In addition to the nominal case, two further operating conditions are examined numerically to assess the effect of tangential strain on NO formation by increasing the inlet mass flow rate by 60% and 100% relative to the nominal case. These configurations are referred to as *Case 1* (nominal), *Case 2* (60% increase), and *Case 3* (100% increase). The non-reactive case, referred to as *Case N-R*, was performed by imposing only air at the inlet boundary. A summary of the operating conditions and the mean tangential tangential strain levels (explained in the Sec. 7.4 section) for all three cases is provided in Table 7.1.

	$\dot{m}$ [g/s]	P_{th} [kW]	K_s [1/s]
Case 1	2.29	3.5	11300
Case 2	3.66	5.5	13500
Case 3	4.58	6.9	14000

Table 7.1: Operating conditions for the investigated case. Mass flow rates, respective theoretical power and mean tangential strain levels are shown for the three different configurations.

7.3 Numerical set-up

7.3.1 3-D case

The computational mesh characteristics and boundary conditions used in this work are the same employed in Chapter 6. The mesh refinement near the walls increases cell density in the flame front, as the flame develops close to the edge of the bluff body. Within the reaction zone, cell sizes range from a minimum of 35 μm to a maximum of 400 μm, with an average size of approximately 100 μm. The numerical results obtained for the velocity field by the LES have been compared with the experimental data at the same various axial locations used in Chapter 5 and Chapter 6. A mass flow rate boundary condition (implying a constant flat axial velocity profile) was imposed at the inlet, with values corresponding to the operating conditions described earlier (see Table 7.1). The Favre-filtered Navier–Stokes equations for conservation

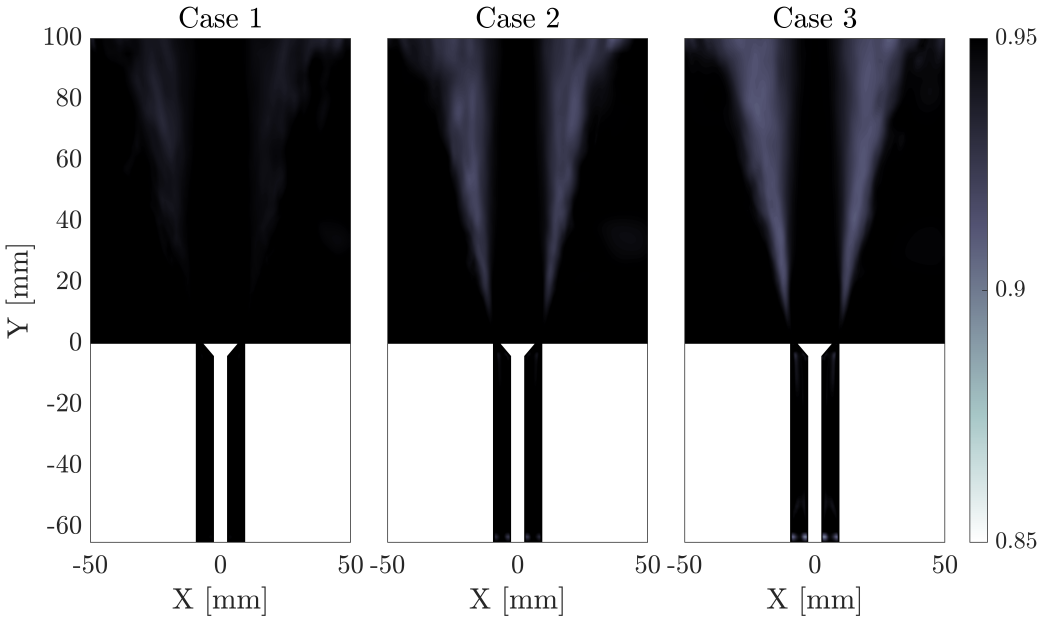

Figure 7.1: Contour plot of the Celik criterium for LES quality in the reactive flow simulation for the investigated test cases of Table 7.1.

of mass and momentum, are solved together with the transport equations of the Eulerian stochastic fields method (see Chapter 3), where Eq. (3.30) is used for species mass fractions and sensible enthalpy. The simulations were performed using the finite volume method in OpenFOAM v6. Second-order schemes were selected for both spatial and temporal discretisation. Time steps of 5×10^{-7} s, 3×10^{-7} s, and 2×10^{-7} s were used respectively for Case 1 to 3 to ensure that the CFL number remained below unity in all the domain. The chemical kinetics mechanism in [266] has been combined with the Capurso mechanism [267] to add the NO formation reactions as previously done by Acquaviva et al. [253]. The results were initially validated by comparing the available experimental data with LES results for the nominal mass flow rate (Case 1) using four and eight stochastic fields. To evaluate the ability of the simulations to capture flow characteristics, time-averaged and root-mean-square (RMS) values of the axial and radial velocity components were compared with experimental measurements. The model's capability to predict the flame structure was assessed by comparing the experimental OH^* chemiluminescence data obtained through Abel transformation with the filtered heat release rate. The suitability of the mesh for LES simulations was verified by ensuring that at least 80% of the turbulent kinetic energy was resolved. The resolved turbulent kinetic energy spectrum was calculated using the Cèlik criterion [227], where the quality of the mesh is assessed by comparing the ratio of the turbulent and effective viscosity.

Results from the reactive flow simulation are presented in Fig. 7.1, which show that more than 80% of the turbulent kinetic energy is resolved across the entire computational domain for all the three operating conditions. In the present study, Soret

effects are neglected to reduce the computational cost of the simulations. While Acquaviva et al. [253] demonstrated the importance of thermal diffusion effects for quantitatively predicting NO emissions in lean premixed and strained hydrogen-air flames, they also showed that the qualitative trends with varying strain rate remain unchanged when these effects are not considered. Thus, neglecting Soret effects is justified in the framework of this work, which investigates NO emission trends as a function of strain in a practical burner configuration.

7.3.2 1-D Counterflow setup

Results from the 3-D simulations are compared with those from 1-D counterflow simulations conducted at the same equivalence ratio and for different tangential strain levels in order to assess the capability of the LES approach to predict the expected trends as tangential strain increases. A similar approach was also followed in past studies [138, 268]. The same reaction mechanism used for the LES is employed in the 1-D simulations.
The counterflow setup consists of a reactants-to-products configuration, as illustrated in Fig. 7.2.

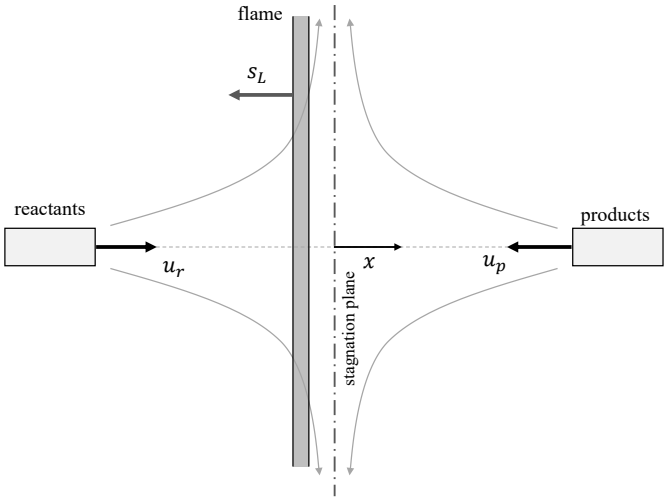

Figure 7.2: Schematic of the counterflow configuration employed for the 1-D simulations. u_r and u_p represent respectively the velocity of reactants and products, x and y are respectively the flamelet longitudinal and tangential coordinate, and S_L is the laminar flame speed.

The reactants mixture, with a nominal equivalence ratio of $\phi = 0.4$, is prescribed on the left-hand side. Following [246], complete combustion products and the unstretched adiabatic equilibrium flame temperature are prescribed on the right-hand side. The applied tangential strain rate in this configuration is defined as

$$K_s = \frac{|u_r| + |u_p|}{L}, \tag{7.1}$$

where $L = 2$ cm is the domain length, and u_r and u_p are the bulk velocities at the reactants and products boundary, respectively [269]. Three levels of nominal tangential strain rates are considered in this study, corresponding to the ones determined in the three turbulent simulations: K_s=11300 s^{-1}, K_s=13500 s^{-1}, and K_s=14000 s^{-1}. Given the applied tangential strain rate (Equation 7.1) and knowning that the same mass flow rate is imposed by CHEM1-D on the reactants and products side, the reactants u_r and products u_p inlet velocities can be found as:

$$u_r = \frac{K_s L}{1 + \frac{\rho_r}{\rho_p}}, \qquad u_p = u_r \frac{\rho_r}{\rho_p}, \tag{7.2}$$

where the density of the reactants ρ_r and products ρ_p have been introduced.

7.4 Results and Discussion

7.4.1 Validation

Figures 7.3 and 7.4 present comparisons between LES and experimental data of time-averaged and RMS axial and radial velocity components at various axial positions, for both non-reacting and reacting cases. The simulations show an overall good agreement with the experimental results for both velocity components and RMS of their fluctuations, except for some underestimation of the radial component at 5 and 10 mm. Additionally, a comparison between the axial component for the cold and reactive flow cases reveals an increase in the extent of the inner recirculation zone (IRZ) due to the expansion of the gases during the combustion process. Regarding velocity fluctuations, the LES successfully predicts the evolution of the RMS for both axial and radial velocities in the cold flow. However, in the reactive flow case, the RMS of the radial velocity in the shear layer is over-predicted, especially in the central region at a height of 20 mm. This over-prediction, found also in the results of Chapter 5 and Chapter 6 and by Liu et al [224], results from the interaction between flow dynamics and changes in density and composition due to chemical reactions. Discrepancies between the experimental data and the numerical simulation results can also be attributed to the limited resolution of the PIV measurements, as noted by Kay et al. [228]. Moreover, it can be observed that an increase in the number of stochastic fields has no effect on the velocity flow field as shown in the results obtained by LES for the reactive case. Nevertheless, these results indicate that overall the modeling framework investigated here is capable of predicting the time-averaged behavior of the flow behind the bluff-body with relatively good accuracy. Further comparisons with experimental data are shown next. Figure 7.5 compares the experimental time averaged OH^* chemiluminescence data with the time-averaged filtered heat release rate, both normalized with their maximum value. The figure shows that the LES model is able to capture both the length and the shape of the flame reported in the

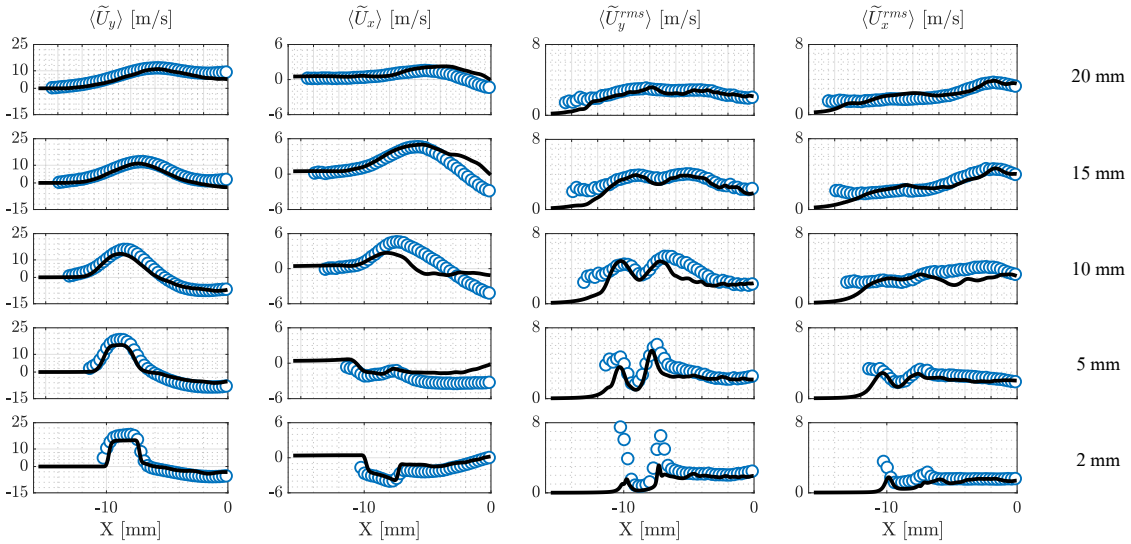

Figure 7.3: Radial profiles of time-averaged and RMS axial and radial velocity components at various axial locations from the bluff-body surface, for the non-reacting case (LES: ▬, Exp: ○).

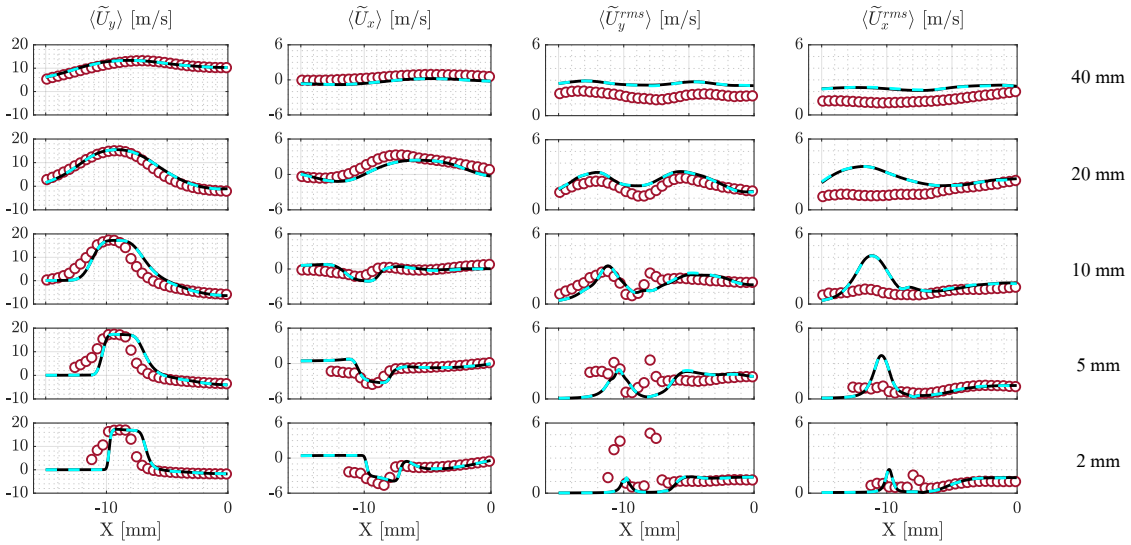

Figure 7.4: Radial profiles of time-averaged and RMS axial and radial velocity components at various axial locations from the bluff-body surface, for reacting Case 1 of Table 7.1 : ▬, LES 8 stochastic fields: ····, Exp: ○).

experimental measurements. An increase in the number of stochastic fields does not lead to significantly different results as observed earlier for the velocity flow field. Figure 7.6 further presents a comparison of the time-averaged filtered temperature fields obtained using four and eight stochastic fields. First, one can notice that again no significant difference in the LES predictions is obtained when increasing the number of stochastic fields to 8, thus, to limit computational effort, four stochastic fields are used in the remainder of this work. The results also highlight the presence of differential diffusion effects. For a hydrogen–air mixture at an equivalence

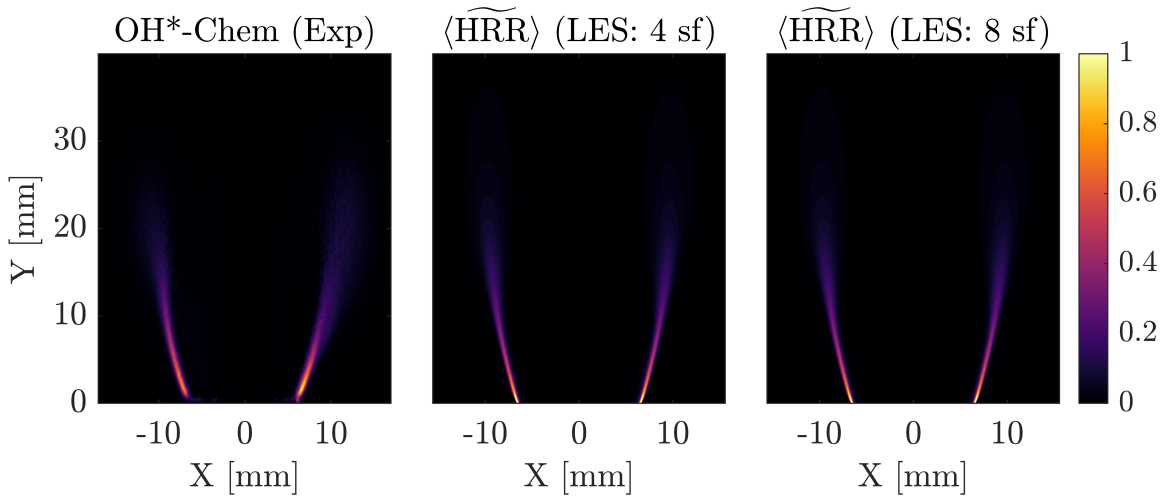

Figure 7.5: Time-averaged OH*-Chemiluminescence from experiments (left) and mid-plane contours of time-averaged filtered heat release rate (HRR) from LES results using four (mid) and eight (right) stochastic fields. All plots are normalized by their maximum values.

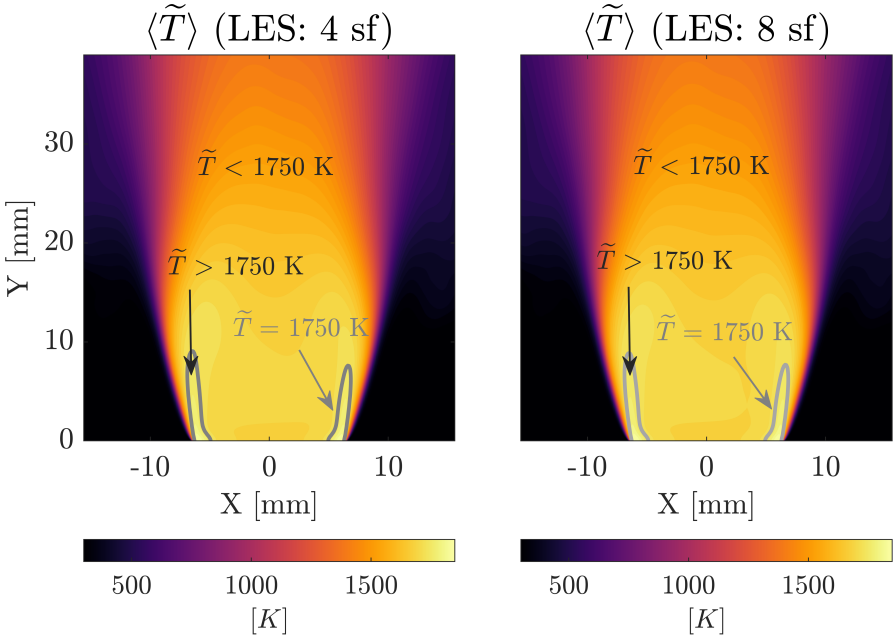

Figure 7.6: Time-averaged filtered temperature fields obtained from LES using four (left) and eight (right) stochastic fields. The grey contour corresponds to the 1750 K filtered-temperature isoline. Regions inside the isoline exhibit temperatures higher than 1750 K, whereas regions outside have lower temperatures.

ratio of $\phi = 0.4$, the adiabatic flame temperature is approximately 1450 K. However, when flame stretch becomes significant, the local mixture fraction distribution can vary throughout the domain, leading to regions along the flame front that are either richer or leaner than the nominal value [246]. This spatial variation alters the

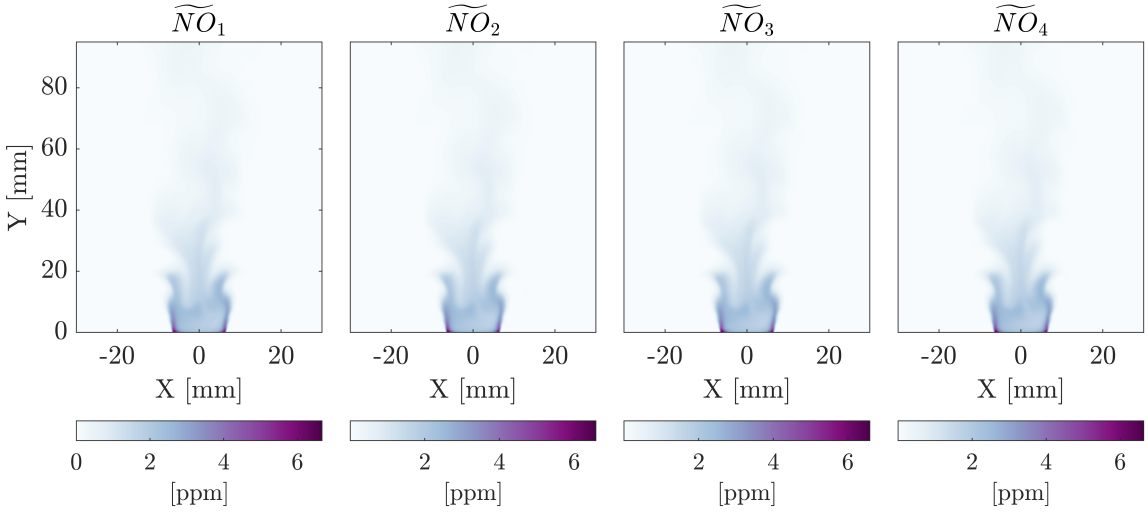

Figure 7.7: Instantaneous filtered NO mass fraction obtained from the solution of the stochastic field equation when four stochastic fields are used.

temperature distribution, with localized values exceeding the temperature value of a laminar freely propagating flame by more than 400 K at the flame anchoring region (bluff-body base), where stretch effects are expected to be strong due to the presence of the shear layer. Such behavior is thus captured in the present LES-ESF formulation and the coupling between differential diffusion and tangential strain will be further investigated in the next sections.

Some considerations can be made regarding the micromixing and Wiener terms in Eq. 3.30, by quantifying the variability among the stochastic fields themselves. Specifically, the standard deviation of the stochastic fields for NO was evaluated. This choice is motivated by the fact that the micromixing term directly depends on the deviation of each stochastic field from their mean, as shown in the last term of the RHS of Eq. 3.30. Hence, the standard deviation provides a clear indication of the relative strength of micromixing and turbulent fluctuations, since the difference among each stochastic field is driven by these two terms. Contour plots of the four instantaneous stochastic fields for NO are reported in Fig. 7.7.

To quantify the deviation of the different stochastic fields from the final (ensemble-averaged) solution, standard deviation is computed as $\sigma = \sqrt{1/N_s(\zeta_i - \bar{\zeta})^2}$, where ζ_i is the solution of the i-th stochastic field and $\bar{\zeta}$ is the mean of all fields. In addition, a percentage deviation is computed to assess the local difference of each stochastic field from the ensemble-averaged solution. The instantaneous standard deviation $\sigma_{\widetilde{\mathrm{NO}}}$ and the percentage deviation ε are presented in the first and second contour plots of Fig. 7.8, respectively.

The results show that the percentage deviation is of the order of 1–2 % at the edge of the bluff body (within the flame region), with local peaks reaching approximately 13% further downstream. This behavior can be attributed to the dependence of both

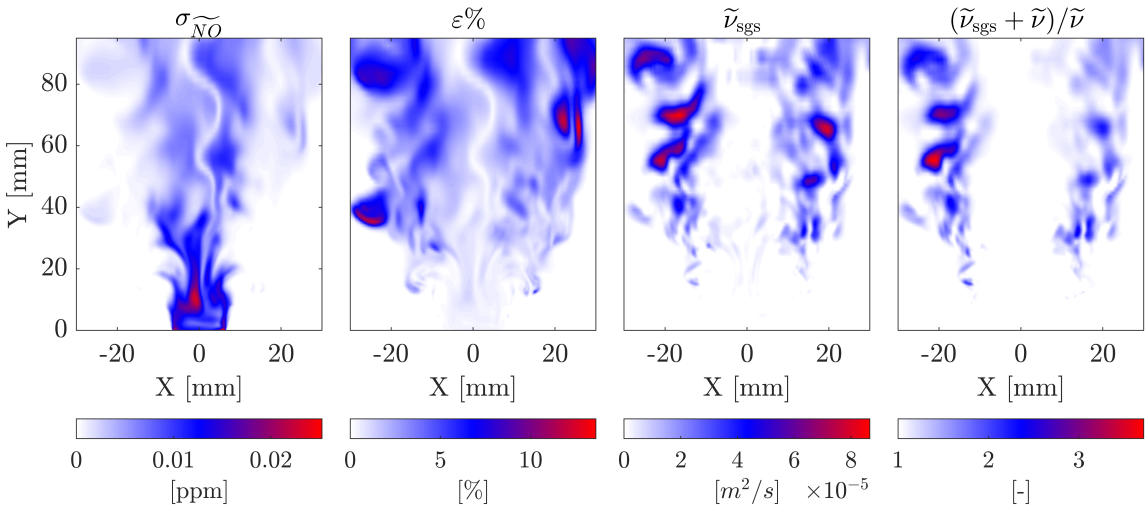

Figure 7.8: From left to right: instantaneous standard deviation of the four NO stochastic fields; percentage deviation; turbulent viscosity; ratio of effective to molecular viscosity.

the micromixing and stochastic terms on the sub-grid viscosity (and on the cell size for the micromixing term). Since the sub-grid viscosity is very low in the flame region and increases downstream as turbulence develops, the stochastic fields tend to deviate more in the downstream region. This interpretation is supported by the fourth contour plot from the left in Fig. 7.8, which shows the ratio between the effective viscosity and the molecular viscosity. Several considerations can be made regarding the deviation among the stochastic fields. (i) Upstream of the bluff body, both the micromixing term and the subgrid-scale fluctuations are essentially zero. This is because the reactant fluxes do not exhibit significant gradients, and no turbulent perturbations are imposed at the inlet; any synthetic turbulence introduced by a turbulence generator would be negligible compared to the one produced by the bluff body. (ii) In the flame region (at the edge of the bluff body), the fluctuations increase. The combustion process generates strong gradients in the scalar fields (in this case, NO), which amplify the contribution of the Wiener term, as this scales with the scalar field gradients. Although the micromixing term would also be expected to act here, since it depends on the deviation of each stochastic field from the ensemble mean, its influence remains limited because both the sub-grid viscosity and the cell size are very small. As a result, the Wiener term dominates in this region. (iii) Further downstream, the scalar-field gradients decrease, while the sub-grid viscosity increases due to both the coarser mesh and the higher turbulence levels. In this region, the Wiener term becomes less significant because of the reduced gradients, allowing micromixing effects to emerge more clearly.

It is worth noting that, in the absence of experimental or DNS data for the increased-strain cases, the observation of similar strain-dependent trends in the conditional mean of the mixture fraction and the hydrogen-based progress variable indicates

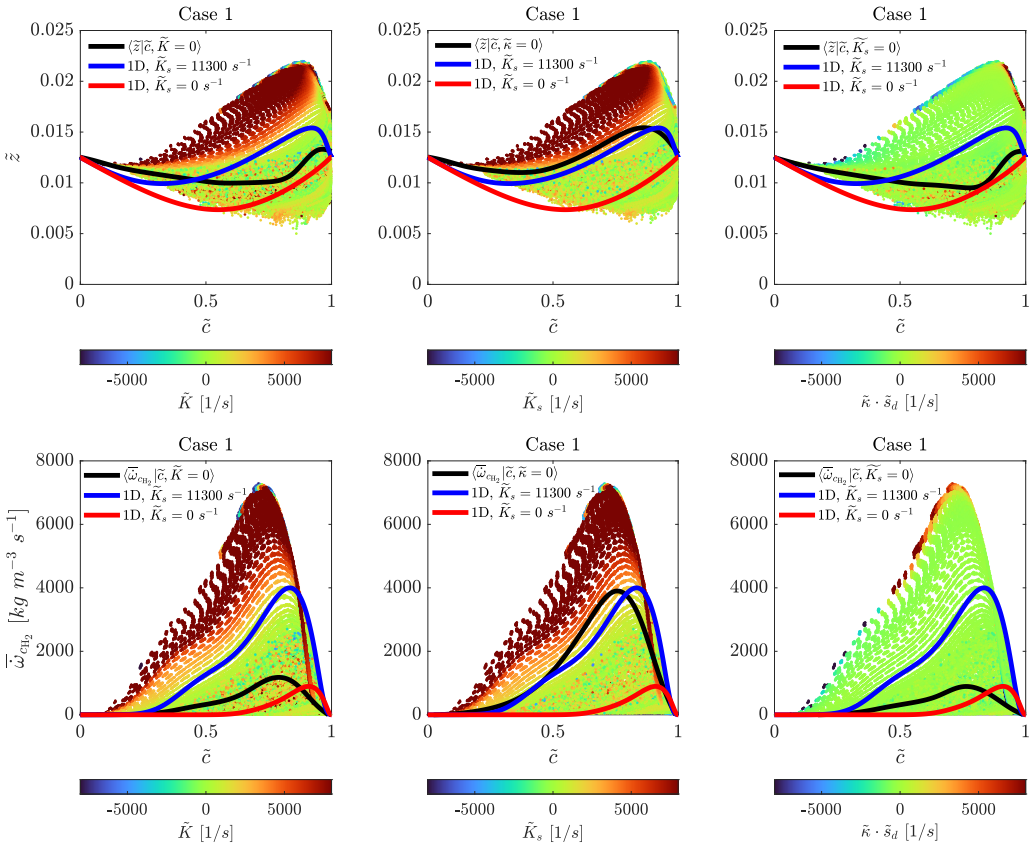

Figure 7.9: Scatter plots of mixture fraction (top) and progress variable reaction rate (bottom) versus progress variable in the flame region. Colours represent filtered stretch (left), tangential strain rate (center), and curvature (right). Solid black lines (▬) represent, left to right, the conditional average ($\langle\widetilde{z}|\widetilde{c}\rangle$ or $\langle\overline{\dot{\omega}}_{c_{H_2}}|\widetilde{c}\rangle$) respectively at $\widetilde{K}=0$, $\widetilde{\kappa}=0$ and $\widetilde{K}_s=0$. The progress variable reaction rate from 1-D unstretched premixed flamelet and 1-D counterflow flamelet at the same equivalence ratio are plotted respectively with a solid red line (▬) and a solid blue line (▬).

that the LES model used here captures the dominant effects of increasing tangential strain rate as expected from laminar and turbulent DNS studies [246, 252]. Yet, the accuracy of LES-ESF in providing a quantitative estimate of species concentrations and NO formation in highly strained turbulent flames should be further assessed in the future as additional data become available.

7.4.2 Reacting states

The effect of tangential strain rate on the flow and thermochemical variables is investigated in this section. Stretch, tangential strain, and curvature can be calculated as

$$\widetilde{K} = \widetilde{K_s} + \tilde{s}_d \cdot \widetilde{\kappa} \tag{7.3}$$

$$\widetilde{K_s} = \nabla \cdot \widetilde{u} - \hat{n} \cdot \nabla \widetilde{u} \cdot \hat{n} \tag{7.4}$$

$$\widetilde{\kappa} = \nabla \cdot \hat{n} \tag{7.5}$$

where K is the total stretch, K_s is the tangential strain, $\tilde{s}_d$ represents the displacement speed and κ is the curvature. The vector $\hat{n} = -\nabla\widetilde{c}_{\mathrm{H_2}}/|\nabla\widetilde{c}_{\mathrm{H_2}}|$ is the flame-normal vector pointing toward the unburned gas. The displacement speed $\tilde{s}_d$ is calculated as:

$$\tilde{s}_d = \frac{1}{|\nabla\widetilde{c}_{\mathrm{H_2}}|}\left(\frac{\partial\widetilde{c}_{\mathrm{H_2}}}{\partial t} + \widetilde{u}\cdot\nabla\widetilde{c}_{\mathrm{H_2}}\right) \tag{7.6}$$

Following the analysis in [138], scatter plots of mixture fraction $\tilde{z}$ and hydrogen-based progress variable reaction rate $\overline{\dot{\omega}}_{c_{\mathrm{H_2}}}$ are plotted versus progress variable $\widetilde{c}$ in Fig. 7.9. These plots are constructed using four random time-steps and are respectively colored by local values of filtered stretch, tangential strain and curvature. The hydrogen-based progress variable and its source term are defined respectively as $\widetilde{c} = 1 - \widetilde{Y}_{\mathrm{H_2}}/\widetilde{Y}^u_{\mathrm{H_2}}$ and $\overline{\dot{\omega}}_{c_{\mathrm{H_2}}} = -\overline{\dot{\omega}}_{\mathrm{H_2}}/\widetilde{Y}^u_{\mathrm{H_2}}$, where $\widetilde{Y}_{\mathrm{H_2}}$ represents the filtered hydrogen mass fraction, and the superscript u denotes the unburnt state. To focus on reactive regions, only data points for which $\overline{\dot{\omega}}_{\mathrm{H_2O}} > 1$ are included. By comparing the plots colored by curvature (right of the figure), for both mixture fraction and progress variable reaction rate, with those colored by total stretch and strain (respectively left and middle plots in the figure), it becomes evident that the contribution to total stretch of curvature multiplied by $\tilde{s}_d$ is negligible, as also found in Chapter 6. A similar observation can be made by comparing the conditional mean of mixture fraction at zero stretch (black solid line in the leftmost plot) to the one at zero tangential strain (black solid line in the rightmost plot). If curvature effects were significant, one would have expected to observe a local enrichment in the conditional mean at zero tangential strain (black solid line in the rightmost plot) due to curvature effects. However, this is not the case, and an enrichment is instead observed for the conditional mean at zero curvature (black solid line in the central plot), which considers only tangential strain effects. The conditional mean in this case also shows a good agreement with the 1-D counterflow strained flamelet at the same mean tangential tangential strain rate evaluated by means of the PDF of tangential strain (see discussion in the next section).

A similar consideration applies to the scatter plots of the source term of the progress variable, which reveal that both the conditional mean at zero stretch and zero tangential strain rate align with the 1-D unstretched flamelet at the given equivalence ratio. In contrast to the findings of Berger *et al.* [138], this test case is primarily dominated by tangential strain, and the effects of curvature can thus be neglected. This is an important consideration, as the reduction in NO_x emissions has previously been associated with an increase in tangential strain rate [246]. In the next subsection, the effect of flame tangential strain rate will be investigated by increasing its level on the

flame through a change in the inlet velocity.

7.4.3 Tangential strain effects on the flame structure

As described in Section 7.2, the mass flow rate at the inlet is increased by 60% and 100% of the nominal value (respectively Case 2 and Case 3 of Table 7.1) to produce corresponding increases in the level of tangential strain on the flame. In order to meaningfully compare conditional means from the LES to results obtained from one-dimensional strained flamelets, it is necessary to quantify the level of tangential strain rate on the flame in the turbulent cases. This was accomplished by using data at random time-steps and considering only reacting samples, with the condition $\overline{\dot{\omega}}_{H_2O} > 1$. Figure 7.10 presents the probability density function (PDF) of the tangential strain rate obtained for the three cases. Mean values are also indicated in the figures by the vertical dashed lines.

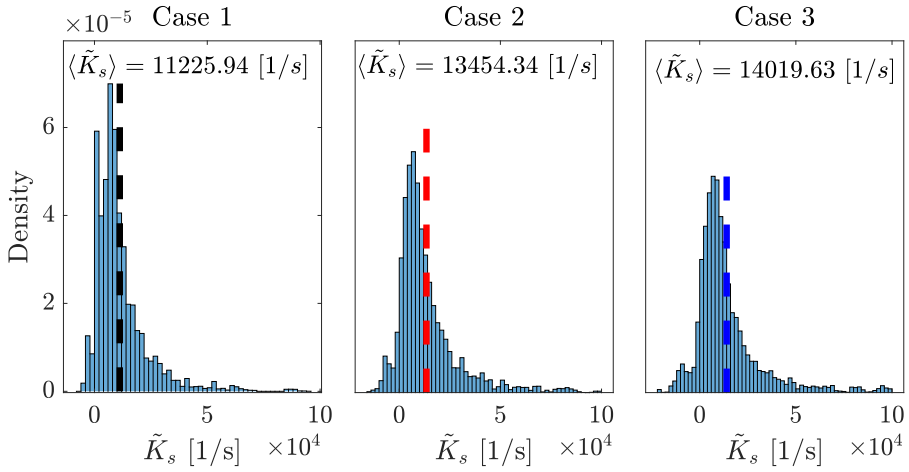

Figure 7.10: Probability density function of tangential strain rate. Only reactive samples at $\overline{\dot{\omega}}_{H_2O} > 1$ are considered. The dashed line represents, from left to right, the mean value of the PDFs respectively for Case 1 (····), Case 2 (····) and Case 3 (····) of Table 7.1.

As illustrated in the figure, the mean tangential strain rate increases with the mass flow rate at the inlet. The estimated values of the latter are reported in Table 7.1 together with the boundary conditions.
It should be noted that comparing the tangential strain levels to those obtained from a laminar computation is not straightforward. In the turbulent case, the presence of transient eddies that appear and vanish rapidly can significantly elevate the strain levels, often resulting in higher values than in the laminar scenario. Moreover, in laminar simulations, the strain rate is defined as the derivative of velocity with respect to the tangential coordinate. In contrast, in the 3-D turbulent case, the tangential strain on the flame is evaluated using Eq. 7.4. This mismatch between the two definitions makes it difficult to directly compare the quantities obtained from the 1-D and 3-D simulations. Consequently, estimating the mean tangential strain

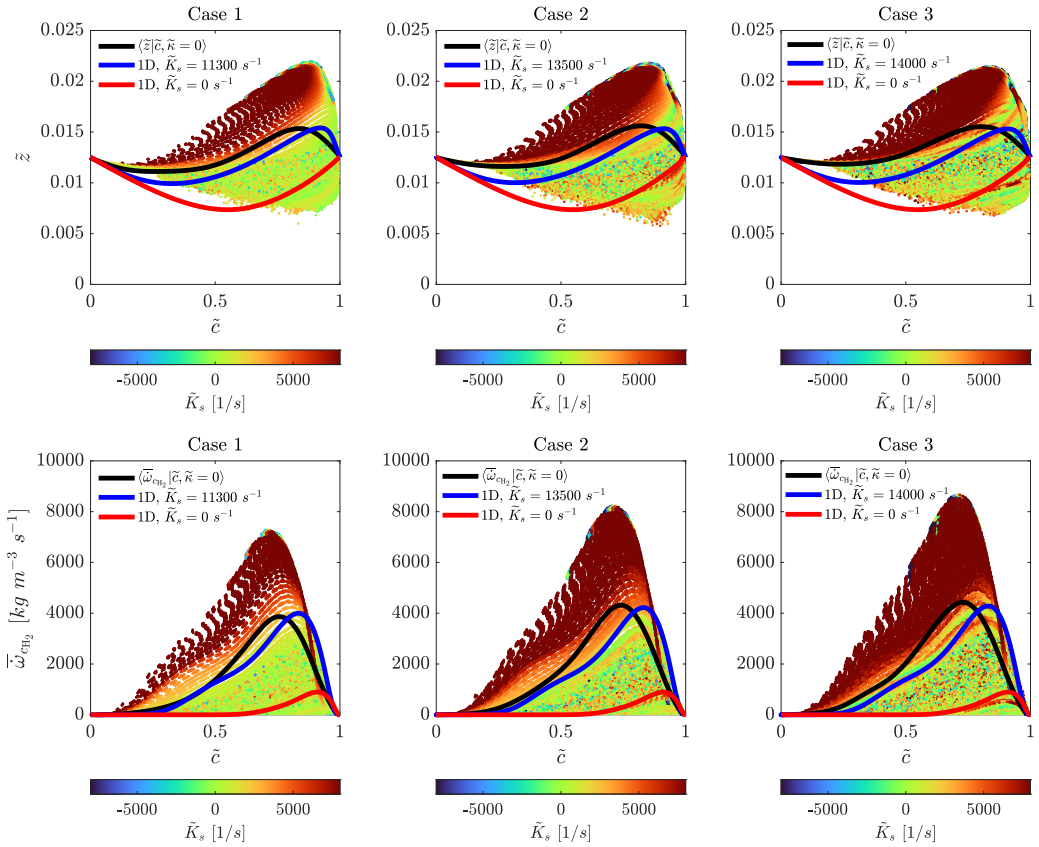

Figure 7.11: Scatter plots of mixture fraction (top) and progress variable reaction rate (bottom) versus progress variable in the flame region for the three reacting cases of Table 7.1. Samples are colored by filtered tangential strain rate. Solid black lines (—) represent the conditional average ($\langle\widetilde{z}|\widetilde{c}\rangle$ or $\langle\overline{\dot{\omega}}_{c_{H_2}}|\widetilde{c}\rangle$) of samples at $\widetilde{\kappa}=0$. The progress variable reaction rate and the Bilger's mixture fraction obtained form the 1-D counterflow and freely propagating (unstretched) simulations at the same equivalence ratio are respectively plotted with solid blue line (—) and solid red line (—).

levels using the probability density function (PDF) provides only an approximation rather than an exact measure. This analysis is therefore performed to estimate a mean level of flame-tangential strain rate in the turbulent cases, and thus have a meaningful comparison with the trends observed in laminar 1D strained flames for the same effective strain. Scatter plots of mixture fraction and progress variable reaction rate versus progress variable are shown in Fig. 7.11 for the three reacting cases of Table 7.1, in order to highlight the influence of tangential strain on the flame. As previously discussed, the effects of curvature are assumed to be negligible. The samples in Fig. 7.11 are colored according to the tangential strain rate, and the conditional means are calculated assuming zero curvature, thus considering only the effects of tangential strain. The conditional means for each case are compared to the results from the 1-D counterflow strained flamelets at the same mean tangential strain rate, estimated using the PDF (see Table 7.1). By examining the colour of the samples in both the plots of filtered mixture fraction and progress variable reaction rate, it is evi-

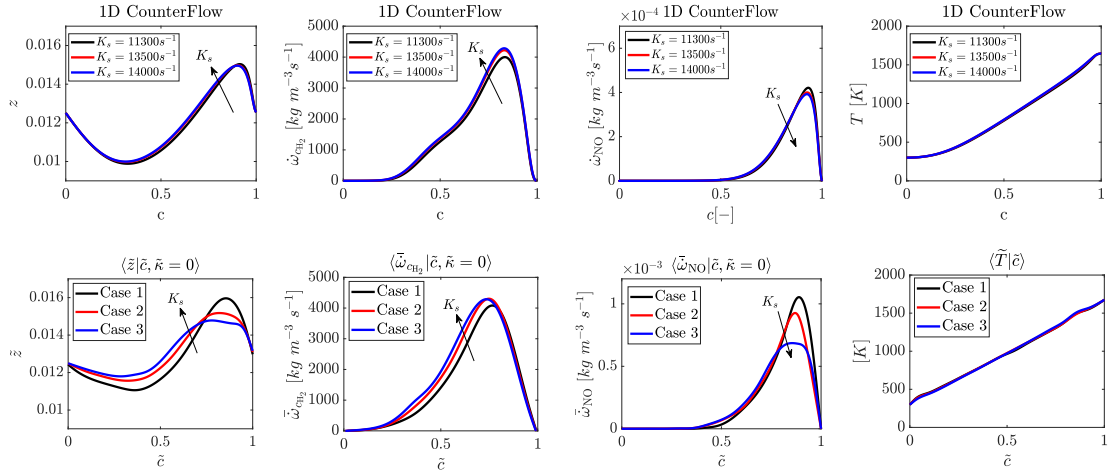

Figure 7.12: (Top) conditional means of mixture fraction (first column), reaction rate of hydrogen-based progress variable (second column), reaction rate of NO (third column) and temperature (last column) for the three reactive cases of Table 7.1 are compared to the same quantities obtained from 1-D counterflow simulations (bottom) at same conditions of equivalence ratio and mean tangential strain. The arrows indicate the direction of increasing tangential strain rate.

dent how the tangential strain levels increase from Case 1 to Case 3. Furthermore, the conditional means for both quantities closely mimic the shape of the laminar counterflow case. Some discrepancies are noticeable in the lean region, where this behavior is more pronounced in laminar flames compared to the turbulent case. This discrepancy may be attributed to 3-D effects, which are not captured in the 1-D laminar flames. Additionally, the shift in the progress variable reaction rate peak toward lower progress variable values is characteristic of a turbulent flame, and is accurately captured by the combustion model. The top and middle graphs in Fig. 7.12 present a comparison between the conditional means of mixture fraction $\tilde{z}$ and progress variable reaction rate $\overline{\dot{\omega}}_{c_{H_2}}$, respectively, obtained from the LES simulations for the three reactive cases reported in Table 7.1 and the laminar counterflow flames at the same mean tangential strain levels. The conditional means follow the same trends as in the 1-D case when the mean tangential strain rate increases. The most notable observation from this figure is that the peak of the reaction rate for the progress variable (middle graphs in Fig. 7.12) increases with tangential strain, resulting in a more reactive flame. This behavior is typical for mixtures with a negative Markstein length $\mathcal{L}$. Moreover, the influence of tangential strain rate manifests clearly in the behavior of the mixture fraction profiles (top graphs in Fig. 7.12). As the tangential strain rate increases, these profiles become noticeably flatter underscoring the role of tangential strain in limiting thermodiffusive instabilities [**246**, **268**]. This effect may also arise because, in the present test case, the increase in tangential strain rate was achieved by increasing the inlet mass flow rate. As a result, however, turbulence intensity also increases (due to the shear gradients), causing turbulent diffusion to dominate over

molecular diffusion, thereby limiting the impact of differential diffusion [270].

7.4.4 Tangential strain effects on NO emissions

As discussed in the previous section, higher tangential strain levels lead to an increased reaction rate of the hydrogen-based progress variable. A similar behavior is expected for the NO reaction rate, as reported by [246]. The latter study showed that although the NO reaction rate increases with tangential strain, a redistribution of OH radicals leads to a decrease in NO emissions as tangential strain increases. In the present work, however, a decrease in the peak NO reaction rate is observed, as shown in the third column graphs in Fig. 7.12. This is attributed to a reversal in Markstein length behavior at sufficiently high tangential strain levels, where the consumption speed begins to decline with increasing tangential strain. Figure 7.13 illustrates this behavior of the consumption speed, calculated as $S_c = -1/(Y^u_{H_2}\rho^u)\int_{-\infty}^{+\infty}\dot{\omega}_{H_2}dx$, for a 1-D counterflow flame at the same equivalence ratio as the turbulent test case and for increasing strain values. As mentioned earlier, the consumption speed increases with stretch and thus with tangential strain. However, after reaching a level of tangential strain around 12000 s^{-1}, the consumption speed starts to decrease, following the typical behavior of a positive Markstein length.

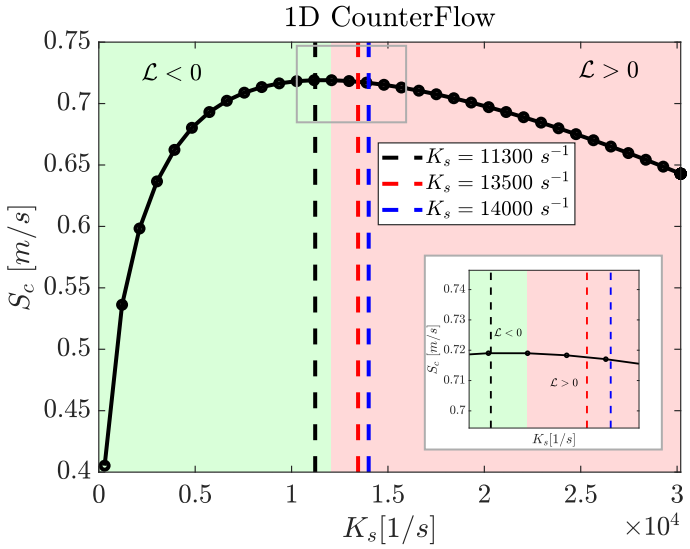

Figure 7.13: Consumption speed as function of tangential strain rate in 1-D counterflow simulations at $\phi = 0.4$. The consumption speed increases with tangential strain up to a value of 12000 s^{-1}. After this value the consumption speed starts to decrease as tangential strain is increased. This transition is highlighted by the inversion of the Markstein length $\mathcal{L}$ which shows the typical behavior of negative Markestein length mixtures for tangential strain lower than 12000 s^{-1} and the opposite for tangential strain levels higher than the latter.

This occurs as, despite the peak of $\dot{\omega}_{H_2}$ increases, its integral along the domain de-

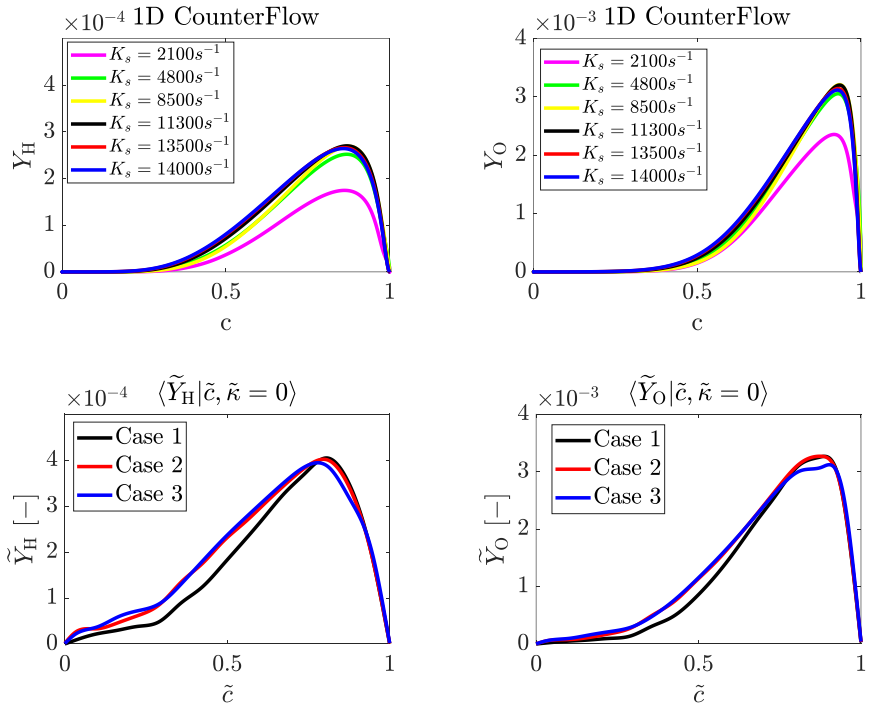

Figure 7.14: (Bottom) conditional means of H (left) and O (right) mass fraction for the three reactive cases of Table 7.1 are compared to the same quantities obtained from 1-D counterflow simulations (top) at same conditions of equivalence ratio and mean tangential strain.

creases due to the flame thickness becoming thinner, and to the fact that strain starts to weaken the flame [271]. By looking at the reaction rate of NO in Fig. 7.12, one can notice that NO formation decreases at sufficiently high tangential strain levels, which is observed for both laminar and turbulent regimes. This occurs because the mean tangential strain rate levels in Case 2 and Case 3 are large enough to induce a shift of the Markstein length from negative to positive.

NO production is also generally influenced by temperature. The plots in the last row of Fig. 7.12 show the conditional mean of temperature in the progress-variable space (left), together with the corresponding profiles from the laminar counterflow flames (right). As the tangential strain rate increases from Case 1 to Case 3, the conditional mean of temperature does not change significantly, consistent with what is observed in the laminar flames. This indicates that the reduction in NO is not driven by temperature variations. Porcarelli et al. [246] showed that, in their configuration, the reduction in NO was linked to the redistribution of OH radicals, which affects NO formation through the thermal route. However, as seen in Fig. 7.6, the temperatures attained in the present case are too low for the thermal-NO mechanism to dominate. At these temperature levels, the NNH pathway remains the primary route of NO formation, consistent with the findings of Acquaviva et al. [253]. Their study

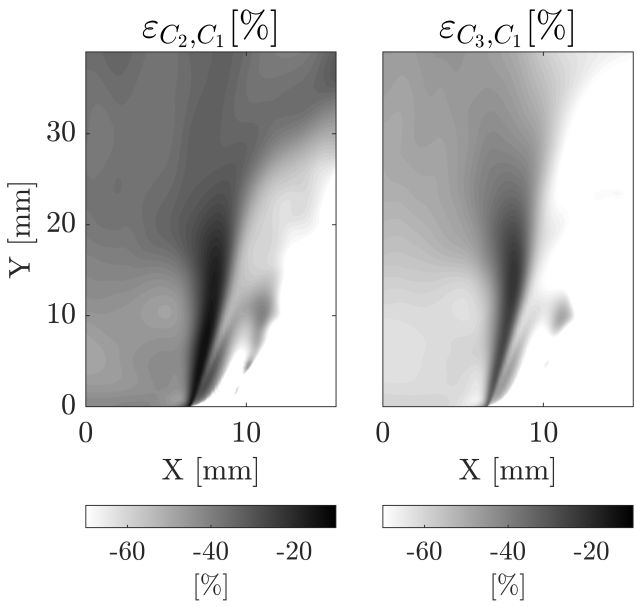

Figure 7.15: Relative difference ε in NO mass fraction for Case 2 (left) and Case 3 (right) with respect to Case 1. C_1, C_2 and C_3 in the title of the figure refer to Case 1, Case 2 and Case 3.

showed that, in laminar counterflow flames, NO peaks increase with strain due to a redistribution of H and O radicals. This behavior holds in the regime of negative Markstein length. However, when the strain becomes sufficiently high to invert the Markstein length from negative to positive, the redistribution of H and O changes. This behavior is illustrated in Fig. 7.14. In laminar counterflow flames, the peaks of both H and O initially increase with strain ($K_s < 11300\ \mathrm{s}^{-1}$), enhancing NO formation through the NNH pathway. Once the strain levels approach the values found in Case 1, Case 2 and Case 3 ($K_s > 11300\ \mathrm{s}^{-1}$), the peaks start to decrease in the reaction zone region ($0.8 < c < 1$). A similar trend is observed in the turbulent cases: although H and O increase with strain in the pre-heating region, their peaks decrease in the reaction zone. This reduction directly contributes to the lower NO production via the NNH pathway, in agreement with the behavior observed in laminar counterflow flames. Figure 7.15 shows the local relative difference in NO mass fraction calculated as $\varepsilon_{C_i,C_1} = (\langle\widetilde{NO}_{C_i}\rangle - \langle\widetilde{NO}_{C_1}\rangle)/\langle\widetilde{NO}_{C1}\rangle \cdot 100\rangle$ for both Case 2 and Case 3 with respect to Case 1, where C_1 and C_i refer respectively to Case 1 and Case 2 or 3. It can be noted how increasing the tangential strain rate leads to a reduction in NO production both in Case 2 and Case 3. One might object that this decrease could be also attributed to a lower flow residence time because of the increased mass flow rate from Case 1 to Case 2 and 3. However, the NO formation pathway which is strongly affected by the residence time is the thermal one, which is not the dominant pathway in the investigated case, as discussed above. Rather, the dominant NO formation route here is the NNH one, which is not affected by the flow residence time as NO is mostly formed

within the flame. This can be seen from the contour plot in Fig. 7.16 below, which shows that the source term of NO in the products region is very close to zero, with most production happening in the flame region. In light of these arguments, the residence time is expected to have a very limited influence on the overall NO trend between the three cases investigated, and thus the observed NO formation can be attributed solely to increased strain.

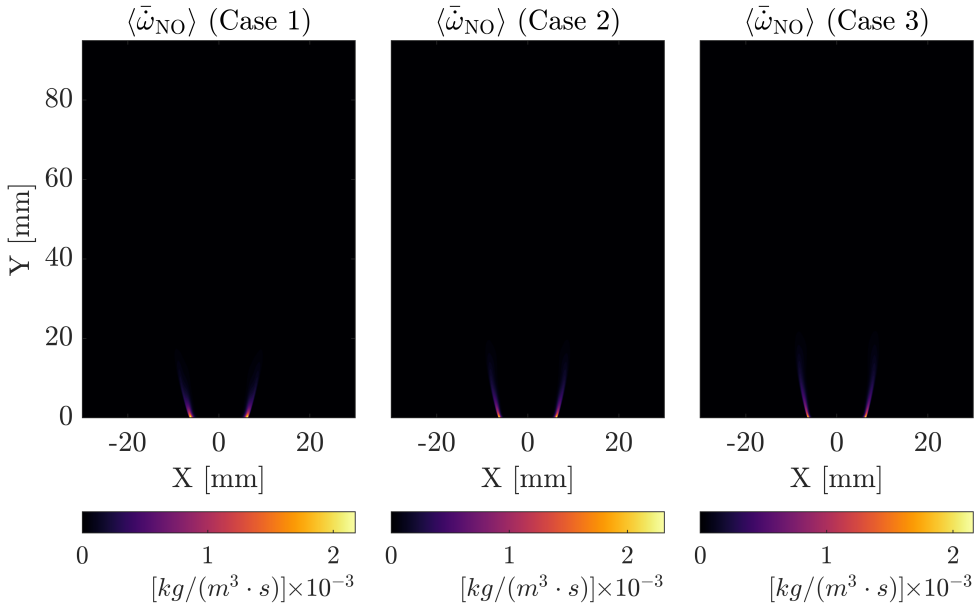

Figure 7.16: Contour plot of NO source term for Case 1 (left), Case 2 (middle) and Case 3 (right)

The time-averaged mass flow rate of NO, computed as $\overline{\dot{m}}_{NO} = \int_A (Y_{NO}\, \rho\, U_y)\, dA$, has been further evaluated at the outlet of the LES domain to get a global picture of the NO emissions for the different strain cases.
Given that the mass flow rate of the reactant mixture at the inlet has been increased from Case 1 to Case 3 of Table 7.1, the thermal power of the burner $P = \dot{m}_{H_2} LHV$ also increases, where $LHV = 120$ MJ/kg denotes the lower heating value of the fuel. To enable a fair comparison across different operating conditions, the NO mass flow rate is normalized by the burner power, yielding an emission intensity expressed as NO mass flow rate per unit power (in kg/s^{-1}/kW). A similar normalization approach is used in [**267**], where an emission index *EI* is defined by dividing the NO mass flow rate by the fuel mass flow rate. This is effectively equivalent to the procedure adopted here, since the fuel mass flow rate is multiplied by the LHV, which remains constant across the three cases while the fuel mass flow rate varies from Case 1 to Case 3. Note that other types of normalization can also be employed; for instance, one may normalize by the effective power $P_{eff} = -LHV \int_V \bar{\omega}_{H2} dV$. When using this alternative normalization (results not shown), the same trends are observed, and the reduction in NO with increasing tangential strain rate remains unchanged. Figure 7.17 presents

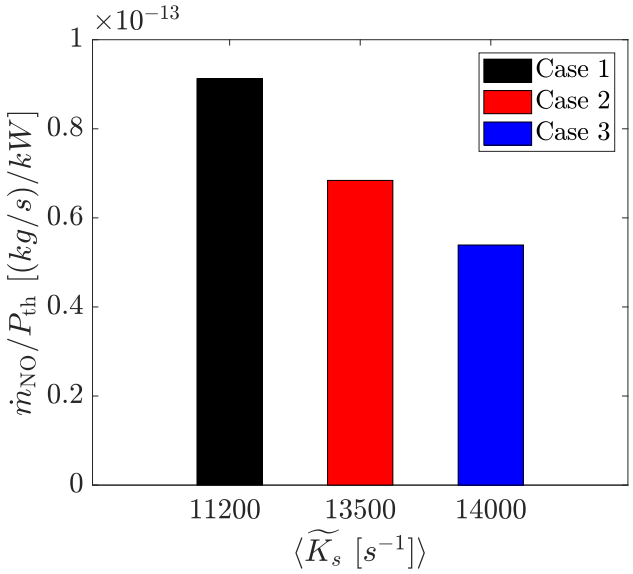

Figure 7.17: NO mass flow rate at the outlet divided by the thermal power. The three levels of mean tangential strain rate evaluated using the PDFs are reported on the x direction, showing a decrease in the NO production per kW as the tangential strain rate is increased.

the normalized mass flow rate of NO for each configuration (refer to Table 7.1) as a function of the mean tangential strain rate. The bar plot illustrates that operating under higher tangential strain conditions leads to a reduction in NO emissions per kilowatt of thermal power. Table 7.2 reports the percentage reduction in the NO mass flow rate per kW as a function of the percentage increase in the mean tangential strain rate. For increases in the tangential strain rate of 19.5% and 23.9% in Case 2 and Case 3, respectively, compared to Case 1, the mass flow rate per unit kilowatt decreases by 26.4% and 42.6%, respectively, resulting in almost half the NO emissions per kW for Case 3.

	$\Delta\dot{m}$ %	$\Delta\langle\widetilde{K}_s\rangle$ %	$\Delta(\dot{m}_{NO}/P)$ %
Case 2	+60	+19.5	-26.4
Case 3	+100	+23.9	-42.6

Table 7.2: From left to right: mass flow rates, the corresponding increase in mean tangential strain, and the reduction of NO mass flow rate normalized by the burner power for the three configurations.

7.5 Summary and Conclusions

Large eddy simulations of a premixed hydrogen-air flame stabilized by a bluff-body burner were performed to investigate the effects of the coupling between tangential strain and differential diffusion in a premixed burner, and its effect on NO emissions. The simulations employed the Eulerian Stochastic Fields method to account

for turbulence-chemistry interactions, with particular emphasis on the role of tangential strain rate in determining flame structure and NO formation characteristics. Three different mass flow rates were examined to systematically vary the tangential strain intensity while maintaining a constant equivalence ratio. The ESF approach, accounting for differential diffusion effects via a non-unity constant Lewis numbers approach, effectively captures the impact of tangential strain evidenced by the redistribution of the mixture fraction and the associated increase in reaction rates. Moreover, the analysis revealed that tangential strain rate is the main component of flame stretch for the investigated case, with curvature contributions being negligible by comparison. This dominance of tangential strain allowed the turbulent flame behavior to be effectively compared with one-dimensional counterflow strained flamelets. As the mass flow rate and consequently the tangential strain rate was increased, the progress variable source term peak shifted toward higher values, indicating enhanced flame reactivity. The consumption speed was observed to initially increase with tangential strain, exhibiting behavior characteristic of mixtures with negative Markstein length. However, beyond a critical value of mean tangential strain rate of approximately 12000 s^{-1}, the consumption speed began to decrease, suggesting a transition in the flame response to tangential strain. A particularly significant finding in the presented analysis is the reduction in NO production at elevated tangential strain rates, demonstrating that the latter can be effectively leveraged to mitigate emissions in hydrogen combustion systems, as hydrogen can sustain high strain levels before extinction. This trend was consistently observed in both the turbulent flame simulations and corresponding laminar flamelet calculations, reinforcing the potential of strain-based approaches to emission control in practical applications. Notably, this study provides the first evidence of NO reduction due to tangential strain effects in a practical premixed hydrogen–air flame configuration. It was shown that doubling the mass flow rate from Case 1 to Case 3 leads to an averaged increase in the flame-tangential strain rate of 23.9%, which in turn results in an almost 43% reduction in NO emissions per kW compared to the nominal case. The results highlight the crucial role of tangential strain in governing both the combustion characteristics and emission formation in bluff-body stabilized hydrogen flames. Moreover, it was also demonstrated that it is possible to control NO_x formation through tangential strain manipulation, offering promising avenues for optimizing hydrogen combustion systems applications where emissions reduction is critical.

8 Conclusions and Outlooks

8.1 Summary and Conclusions

This work presents an investigation of turbulent hydrogen–air flames using large eddy simulations, with particular emphasis on a lean premixed configuration subjected to high tangential strain rates. The study is organized into three main parts, each addressing key aspects of modeling and physical interpretation.

In Chapter 5, the capability of flamelet-based models in their baseline formulation was assessed using a commercial solver. The objective was to evaluate the current applicability of models originally developed for hydrocarbon fuels to hydrogen combustion, considering both premixed and non-premixed configurations. The results showed that the baseline models provide accurate predictions of the velocity field and its fluctuations in both cases. Furthermore, the main features of the flame structure were well captured, as demonstrated by comparison with experimental OH*-chemiluminescence data. However, some limitations were identified. In particular, the models were not able to correctly predict the lift-off behavior in the HYLON case. Additionally, for the premixed configuration, the lack of experimental temperature data prevented a detailed assessment of differential diffusion effects and their role in the redistribution of the mixture fraction, which could potentially lead to superadiabatic temperatures.

In Chapter 6, the NTNU burner was investigated using a flamelet model both with and without differential diffusion effects. The aim was to assess the importance of these effects and to quantify their impact on the predicted flow and flame characteristics. The results indicated that differential diffusion has a negligible impact on the velocity field and its fluctuations. In contrast, a significant influence was observed on the flame structure. When differential diffusion effects were included, the model predicted a shorter flame and a shift of the reaction rate peak toward the edge of the bluff body, in closer agreement with experimental observations. Moreover, strong molecular diffusion effects, characteristic of lean premixed hydrogen–air flames, led to a redistribution of the mixture fraction and to the emergence of superadiabatic

temperatures, which were not captured by the baseline model. This redistribution was found to be particularly pronounced at the edge of the bluff body, where flame stabilization occurs.

A key finding of this work is that the observed redistribution of the mixture fraction is primarily driven by tangential strain rate effects, which were found to dominate over curvature effects. Interestingly, the model was able to capture the increase in the progress variable reaction rate with increasing strain without relying on a strained flamelet database, effectively reproducing the behavior of mixtures characterized by negative Markstein length. These results suggest that, within the LES framework and for the investigated conditions, an unstretched flamelet database can effectively reproduce the key physical mechanisms governing lean premixed hydrogen flames, including the coupling between strain, curvature, and differential diffusion.

In Chapter 7, the impact of tangential strain rate on NO emissions in a lean premixed hydrogen–air flame was investigated using large eddy simulations coupled with an ESF-based transported FDF approach. The analysis was carried out on the NTNU burner, considering different operating conditions corresponding to increasing levels of tangential strain rate obtained by varying the inlet mass flow rate.

The model was first validated against available experimental data, showing good agreement in the prediction of both mean velocity fields and their fluctuations in reactive and non-reactive conditions. This confirms the capability of the adopted LES–FDF framework to accurately reproduce the main flow features and provides a solid basis for the subsequent analysis of emission formation.

The results highlighted the dominant role of tangential strain rate in governing both flame structure and pollutant formation. In agreement with the findings of Chapter 6, tangential strain effects were found to be predominant over curvature, particularly in the shear layer region where the flame stabilizes. The increase in tangential strain led to enhanced local mixing and modified thermochemical states, primarily through changes in temperature and radical concentrations, which are known to strongly influence NO formation pathways.

Another key outcome of this study is that increasing the tangential strain rate results in a significant reduction of NO emissions. In particular, an increase in the inlet mass flow rate leading to higher strain levels produced a marked decrease in NO emissions per unit thermal power, with reductions of up to approximately 40% compared to the nominal operating condition. This behavior is attributed to a redistribution of O and H radicals, strongly influenced by flame stretch, which reduces the contribution of the NNH pathway and consequently leads to a decrease in NO production.

The comparison with one-dimensional counterflow simulations further confirmed that the LES framework is able to capture the qualitative trends associated with increasing tangential strain, demonstrating consistency between canonical and turbulent configurations. This supports the validity of using LES to investigate the coupling between strain and emissions in realistic combustion systems.

Overall, the findings of this chapter demonstrate that tangential strain rate rep-

resents a key controlling parameter for NO emissions in lean premixed hydrogen flames. The results indicate that, beyond its impact on flame stabilization and structure, strain can be effectively exploited as a design parameter to mitigate pollutant formation. These insights provide valuable guidance for the development of low-emission hydrogen combustion systems and highlight the importance of accurately capturing strain effects within high-fidelity numerical frameworks.

8.2 Future Work

This work concludes with suggestions for future research on hydrogen combustion and LES modeling, together with remarks on the current modeling framework and directions for further studies. The main recommendations are summarized below:

- In Chapter 5, the HYLON burner was investigated. The analysis based on the Takeno index showed that the flame exhibits multiple combustion regimes. This poses challenges for the application of flamelet models, which are typically developed for either premixed or non-premixed conditions. Further efforts are therefore required to develop modeling approaches capable of handling multiple combustion regimes within a single, efficient framework.

- In Chapter 6, a model accounting for differential diffusion effects was employed. The results indicated that constructing the look-up table using only unstretched flamelets is sufficient to capture key features of strained flames, such as the distribution of mixture fraction and the increase in the progress variable reaction rate associated with mixtures characterized by a negative Markstein length. However, further investigations are needed to assess the quantitative accuracy of this approach and to define the strain rate regimes over which it remains valid. The potential advantages of incorporating strain rate as an additional parameter in the manifold, along with the identification of an appropriate controlling variable, should also be explored. Moreover, the current model is limited to four controlling variables and does not include enthalpy, which is essential for accurately accounting for heat losses. As reported in [258], including enthalpy among the controlling variables can improve the prediction of the consumption speed. Finally, the model employs variance equations derived under the assumption of unity Lewis number mixtures. A rigorous derivation of variance equations for both mixture fraction and progress variable, applicable to non-unity Lewis number conditions, would be beneficial. A comparison with the current formulation should be carried out to assess whether significant differences arise.

- In Chapter 7, a transported PDF method based on the ESF approach was used to investigate the effects of tangential strain rate on NO emissions in a practical

configuration. The results were found to be consistent with previous studies on strained laminar and turbulent DNS cases. However, the analysis at higher strain levels remains purely numerical, and experimental data are required to validate these findings, despite the consistency of the observed trends with the literature. Furthermore, Soret effects were neglected in this study. It is known that these effects can play a significant role, particularly in lean premixed hydrogen–air flames under high levels of tangential strain rate, influencing both the consumption speed and NO formation. Therefore, for a quantitative comparison between LES results and future experimental data, Soret effects should be included. The same consideration applies to the flamelet model used in Chapter 6.

Bibliography

1. **Valérie Masson-Delmotte** et al. “Climate change 2021: the physical science basis”. In: *Contribution of working group I to the sixth assessment report of the intergovernmental panel on climate change* 2.1 (2021), p. 2391. DOI: doi.org/10.1017/9781009157896.
2. **Andrew A. Lacis** et al. “Atmospheric CO_2: Principal Control Knob Governing Earth’s Temperature”. In: *Science* 330.6002 (2010), pp. 356–359. DOI: 10.1126/science.1190653.
3. **Royal Society** and **National Academy** of **Sciences**. *Climate change: Evidence & causes*. Royal Society, 2020. URL: https://royalsociety.org/-/media/policy/projects/climate-evidence-causes/climate-change-evidence-causes.pdf.
4. **Copernicus Climate Change Service (C3S)**. *European State of the Climate 2024*. Accessed: 2025-12-30. 2024. URL: https://climate.copernicus.eu/esotc/2024.
5. **Colin P Morice** et al. “An updated assessment of near-surface temperature change from 1850: The HadCRUT5 data set”. In: *Journal of Geophysical Research: Atmospheres* 126.3 (2021), e2019JD032361. DOI: https://doi.org/10.1029/2019JD032361.
6. **Noah S. Diffenbaugh** and **Marshall Burke**. “Global warming has increased global economic inequality”. In: *Proceedings of the National Academy of Sciences* 116.20 (2019), pp. 9808–9813. DOI: https://doi.org/10.1073/pnas.1816020116.
7. **IPCC**. *Climate Change 2021: The Physical Science Basis. Chapter 9: Ocean, Cryosphere and Sea Level Change*. Tech. rep. Cambridge University Press, 2021. URL: https://www.ipcc.ch/report/ar6/wg1/chapter/chapter-9/.

8. **IPCC**. *Climate Change 2021: The Physical Science Basis. Chapter 11: Weather and Climate Extreme Events in a Changing Climate*. Tech. rep. Cambridge University Press, 2021. URL: https://www.ipcc.ch/report/ar6/wg1/chapter/chapter-11/.

9. **IPCC**. *Climate Change 2023: Synthesis Report*. Tech. rep. Cambridge University Press, 2023. URL: https://www.ipcc.ch/report/ar6/syr/.

10. **IPCC**. *Climate Change 2022: Mitigation of Climate Change. Contribution of Working Group III to the Sixth Assessment Report*. Tech. rep. Cambridge University Press, 2022. DOI: 10.1017/9781009157926.

11. **Joint Research Centre (JRC) European Commission**. *GHG emissions of all world countries – 2025*. Publications Office of the European Union, 2025. DOI: doi/10.2760/9816914.

12. **Statista**. *Greenhouse gas emissions worldwide by sector*. Total GHG emissions: 57.7 Gt CO_2-eq in 2024. 2025. URL: https://www.statista.com/chart/33334/greenhouse-gas-emissions-worldwide-by-sector/.

13. **Hannah Ritchie**, **Pablo Rosado**, and **Max Roser**. "CO_2 and Greenhouse Gas Emissions". In: *Our World in Data* (2023). URL: https://ourworldindata.org/co2-and-greenhouse-gas-emissions.

14. **Climate Watch, World Resources Institute**. *Climate Watch Historical Emissions Data Explorer*. Accessed: 2025-01-19. Licensed under Creative Commons Attribution 4.0 (CC BY 4.0). 2025. URL: https://www.climatewatchdata.org/data-explorer/historical-emissions.

15. **Business Europe**. *Decarbonisation in the aviation and maritime sectors*. 2021. URL: https://www.businesseurope.eu/wp-content/uploads/2025/02/2021-03-24_pp_alternative_fuels_aviation_and_maritime-85b-1.pdf.

16. **Binny Bagga**. "The Future of Fossil Fuels: Renewable Energy—Wind and Solar". In: *Sustainability in the Oil and Gas Sector: Adaptation and Mitigation Strategies for Tackling Climate Change*. Ed. by **Thomas Walker**, **Sergey Barabanov**, and **Victoria Michaeli** Maya nd Kelly. Cham: Springer Nature Switzerland, 2024, pp. 65–94. DOI: 10.1007/978-3-031-51586-6_4.

17. **International Energy Agency**. *Net Zero by 2050: A Roadmap for the Global Energy Sector*. Accessed: 2025-01-02. Paris: International Energy Agency (IEA), 2021. URL: https://iea.blob.core.windows.net/assets/deebef5d-0c34-4539-9d0c-10b13d840027/NetZeroby2050-ARoadmapfortheGlobalEnergySector.pdf.

18. **A. Dreizler** et al. "The role of combustion science and technology in low and zero impact energy transformation processes". In: *Applications in Energy and Combustion Science* 7 (2021), p. 100040. ISSN: 2666-352X. DOI: https://doi.org/10.1016/j.jaecs.2021.100040.

19. **Hydrogen Council** and **McKinsey & Company**. *Hydrogen Insights 2024*. Accessed: 2025-01-02. Brussels: Hydrogen Council, 2024. URL: https://hydrogencouncil.com/en/hydrogen-insights-2024/.

20. **Lorenzo Folcarelli** et al. "A Chemical Reactor Network methodology for estimating NOx emissions under non-premixed lean hydrogen combustion with water injection". In: *International Journal of Hydrogen Energy* 168 (2025), p. 150561. DOI: https://doi.org/10.1016/j.ijhydene.2025.150561.

21. **Heinz Pitsch**. "The transition to sustainable combustion: Hydrogen- and carbon-based future fuels and methods for dealing with their challenges". In: *Proceedings of the Combustion Institute* 40.1 (2024), p. 105638. ISSN: 1540-7489. DOI: https://doi.org/10.1016/j.proci.2024.105638.

22. **Haifeng Liu** et al. "Deployment of hydrogen in hard-to-abate transport sectors under limited carbon dioxide removal (CDR): Implications on global energy-land-water system". In: *Renewable and Sustainable Energy Reviews* 184 (2023), p. 113578. ISSN: 1364-0321. DOI: https://doi.org/10.1016/j.rser.2023.113578.

23. **Hydrogen Council**. *Hydrogen Insights 2024*. 2024. URL: https://hydrogencouncil.com/en/hydrogen-insights-2024/.

24. **B.E. Milton** and **J.C. Keck**. "Laminar burning velocities in stoichiometric hydrogen and hydrogen-hydrocarbon gas mixtures". In: *Combustion and Flame* 58.1 (1984), pp. 13–22. ISSN: 0010-2180. DOI: https://doi.org/10.1016/0010-2180(84)90074-9.

25. **Zuohua Huang** et al. "Measurements of laminar burning velocities for natural gas–hydrogen–air mixtures". In: *Combustion and Flame* 146.1 (2006), pp. 302–311. DOI: https://doi.org/10.1016/j.combustflame.2006.03.003.

26. **Antonio L. Sánchez** and **Forman A. Williams**. "Recent advances in understanding of flammability characteristics of hydrogen". In: *Progress in Energy and Combustion Science* 41 (2014), pp. 1–55. DOI: https://doi.org/10.1016/j.pecs.2013.10.002.

27. **Haiqin Zhou** et al. "Hydrogen-fueled gas turbines in future energy system". In: *International Journal of Hydrogen Energy* 64 (2024), pp. 569–582. DOI: https://doi.org/10.1016/j.ijhydene.2024.03.327.

28. **Mohammad Alhuyi Nazari** et al. "Utilization of hydrogen in gas turbines: A comprehensive review". In: *International Journal of Low-Carbon Technologies* 17 (2022), pp. 513–519. DOI: https://doi.org/10.1093/ijlct/ctac025.

29. **Pavlos Nikolaidis** and **Andreas Poullikkas**. "A comparative overview of hydrogen production processes". In: *Renewable and sustainable energy reviews* 67 (2017), pp. 597–611. DOI: http://dx.doi.org/10.1016/j.rser.2016.09.044.

30. **Richa Kothari**, **D Buddhi**, and **RL Sawhney**. “Comparison of environmental and economic aspects of various hydrogen production methods”. In: *Renewable and Sustainable Energy Reviews* 12.2 (2008), pp. 553–563. DOI: https://doi.org/10.1016/j.rser.2006.07.012.

31. **Havva Balat** and **Elif Kırtay**. “Hydrogen from biomass–present scenario and future prospects”. In: *International journal of hydrogen energy* 35.14 (2010), pp. 7416–7426. DOI: https://doi.org/10.1016/j.ijhydene.2010.04.137.

32. **Jimena Incer-Valverde** et al. ““Colors” of hydrogen: Definitions and carbon intensity”. In: *Energy conversion and management* 291 (2023), p. 117294. DOI: https://doi.org/10.1016/j.enconman.2023.117294.

33. **James A Scobie** et al. “Review of ingress in gas turbines”. In: *Journal of Engineering for Gas Turbines and Power* 138.12 (2016), p. 120801. DOI: https://doi.org/10.1115/1.4033938.

34. **S Manigandan** et al. “Role of hydrogen on aviation sector: A review on hydrogen storage, fuel flexibility, flame stability, and emissions reduction on gas turbines engines”. In: *Fuel* 352 (2023), p. 129064. DOI: https://doi.org/10.1016/j.fuel.2023.129064.

35. **Nageswara Rao Muktinutalapati**. “Materials for gas turbines–an overview”. In: *Advances in gas turbine technology* 23 (2011). DOI: 10.5772/20730.

36. **VM Maslennikov** and **V Ja Shterenberg**. “Advanced gas turbine system utilizing partial oxidation technology for ecologically clean power generation”. In: *International Journal of Low-Carbon Technologies* 6.1 (2011), pp. 55–63. DOI: https://doi.org/10.1093/ijlct/ctq043.

37. **Booma Devi** et al. “Influence of high oxygenated biofuels on micro-gas turbine engine for reduced emission”. In: *Aircraft Engineering and Aerospace Technology* 93.3 (2021), pp. 508–513. DOI: https://doi.org/10.1108/AEAT-07-2020-0150.

38. **Raghav Gupta** and **Mohd Faisal Jalil**. “An Overview of Using Hydrogen in Transportation Sector as Fuel”. In: *Renewable Power for Sustainable Growth: Proceedings of International Conference on Renewal Power (ICRP 2020)*. Springer. 2021, pp. 509–517. DOI: https://doi.org/10.1007/978-981-33-4080-0_49.

39. **Simon Öberg**, **Mikael Odenberger**, and **Filip Johnsson**. “Exploring the competitiveness of hydrogen-fueled gas turbines in future energy systems”. In: *International Journal of Hydrogen Energy* 47.1 (2022), pp. 624–644. DOI: https://doi.org/10.1016/j.ijhydene.2021.10.035.

40. **Simon Öberg**, **Mikael Odenberger**, and **Filip Johnsson**. “The value of flexible fuel mixing in hydrogen-fueled gas turbines–a techno-economic study”. In: *International Journal of Hydrogen Energy* 47.74 (2022), pp. 31684–31702. DOI: https://doi.org/10.1016/j.ijhydene.2022.07.075.

41. **Alessandro Cappelletti** and **Francesco Martelli**. “Investigation of a pure hydrogen fueled gas turbine burner”. In: *International Journal of Hydrogen Energy* 42.15 (2017), pp. 10513–10523. DOI: https://doi.org/10.1016/j.ijhydene.2017.02.104.

42. **David Noble** et al. “Assessment of current capabilities and near-term availability of hydrogen-fired gas turbines considering a low-carbon future”. In: *Journal of Engineering for Gas Turbines and Power* 143.4 (2021), p. 041002. DOI: https://doi.org/10.1115/1.4049346.

43. **Seyed Ehsan Hosseini** and **Brayden Butler**. “An overview of development and challenges in hydrogen powered vehicles”. In: *International journal of green energy* 17.1 (2020), pp. 13–37. DOI: https://doi.org/10.1080/15435075.2019.1685999.

44. **Elena Stefan** et al. “Materials challenges in hydrogen-fuelled gas turbines”. In: *International Materials Reviews* 67.5 (2022), pp. 461–486. DOI: https://doi.org/10.1080/09506608.2021.1981706.

45. **Milos B Djukic** et al. “Hydrogen damage of steels: A case study and hydrogen embrittlement model”. In: *Engineering Failure Analysis* 58 (2015), pp. 485–498. DOI: https://doi.org/10.1016/j.engfailanal.2015.05.017.

46. **Meng Ni**. “An overview of hydrogen storage technologies”. In: *Energy exploration & exploitation* 24.3 (2006), pp. 197–209. DOI: https://doi.org/10.1260/014459806779367455.

47. **IA Hassan** et al. “Hydrogen storage technologies for stationary and mobile applications: Review, analysis and perspectives”. In: *Renewable and Sustainable Energy Reviews* 149 (2021), p. 111311. DOI: https://doi.org/10.1016/j.rser.2021.111311.

48. **AG Olabi** et al. “Large-vscale hydrogen production and storage technologies: Current status and future directions”. In: *International Journal of Hydrogen Energy* 46.45 (2021), pp. 23498–23528. DOI: https://doi.org/10.1016/j.ijhydene.2020.10.110.

49. **Taspia Shawkat Chowdhury** et al. “A critical review on gas turbine cooling performance and failure analysis of turbine blades”. In: *International journal of thermofluids* 18 (2023), p. 100329. DOI: https://doi.org/10.1016/j.ijft.2023.100329.

50. **Abdel-Hamid I Mourad** et al. “Failure analysis of gas and wind turbine blades: A review”. In: *Engineering Failure Analysis* 146 (2023), p. 107107. DOI: https://doi.org/10.1016/j.engfailanal.2023.107107.

51. **Mojtaba Rajabinezhad** et al. “Corrosion-fatigue failure of gas-turbine blades in an oil and gas production plant”. In: *Materials* 13.4 (2020), p. 900. DOI: https://doi.org/10.3390/ma13040900.

52. **Kuiying Chen**, **Dongyi Seo**, and **Pervez Canteenwalla**. “The effect of high-temperature water vapour on degradation and failure of hot section components of gas turbine engines”. In: *Coatings* 11.9 (2021), p. 1061. DOI: https://doi.org/10.3390/coatings11091061.

53. **G Yu**, **CK Law**, and **CK Wu**. “Laminar flame speeds of hydrocarbon+ air mixtures with hydrogen addition”. In: *Combustion and flame* 63.3 (1986), pp. 339–347. DOI: https://doi.org/10.1016/0010-2180(86)90003-9.

54. **Muhammad Shakeel Ahmad**, **Mohd Syukri Ali**, and **Nasrudin Abd Rahim**. “Hydrogen energy vision 2060: Hydrogen as energy Carrier in Malaysian primary energy mix–Developing P2G case”. In: *Energy Strategy Reviews* 35 (2021), p. 100632. DOI: https://doi.org/10.1016/j.esr.2021.100632.

55. **Dominik Ebi** and **Peter Jansohn**. “Boundary layer flashback limits of hydrogen-methane-air flames in a generic swirl burner at gas turbine-relevant conditions”. In: *Journal of Engineering for Gas Turbines and Power* 143.8 (2021), p. 081011. DOI: https://doi.org/10.1115/1.4049777.

56. **Brent B Skabelund** et al. “Thermodynamic and emission analysis of a hydrogen/methane fueled gas turbine”. In: *Energy Conversion and Management: X* 19 (2023), p. 100394. DOI: https://doi.org/10.1016/j.ecmx.2023.100394.

57. **Bo Zhang** et al. “Thermodynamic, environmental, and optimization of a new power generation system driven by a gas turbine cycle”. In: *Energy Reports* 6 (2020), pp. 2531–2548. DOI: https://doi.org/10.1016/j.egyr.2020.09.003.

58. **Felipe Bolaños** et al. “Study of a rich/lean staged combustion concept for hydrogen at gas turbine relevant conditions”. In: *Turbo Expo: Power for Land, Sea, and Air*. Vol. 55102. American Society of Mechanical Engineers. 2013, V01AT04A031. DOI: https://doi.org/10.1115/GT2013-94420.

59. **Hong Liu**, **Zhuoxiong Zeng**, and **Kaifang Guo**. “Numerical analysis on hydrogen swirl combustion and flow characteristics of a micro gas turbine combustor with axial air/fuel staged technology”. In: *Applied Thermal Engineering* 219 (2023), p. 119460. DOI: https://doi.org/10.1016/j.applthermaleng.2022.119460.

60. **Yize Liu** et al. “Review of modern low emissions combustion technologies for aero gas turbine engines”. In: *Progress in Aerospace Sciences* 94 (2017), pp. 12–45. DOI: https://doi.org/10.1016/j.paerosci.2017.08.001.

61. **Tieyi Tan**, **Weijun Fan**, and **Rongchun Zhang**. "Study on hydrogen staged combustion for gas turbine". In: *Fuel* 349 (2023), p. 128700. DOI: https://doi.org/10.1016/j.fuel.2023.128700.

62. **Xiulei Wang** et al. "Advances on materials design and manufacture technology of plastic liner of type IV hydrogen storage vessel". In: *International journal of hydrogen energy* 47.13 (2022), pp. 8382–8408. DOI: https://doi.org/10.1016/j.ijhydene.2021.12.198.

63. **Weiming Xu** et al. "The role of nitric oxide in cancer". In: *Cell research* 12.5 (2002), pp. 311–320. DOI: https://doi.org/10.1038/sj.cr.7290133.

64. **N. Peters**. "Multiscale combustion and turbulence". In: *Proceedings of the Combustion Institute* 32.1 (2009), pp. 1–25. ISSN: 1540-7489. DOI: https://doi.org/10.1016/j.proci.2008.07.044.

65. **A. Khelil** et al. "Prediction of a high swirled natural gas diffusion flame using a PDF model". In: *Fuel* 88.2 (2009), pp. 374–381. ISSN: 0016-2361. DOI: https://doi.org/10.1016/j.fuel.2008.09.008.

66. **Zhichao Wang** and **Xiaoyi Yang**. "NOx formation mechanism and emission prediction in turbulent combustion: a review". In: *Applied Sciences* 14.14 (2024), p. 6104. DOI: https://doi.org/10.3390/app14146104.

67. **Y. B. Zeldovich**. "The Oxidation of Nitrogen in Combustion and Explosions". In: *Chemical Physics and Hydrodynamics*. Princeton: Princeton University Press, 2014, pp. 364–403. ISBN: 9781400862979. DOI: doi:10.1515/9781400862979.364.

68. **G. Löffler** et al. "NOx formation in natural gas combustion - a new simplified reaction scheme for CFD calculations". In: *Fuel* 85.4 (2006), pp. 513–523. ISSN: 0016-2361. DOI: https://doi.org/10.1016/j.fuel.2005.07.012. URL: https://www.sciencedirect.com/science/article/pii/S001623610500253X.

69. **Cheol-Hong Hwang**, **Seung-Ho Hyun**, and **Chang-Eon Lee**. "Effects of Heat Loss on NOx Emission in the Postflame Region of Premixed CH4Air Combustion". In: *Energy & Fuels* 22.2 (2008), pp. 996–1003. DOI: 10.1021/ef700604f.

70. **Joanna Blauwens**, **Bruno Smets**, and **Jozef Peeters**. "Mechanism of "prompt" no formation in hydrocarbon flames". In: *Symposium (International) on Combustion* 16.1 (1977), pp. 1055–1064. ISSN: 0082-0784. DOI: https://doi.org/10.1016/S0082-0784(77)80395-0.

71. **Zhongya Xi** et al. "Numerical investigation on flow characteristics and emissions under varying swirler vane angle in a lean premixed combustor". In: *Case Studies in Thermal Engineering* 31 (2022), p. 101800. ISSN: 2214-157X. DOI: https://doi.org/10.1016/j.csite.2022.101800.

72. **Songlin Liu** and **Wenkun Zhu**. "A comprehensive review on the significant role of nitrous oxide in the transformation of nitrogen oxides during combustion". In: *Journal of the Energy Institute* 116 (2024), p. 101678. ISSN: 1743-9671. DOI: https://doi.org/10.1016/j.joei.2024.101678.

73. **Shunta Xu** et al. "NO formation and reduction during methane/hydrogen MILD combustion over a wide range of hydrogen-blending ratios in a well-stirred reactor". In: *Fuel* 346 (2023), p. 128324. ISSN: 0016-2361. DOI: https://doi.org/10.1016/j.fuel.2023.128324.

74. **A.A. Konnov**, **G. Colson**, and **J. De Ruyck**. "NO formation rates for hydrogen combustion in stirred reactors". In: *Fuel* 80.1 (2001), pp. 49–65. ISSN: 0016-2361. DOI: https://doi.org/10.1016/S0016-2361(00)00060-0.

75. **Earl L. Merryman** and **Arthur Levy**. "Nitrogen oxide formation in flames: The roles of NO2 and fuel nitrogen". In: *Symposium (International) on Combustion* 15.1 (1975). Fifteenth Symposium (International) on Combustion, pp. 1073–1083. ISSN: 0082-0784. DOI: https://doi.org/10.1016/S0082-0784(75)80372-9.

76. **A. H. Lefebvre**. "Lean Premixed/Prevaporized Combustion". In: *Proceedings of the Workshop on Lean Premixed/Prevaporized Combustion*. NASA Conference Publication NASA-CP-2016. Accessed: 2025-04-23. Cleveland, OH, USA: NASA, Jan. 1977, E-9255. URL: https://ntrs.nasa.gov/citations/19770026353 (visited on 04/23/2025).

77. **David M Dias**, **Pedro R Resende**, and **Alexandre M Afonso**. "A Review on Micro-Combustion Flame Dynamics and Micro-Propulsion Systems". In: *Energies* 17.6 (2024), p. 1327. DOI: https://doi.org/10.3390/en17061327.

78. **C.K. Law**. *Combustion Physics*. Cambridge University Press, 2010. URL: https://books.google.it/books?id=vWgJvKMXwQ8C.

79. **Tim C. Lieuwen**. *Unsteady Combustor Physics*. Cambridge University Press, 2012. DOI: https://doi.org/10.1017/CBO9781139059961.

80. **Wojciech Jerzak** and **Monika Kuźnia**. "Experimental study of impact of swirl number as well as oxygen and carbon dioxide content in natural gas combustion air on flame flashback and blow-off". In: *Journal of Natural Gas Science and Engineering* 29 (2016), pp. 46–54. ISSN: 1875-5100. DOI: https://doi.org/10.1016/j.jngse.2015.12.054.

81. **Denis Thibaut** and **Sebastien Candel**. "Numerical study of unsteady turbulent premixed combustion: Application to flashback simulation". In: *Combustion and Flame* 113.1-2 (1998), pp. 53–65. DOI: https://doi.org/10.1016/S0010-2180(97)00196-X.

82. **A.C. Benim** and **K.J. Syed**. *Flashback Mechanisms in Lean Premixed Gas Turbine Combustion*. Academic Press, 2014. ISBN: 9780128008263. URL: https://books.google.it/books?id=o3ODBAAAQBAJ.

83. **Christoph D.K. Schumann** et al. "A priori and a posteriori analyses of differential and preferential diffusion in large eddy simulations of partially premixed hydrogen–air flames". In: *Combustion and Flame* 283 (2026), p. 114537. ISSN: 0010-2180. DOI: https://doi.org/10.1016/j.combustflame.2025.114537.

84. **Pasquale Eduardo Lapenna** et al. "Hydrogen laminar flames". In: *Hydrogen for Future Thermal Engines*. Springer, 2023, pp. 93–139. DOI: https://doi.org/10.1007/978-3-031-28412-0_3.

85. **Mustafa İlbaş**, **Serhat Karyeyen**, and **İlker Yilmaz**. "Effect of swirl number on combustion characteristics of hydrogen-containing fuels in a combustor". In: *International Journal of Hydrogen Energy* 41.17 (2016). Special Issue on 17th International Conference on Emerging Nuclear Energy Systems (ICENES'2015), 4-8 October 2015, Istanbul, Turkey, pp. 7185–7191. ISSN: 0360-3199. DOI: https://doi.org/10.1016/j.ijhydene.2015.12.107.

86. **Ivan Langella** et al. "Large-eddy simulation of reacting flows in industrial gas turbine combustor". In: *Journal of Propulsion and Power* 34.5 (2018), pp. 1269–1284. DOI: https://doi.org/10.2514/1.B36842.

87. **S. Marragou** et al. "Modeling of H2/air flame stabilization regime above coaxial dual swirl injectors". In: *Combustion and Flame* 255 (2023), p. 112908. ISSN: 0010-2180. DOI: https://doi.org/10.1016/j.combustflame.2023.112908.

88. **Catherine J Goy**, **Stuart R James**, **Suzanne Rea**, et al. "Monitoring combustion instabilities: E. ON UK's experience". In: *Progress in Astronautics and Aeronautics* 210 (2005), p. 163. DOI: https://doi.org/10.2514/5.9781600866807.0163.0175.

89. **Sarah Link** et al. "Experimental analysis of dual-fuel (CH4/H2) capability in a partially-premixed swirl stabilized combustor". In: *International Journal of Hydrogen Energy* 101 (2025), pp. 427–437. ISSN: 0360-3199. DOI: https://doi.org/10.1016/j.ijhydene.2024.12.286.

90. **TNF Workshop**. *HYLON Phase 2 – Hydrogen/air flames in a dual swirl coaxial injector (IMFT/CERFACS and KAUST)*. Accessed: February 24, 2026. TNF Workshop, 2026. URL: https://tnfworkshop.org/hylon2/.

91. **TNF Workshop**. *Bluff body hydrogen flame (NTNU, Trondheim)*. Accessed: February 24, 2026. TNF Workshop, 2026. URL: https://tnfworkshop.org/bluff-body-hydrogen-flame-ntnu-trondheim/.

92. **Harald H.-W. Funke** et al. “30 Years of Dry-Low-NOx Micromix Combustor Research for Hydrogen-Rich Fuels—An Overview of Past and Present Activities”. In: *Journal of Engineering for Gas Turbines and Power* 143.7 (Mar. 2021), p. 071002. DOI: 10.1115/1.4049764.

93. **Dan Zhao**, **Ephraim Gutmark**, and **Philip de Goey**. “A review of cavity-based trapped vortex, ultra-compact, high-g, inter-turbine combustors”. In: *Progress in Energy and Combustion Science* 66 (2018), pp. 42–82. ISSN: 0360-1285. DOI: https://doi.org/10.1016/j.pecs.2017.12.001.

94. **Swetaprovo Chaudhuri** et al. “Blowoff dynamics of bluff body stabilized turbulent premixed flames”. In: *Combustion and Flame* 157.4 (2010), pp. 790–802. ISSN: 0010-2180. DOI: https://doi.org/10.1016/j.combustflame.2009.10.020.

95. **Arthur H Lefebvre** and **Dilip R Ballal**. *Gas turbine combustion: alternative fuels and emissions*. CRC press, 2010. DOI: https://doi.org/10.1201/9781420086058.

96. **I. Esquiva-Dano**, **H.T. Nguyen**, and **D. Escudie**. “Influence of a bluff-body’s shape on the stabilization regime of non-premixed flames”. In: *Combustion and Flame* 127.4 (2001), pp. 2167–2180. ISSN: 0010-2180. DOI: https://doi.org/10.1016/S0010-2180(01)00318-2.

97. **T. Yahou** et al. “The role of preferential diffusion on the ignition dynamics of lean premixed hydrogen flames”. In: *Proceedings of the Combustion Institute* 40.1 (2024), p. 105612. ISSN: 1540-7489. DOI: https://doi.org/10.1016/j.proci.2024.105612.

98. **H.H.-W. Funke**, **N. Beckmann**, and **S. Abanteriba**. “An overview on dry low NOx micromix combustor development for hydrogen-rich gas turbine applications”. In: *International Journal of Hydrogen Energy* 44.13 (2019), pp. 6978–6990. ISSN: 0360-3199. DOI: https://doi.org/10.1016/j.ijhydene.2019.01.161.

99. **K Barlow** et al. “Trapped vortex combustor development for military aircraft”. In: (2008). URL: https://apps.dtic.mil/sti/tr/pdf/ADA478875.pdf.

100. **Song Chen** et al. “Numerical investigation of a trapped vortex miniature ramjet combustor”. In: *Journal of Propulsion and Power* 31.3 (2015), pp. 872–882. DOI: https://doi.org/10.2514/1.B35602.

101. **J.-Y Ren** et al. “Strain-rate effects on hydrogen-enhanced lean premixed combustion”. In: *Combustion and Flame* 124.4 (2001), pp. 717–720. ISSN: 0010-2180. DOI: https://doi.org/10.1016/S0010-2180(00)00205-4.

102. **Shinji Nakaya** et al. “Ignition and supersonic combustion behavior of liquid ethanol in a scramjet model combustor with cavity flame holder”. In: *Proceedings of the Combustion Institute* 35.2 (2015), pp. 2091–2099. ISSN: 1540-7489. DOI: https://doi.org/10.1016/j.proci.2014.07.023.

103. **Louis N. Cattafesta** et al. “Active control of flow-induced cavity oscillations”. In: *Progress in Aerospace Sciences* 44.7 (2008), pp. 479–502. ISSN: 0376-0421. DOI: https://doi.org/10.1016/j.paerosci.2008.07.002.

104. **Ludovic Chatellier**, **Janick Laumonier**, and **Yves Gervais**. “Active control of the aeroacoustics of cavity flows from the downstream edge”. In: *Comptes Rendus Mécanique* 334.4 (2006), pp. 259–265. ISSN: 1631-0721. DOI: https://doi.org/10.1016/j.crme.2006.03.003.

105. **Krishna Kant Agarwal**, **S. Krishna**, and **R. V. Ravikrishna**. “Mixing Enhancement in a Compact Trapped Vortex Combustor”. In: *Combustion Science and Technology* 185.3 (2013), pp. 363–378. DOI: 10.1080/00102202.2012.721034.

106. **Zhi-kai Wang** et al. “Effect of structure parameters of the flow guide vane on cold flow characteristics in trapped vortex combustor”. In: *Journal of Hydrodynamics* 27.5 (2015), pp. 730–737. DOI: https://doi.org/10.1016/S1001-6058(15)60535-2.

107. **Zejun Wu** et al. “Experimental and numerical studies on a trapped vortex combustor with different struts width”. In: *Applied Thermal Engineering* 91 (2015), pp. 91–104. ISSN: 1359-4311. DOI: https://doi.org/10.1016/j.applthermaleng.2015.06.068.

108. **V. R. Katta** and **W. M. Roquemore**. “Numerical Studies on Trapped-Vortex Concepts for Stable Combustion”. In: *Journal of Engineering for Gas Turbines and Power* 120.1 (Jan. 1998), pp. 60–68. DOI: 10.1115/1.2818088.

109. **Venkat Raman** and **Malik Hassanaly**. “Emerging trends in numerical simulations of combustion systems”. In: *Proceedings of the Combustion Institute* 37.2 (2019), pp. 2073–2089. ISSN: 1540-7489. DOI: https://doi.org/10.1016/j.proci.2018.07.121.

110. **Denis Veynante** and **Luc Vervisch**. “Turbulent combustion modeling”. In: *Progress in Energy and Combustion Science* 28.3 (2002), pp. 193–266. ISSN: 0360-1285. DOI: https://doi.org/10.1016/S0360-1285(01)00017-X.

111. **Tarek Echekki** and **Epaminondas Mastorakos**. *Turbulent Combustion Modeling: Advances, New Trends and Perspectives*. Vol. 95. Jan. 2011. ISBN: 978-94-007-0411-4. DOI: 10.1007/978-94-007-0412-1.

112. **Andrea Giusti** and **Epaminondas Mastorakos**. “Turbulent combustion modelling and experiments: Recent trends and developments”. In: *Flow, Turbulence and Combustion* 103.4 (2019), pp. 847–869. DOI: https://doi.org/10.1007/s10494-019-00072-6.

113. **Joseph C. Oefelein**. "Large eddy simulation of turbulent combustion processes in propulsion and power systems". In: *Progress in Aerospace Sciences* 42.1 (2006), pp. 2–37. ISSN: 0376-0421. DOI: https://doi.org/10.1016/j.paerosci.2006.02.001.

114. **Stephen B Pope**. "Turbulent Flows". In: *Measurement Science and Technology* 12.11 (Sept. 2001), p. 2020. DOI: 10.1088/0957-0233/12/11/705. URL: https://dx.doi.org/10.1088/0957-0233/12/11/705.

115. **C Priere** et al. "Large eddy simulation predictions of mixing enhancement for jets in cross-flows". In: *Journal of turbulence* 5.1 (2004), p. 005. DOI: 10.1088/1468-5248/5/1/005.

116. **Ulrich Schumann**. "Large-eddy simulation of turbulent diffusion with chemical reactions in the convective boundary layer". In: *Atmospheric Environment (1967)* 23.8 (1989), pp. 1713–1727. ISSN: 0004-6981. DOI: https://doi.org/10.1016/0004-6981(89)90056-5.

117. **Andrew Cook** and **James Riley**. "A Subgrid Model for Equilibrium Chemistry in Turbulent Flows". In: *Physics of Fluids - PHYS FLUIDS* 6 (Aug. 1994), pp. 2868–2870. DOI: 10.1063/1.868111.

118. **Massimo Germano** et al. "A dynamic subgrid-scale eddy viscosity model". In: *Physics of Fluids A: Fluid Dynamics* 3.7 (July 1991), pp. 1760–1765. ISSN: 0899-8213. DOI: 10.1063/1.857955.

119. **A. Kempf**, **A. Sadiki**, and **J. Janicka**. "Prediction of finite chemistry effects using large eddy simulation". In: *Proceedings of the Combustion Institute* 29.2 (2002), pp. 1979–1985. ISSN: 1540-7489. DOI: https://doi.org/10.1016/S1540-7489(02)80241-3.

120. **J. Janicka** and **A. Sadiki**. "Large eddy simulation of turbulent combustion systems". In: *Proceedings of the Combustion Institute* 30.1 (2005), pp. 537–547. ISSN: 1540-7489. DOI: https://doi.org/10.1016/j.proci.2004.08.279.

121. **Heinz Pitsch**. "Large-eddy simulation of turbulent combustion". In: *Annu. Rev. Fluid Mech.* 38.1 (2006), pp. 453–482. DOI: https://doi.org/10.1146/annurev.fluid.38.050304.092133.

122. **Norbert Peters**. "Turbulent combustion". In: *Measurement Science and Technology* 12.11 (2001), pp. 2022–2022. DOI: 10.1088/0957-0233/12/11/708.

123. **Thierry Poinsot** and **Denis Veynante**. *Theoretical and Numerical Combustion*. R.T. Edwards Inc., 2005, p. 522. URL: https://hal.science/hal-00270731.

124. **R.W. Bilger**. "Future progress in turbulent combustion research". In: *Progress in Energy and Combustion Science* 26.4 (2000), pp. 367–380. ISSN: 0360-1285. DOI: https://doi.org/10.1016/S0360-1285(00)00015-0.

125. **K.N.C. Bray** et al. “Finite rate chemistry and presumed PDF models for premixed turbulent combustion”. In: *Combustion and Flame* 146.4 (2006), pp. 665–673. ISSN: 0010-2180. DOI: https://doi.org/10.1016/j.combustflame.2006.07.001.

126. **A.N. Lipatnikov** et al. “A priori DNS study of applicability of flamelet concept to predicting mean concentrations of species in turbulent premixed flames at various Karlovitz numbers”. In: *Combustion and Flame* 222 (2020), pp. 370–382. ISSN: 0010-2180. DOI: https://doi.org/10.1016/j.combustflame.2020.09.001.

127. **Luis Valino**, **Radu Mustata**, and **Khaled Ben Letaief**. “Consistent behavior of Eulerian Monte Carlo fields at low Reynolds numbers”. In: *Flow, Turbulence and Combustion* 96.2 (2016), pp. 503–512. DOI: https://doi.org/10.1007/s10494-015-9687-0.

128. **Paola Breda** et al. “Validation of an Eulerian stochastic fields solver coupled with reaction–diffusion manifolds on LES of methane/air non-premixed flames”. In: *Flow, Turbulence and Combustion* 107.2 (2021), pp. 441–477. DOI: https://doi.org/10.1007/s10494-020-00235-w.

129. **Ehsan Abbasi-Atibeh** and **Jeffrey M. Bergthorson**. “Differential diffusion effects in counter-flow premixed hydrogen-enriched methane and propane flames”. In: *Proceedings of the Combustion Institute* 37.2 (2019), pp. 2399–2406. ISSN: 1540-7489. DOI: https://doi.org/10.1016/j.proci.2018.08.006.

130. **F.H. Vance** et al. “Quantifying the impact of heat loss, stretch and preferential diffusion effects to the anchoring of bluff body stabilized premixed flames”. In: *Combustion and Flame* 237 (2022), p. 111729. ISSN: 0010-2180. DOI: https://doi.org/10.1016/j.combustflame.2021.111729.

131. **Wm T Ashurst**, **N Peters**, and **MD Smooke**. “Numerical simulation of turbulent flame structure with non-unity Lewis number”. In: *Combustion science and technology* 53.4-6 (1987), pp. 339–375. DOI: https://doi.org/10.1080/00102208708947036.

132. **Gregory S. Jackson** et al. “Influence of H2 on the response of lean premixed CH4 flames to high strained flows”. In: *Combustion and Flame* 132.3 (2003), pp. 503–511. ISSN: 0010-2180. DOI: https://doi.org/10.1016/S0010-2180(02)00496-0.

133. **Eun-Seong Cho** and **Suk Ho Chung**. “Improvement of flame stability and NOx reduction in hydrogen-added ultra lean premixed combustion”. In: *Journal of Mechanical Science and Technology* 23.3 (2009), pp. 650–658. DOI: https://doi.org/10.1007/s12206-008-1223-x.

134. **Raymond L. Speth** and **Ahmed F. Ghoniem**. “Using a strained flame model to collapse dynamic mode data in a swirl-stabilized syngas combustor”. In: *Proceedings of the Combustion Institute* 32.2 (2009), pp. 2993–3000. ISSN: 1540-7489. DOI: https://doi.org/10.1016/j.proci.2008.05.072.

135. **J.A. van Oijen** et al. “State-of-the-art in premixed combustion modeling using flamelet generated manifolds”. In: *Progress in Energy and Combustion Science* 57 (2016), pp. 30–74. ISSN: 0360-1285. DOI: https://doi.org/10.1016/j.pecs.2016.07.001.

136. **Daoguan Ning**, **Aiwu Fan**, and **Hong Yao**. “Effects of fuel composition and strain rate on NO emission of premixed counter-flow H2/CO/air flames”. In: *International Journal of Hydrogen Energy* 42.15 (2017), pp. 10466–10474. ISSN: 0360-3199. DOI: https://doi.org/10.1016/j.ijhydene.2016.12.059.

137. **D. Bradley** et al. “The development and structure of flame instabilities and cellularity at low Markstein numbers in explosions”. In: *Combustion and Flame* 122.1 (2000), pp. 195–209. ISSN: 0010-2180. DOI: https://doi.org/10.1016/S0010-2180(00)00113-9.

138. **Lukas Berger**, **Antonio Attili**, and **Heinz Pitsch**. “Synergistic interactions of thermodiffusive instabilities and turbulence in lean hydrogen flames”. In: *Combustion and Flame* 244 (2022), p. 112254. ISSN: 0010-2180. DOI: https://doi.org/10.1016/j.combustflame.2022.112254.

139. **D R Stull** and **H Prophet**. *JANAF thermochemical tables, second edition:* en. Jan. 1971. DOI: https://doi.org/10.6028/NBS.NSRDS.37.

140. **G.K. Batchelor**. *An Introduction to Fluid Dynamics*. Cambridge Mathematical Library. Cambridge University Press, 2000. ISBN: 9781139643467. DOI: https://doi.org/10.1017/CBO9780511800955.

141. **F.A. Williams**. *Combustion Theory*. CRC Press, 2018. ISBN: 9780429973680. DOI: https://doi.org/10.1201/9780429494055.

142. **Alexandre Ern** and **Vincent Giovangigli**. *Multicomponent transport algorithms*. Springer, 1994. DOI: https://doi.org/10.1007/978-3-540-48650-3.

143. **J.O. Hirschfelder**, **C.F. Curtiss**, and **R.B. Bird**. *The Molecular Theory of Gases and Liquids*. Wiley, 1964. ISBN: 9780471400653. DOI: 10.1063/1.3061949. URL: https://books.google.it/books?id=dvvcEAAAQBAJ.

144. **Malik Hassanaly** et al. “A minimally-dissipative low-Mach number solver for complex reacting flows in OpenFOAM”. In: *Computers & Fluids* 162 (2018), pp. 11–25. ISSN: 0045-7930. DOI: https://doi.org/10.1016/j.compfluid.2017.11.020.

145. **Bamdad Lessani** and **Miltiadis V. Papalexandris**. “Time-accurate calculation of variable density flows with strong temperature gradients and combustion”. In: *Journal of Computational Physics* 212.1 (2006), pp. 218–246. ISSN: 0021-9991. DOI: https://doi.org/10.1016/j.jcp.2005.07.001.

146. **Amable Liñán**. “Diffusion-controlled Combustion”. In: *Mechanics for a New Mellennium*. Ed. by **Hassan Aref** and **James W. Phillips**. Dordrecht: Springer Netherlands, 2002, pp. 487–502. DOI: https://doi.org/10.1007/0-306-46956-1_31.

147. **Amable Liñán**. *On the Structure of Laminar Diffusion Flames*. Tech. rep. 1963. DOI: 10.21236/AD0432822.

148. **R.W. Bilger**, **S.H. Stårner**, and **R.J. Kee**. “On reduced mechanisms for methane-air combustion in nonpremixed flames”. In: *Combustion and Flame* 80.2 (1990), pp. 135–149. ISSN: 0010-2180. DOI: https://doi.org/10.1016/0010-2180(90)90122-8.

149. **David G. Goodwin** et al. *Cantera: An Object-oriented Software Toolkit for Chemical Kinetics, Thermodynamics, and Transport Processes*. https://www.cantera.org. Version 3.2.0. 2025. DOI: 10.5281/zenodo.17620923.

150. **T Poinsot**, **T Echekki**, and **MG Mungal**. “A study of the laminar flame tip and implications for premixed turbulent combustion”. In: *Combustion science and technology* 81.1-3 (1992), pp. 45–73. DOI: https://doi.org/10.1080/00102209208951793.

151. **Arnaud Trouvé** and **Thierry Poinsot**. “The evolution equation for the flame surface density in turbulent premixed combustion”. In: *Journal of Fluid Mechanics* 278 (1994), pp. 1–31. DOI: 10.1017/S0022112094003599.

152. **M. Matalon** and **B. J. Matkowsky**. “Flames as gasdynamic discontinuities”. In: *Journal of Fluid Mechanics* 124 (1982), pp. 239–259. DOI: 10.1017/S0022112082002481.

153. **Sebastien M. Candel** and **Thierry J. Poinsot**. “Flame Stretch and the Balance Equation for the Flame Area”. In: *Combustion Science and Technology* 70.1-3 (1990), pp. 1–15. DOI: 10.1080/00102209008951608.

154. **George H. Markstein**. “Experimental and Theoretical Studies of Flame-Front Stability”. In: *Dynamics of Curved Fronts*. Ed. by **Pierre Pelcé**. San Diego: Academic Press, 1988, pp. 413–423. ISBN: 978-0-12-550355-6. DOI: https://doi.org/10.1016/B978-0-08-092523-3.50045-9.

155. **G.H. Markstein**. *Nonsteady Flame Propagation: AGARDograph*. AGARDograph. Pergamon, 2014. ISBN: 9781483221625. URL: https://books.google.it/books?id=wICoBQAAQBAJ.

156. **E.A. Tingas**. *Hydrogen for Future Thermal Engines*. Green Energy and Technology. Springer International Publishing, 2023. ISBN: 9783031284120. DOI: https://doi.org/10.1007/978-3-031-28412-0.

157. **Moshe Matalon**. "Flame dynamics". In: *Proceedings of the Combustion Institute* 32.1 (2009), pp. 57–82. ISSN: 1540-7489. DOI: https://doi.org/10.1016/j.proci.2008.08.002.

158. **Francis Oppong** et al. "Intrinsic instability of different fuels spherically expanding flames: A review". In: *Fuel Processing Technology* 234 (2022), p. 107325. ISSN: 0378-3820. DOI: https://doi.org/10.1016/j.fuproc.2022.107325.

159. **Paul Clavin** and **Geoff Searby**. *Combustion Waves and Fronts in Flows: Flames, Shocks, Detonations, Ablation Fronts and Explosion of Stars*. Cambridge University Press, 2016. DOI: https://doi.org/10.1017/CBO9781316162453.

160. **Daniel Fernández-Galisteo**, **Vadim N. Kurdyumov**, and **Paul D. Ronney**. "Analysis of premixed flame propagation between two closely-spaced parallel plates". In: *Combustion and Flame* 190 (2018), pp. 133–145. ISSN: 0010-2180. DOI: https://doi.org/10.1016/j.combustflame.2017.11.022.

161. **C.K. Law**. "Dynamics of stretched flames". In: *Symposium (International) on Combustion* 22.1 (1989), pp. 1381–1402. ISSN: 0082-0784. DOI: https://doi.org/10.1016/S0082-0784(89)80149-3.

162. **A.T. Kirkpatrick** and **K.K. Kuo**. *Principles of Combustion*. Wiley, 2024. ISBN: 9781394187072. URL: https://books.google.it/books?id=uokoEQAAQBAJ.

163. **N. Peters**. "The turbulent burning velocity for large-scale and small-scale turbulence". In: *Journal of Fluid Mechanics* 384 (1999), pp. 107–132. DOI: 10.1017/S0022112098004212.

164. **Bernard Lewis** and **Guenther Von Elbe**. *Combustion, flames and explosions of gases*. Elsevier, 2012. DOI: https://doi.org/10.1016/C2009-0-21751-X.

165. **A Favre**. "Problems of hydrodynamics and continuum mechanics". In: *Soc. Indust.* (1969), pp. 231–266.

166. **Joseph Smagorinsky**. "General circulation experiments with the primitive equations: I. The basic experiment". In: *Monthly weather review* 91.3 (1963), pp. 99–164. DOI: https://doi.org/10.1175/1520-0493(1963)091<0099:GCEWTP>2.3.CO;2.

167. **Xiaochuan Chai** and **Krishnan Mahesh**. "Dynamic -equation model for large-eddy simulation of compressible flows". In: *Journal of Fluid Mechanics* 699 (2012), pp. 385–413. DOI: 10.1017/jfm.2012.115.

168. **Akira Yoshizawa**. "Statistical theory for compressible turbulent shear flows, with the application to subgrid modeling". In: *The Physics of Fluids* 29.7 (July 1986), pp. 2152–2164. ISSN: 0031-9171. DOI: 10.1063/1.865552.

169. **Heinz Pitsch** and **Helfried Steiner**. “Large-eddy simulation of a turbulent piloted methane/air diffusion flame (Sandia flame D)”. In: *Physics of fluids* 12.10 (2000), pp. 2541–2554. DOI: https://doi.org/10.1063/1.1288493.

170. **L.Y.M. Gicquel**, **G. Staffelbach**, and **T. Poinsot**. “Large Eddy Simulations of gaseous flames in gas turbine combustion chambers”. In: *Progress in Energy and Combustion Science* 38.6 (2012), pp. 782–817. ISSN: 0360-1285. DOI: https://doi.org/10.1016/j.pecs.2012.04.004.

171. **D.B. Spalding**. “Mixing and chemical reaction in steady confined turbulent flames”. In: *Symposium (International) on Combustion* 13.1 (1971). Thirteenth symposium (International) on Combustion, pp. 649–657. ISSN: 0082-0784. DOI: https://doi.org/10.1016/S0082-0784(71)80067-X.

172. **D. Brian Spalding**. “Development of the eddy-break-up model of turbulent combustion”. In: *Symposium (International) on Combustion* 16.1 (1977), pp. 1657–1663. ISSN: 0082-0784. DOI: https://doi.org/10.1016/S0082-0784(77)80444-X.

173. **Christer Fureby** and **S-I Moller**. “Large eddy simulation of reacting flows applied to bluff body stabilized flames”. In: *AIAA journal* 33.12 (1995), pp. 2339–2347. DOI: https://doi.org/10.2514/3.12989.

174. **Eugenio Giacomazzi**, **Valerio Battaglia**, and **Claudio Bruno**. “The coupling of turbulence and chemistry in a premixed bluff-body flame as studied by LES”. In: *Combustion and Flame* 138.4 (2004), pp. 320–335. ISSN: 0010-2180. DOI: https://doi.org/10.1016/j.combustflame.2004.06.004.

175. **M. Boger** et al. “Direct numerical simulation analysis of flame surface density concept for large eddy simulation of turbulent premixed combustion”. In: *Symposium (International) on Combustion* 27.1 (1998). Twenty-Seventh Sysposium (International) on Combustion Volume One, pp. 917–925. ISSN: 0082-0784. DOI: https://doi.org/10.1016/S0082-0784(98)80489-X.

176. **S.B. Pope**. “The evolution of surfaces in turbulence”. In: *International Journal of Engineering Science* 26.5 (1988), pp. 445–469. ISSN: 0020-7225. DOI: https://doi.org/10.1016/0020-7225(88)90004-3.

177. **L. Vervisch** and **D. Veynante**. “Interlinks between approaches for modeling turbulent flames”. In: *Proceedings of the Combustion Institute* 28.1 (2000), pp. 175–183. ISSN: 1540-7489. DOI: https://doi.org/10.1016/S0082-0784(00)80209-X.

178. **V Smiljanovski**, **V Moser**, and **Rupert Klein**. “A capturing-tracking hybrid scheme for deflagration discontinuities”. In: *Combustion Theory and Modelling* 1.2 (1997), p. 183. DOI: 10.1088/1364-7830/1/2/004.

179. **Kenneth Noel Corbett Bray**. "Laminar flamelets in turbulent flames". In: *Turbulent reacting flows* (1994). DOI: https://doi.org/10.1080/00102202.2016.1195819.

180. **O. Colin** et al. "A thickened flame model for large eddy simulations of turbulent premixed combustion". In: *Physics of Fluids* 12.7 (July 2000), pp. 1843–1863. ISSN: 1070-6631. DOI: 10.1063/1.870436.

181. **G. Wang**, **M. Boileau**, and **D. Veynante**. "Implementation of a dynamic thickened flame model for large eddy simulations of turbulent premixed combustion". In: *Combustion and Flame* 158.11 (2011), pp. 2199–2213. ISSN: 0010-2180. DOI: https://doi.org/10.1016/j.combustflame.2011.04.008.

182. **P.S. Volpiani**, **T. Schmitt**, and **D. Veynante**. "A posteriori tests of a dynamic thickened flame model for large eddy simulations of turbulent premixed combustion". In: *Combustion and Flame* 174 (2016), pp. 166–178. ISSN: 0010-2180. DOI: https://doi.org/10.1016/j.combustflame.2016.08.007.

183. **B. Fiorina** et al. "A filtered tabulated chemistry model for LES of premixed combustion". In: *Combustion and Flame* 157.3 (2010), pp. 465–475. ISSN: 0010-2180. DOI: https://doi.org/10.1016/j.combustflame.2009.09.015.

184. **S.B. Pope**. "PDF methods for turbulent reactive flows". In: *Progress in Energy and Combustion Science* 11.2 (1985), pp. 119–192. ISSN: 0360-1285. DOI: https://doi.org/10.1016/0360-1285(85)90002-4.

185. **S.B. Pope**. "Computations of turbulent combustion: Progress and challenges". In: *Symposium (International) on Combustion* 23.1 (1991). Twenty-Third Symposium (International) on Combustion, pp. 591–612. ISSN: 0082-0784. DOI: https://doi.org/10.1016/S0082-0784(06)80307-3.

186. **Luis Valiño**. "A field Monte Carlo formulation for calculating the probability density function of a single scalar in a turbulent flow". In: *Flow, turbulence and combustion* 60.2 (1998), pp. 157–172. DOI: https://doi.org/10.1023/A:1009968902446.

187. **W.P. Jones** and **S. Navarro-Martinez**. "Large eddy simulation of autoignition with a subgrid probability density function method". In: *Combustion and Flame* 150.3 (2007), pp. 170–187. ISSN: 0010-2180. DOI: https://doi.org/10.1016/j.combustflame.2007.04.003.

188. **Vladimir Sabel'nikov** and **Olivier Soulard**. "Rapidly decorrelating velocity-field model as a tool for solving one-point Fokker-Planck equations for probability density functions of turbulent reactive scalars". In: *Physical Review E* 72.1 (2005), p. 016301. DOI: https://doi.org/10.1103/PhysRevE.72.016301.

189. **R. W. Bilger**. "Conditional moment closure for turbulent reacting flow". In: *Physics of Fluids A: Fluid Dynamics* 5.2 (Feb. 1993), pp. 436–444. ISSN: 0899-8213. DOI: 10.1063/1.858867.

190. **S Navarro-Martinez**, **A Kronenburg**, and **F Di Mare**. "Conditional moment closure for large eddy simulations". In: *Flow, Turbulence and Combustion* 75.1 (2005), pp. 245–274. DOI: https://doi.org/10.1007/s10494-005-8580-7.

191. **Ansys Inc.** *Ansys Fluent Theory Guide*. 23.1. Accessed: 2026-03-04. 2023. URL: https://ansyshelp.ansys.com (visited on 03/04/2026).

192. **Hagen Müller**, **Federica Ferraro**, and **Michael Pfitzner**. "Implementation of a Steady Laminar Flamelet Model for non-premixed combustion in LES and RANS simulations". In: *8th International OpenFOAM Workshop*. 2013, pp. 1–12.

193. **Charles D. Pierce** and **Parviz Moin**. "Progress-variable approach for large-eddy simulation of non-premixed turbulent combustion". In: *Journal of Fluid Mechanics* 504 (2004), pp. 73–97. DOI: 10.1017/S0022112004008213.

194. **J. Janicka** and **N. Peters**. "Prediction of turbulent jet diffusion flame lift-off using a pdf transport equation". In: *Symposium (International) on Combustion* 19.1 (1982). Nineteenth Symposium (International) on Combustion, pp. 367–374. ISSN: 0082-0784. DOI: https://doi.org/10.1016/S0082-0784(82)80208-7.

195. **Matthias Ihme**, **Chong M. Cha**, and **Heinz Pitsch**. "Prediction of local extinction and re-ignition effects in non-premixed turbulent combustion using a flamelet/progress variable approach". In: *Proceedings of the Combustion Institute* 30.1 (2005), pp. 793–800. ISSN: 1540-7489. DOI: https://doi.org/10.1016/j.proci.2004.08.260.

196. **Zhi X Chen** et al. "Prediction of local extinctions in piloted jet flames with inhomogeneous inlets using unstrained flamelets". In: *Combust. Flame* 212 (2020), pp. 415–432. URL: https://doi.org/10.1016/j.combustflame.2019.11.007.

197. **H. Pitsch**. "A consistent level set formulation for large-eddy simulation of premixed turbulent combustion". In: *Combustion and Flame* 143.4 (2005). Special Issue to Honor Professor Robert W. Bilger on the Occasion of His Seventieth Birthday, pp. 587–598. ISSN: 0010-2180. DOI: https://doi.org/10.1016/j.combustflame.2005.08.031.

198. **Ken Bray**, **Pascale Domingo**, and **Luc Vervisch**. "Role of the progress variable in models for partially premixed turbulent combustion". In: *Combustion and Flame* 141.4 (2005), pp. 431–437. ISSN: 0010-2180. DOI: https://doi.org/10.1016/j.combustflame.2005.01.017.

199. **A. Soli**, **I. Langella**, and **Z. X. Chen**. "Analysis of Flame Front Breaks Appearing in LES of Inhomogeneous Jet Flames Using Flamelets". In: *Prog. Energy Combust. Sci.* 49 (2021), pp. 189–208. URL: https://doi.org/10.1007/s10494-021-00306-6.

200. **Ivan Langella** et al. “Assessment of dynamic closure for premixed combustion large eddy simulation”. In: *Combustion Theory and Modelling* 19.5 (2015), pp. 628–656. DOI: https://doi.org/10.1080/13647830.2015.1080387.

201. **Gioele Ferrante**, **Zhi X Chen**, and **Ivan Langella**. “Dynamic modelling of subgrid scalar dissipation rate in premixed and partially premixed flames with differential filter”. In: *Appl. Therm. Eng.* 248 (2024), p. 123233. URL: https://doi.org/10.1016/j.applthermaleng.2024.123233.

202. **N. Mukundakumar** et al. “A new preferential diffusion model applied to FGM simulations of hydrogen flames”. In: *Combust. Theory Model.* 25.7 (2021), pp. 1245–1267. URL: https://doi.org/10.1080/13647830.2021.1970232.

203. **Gioele Ferrante**, **Georg Eitelberg**, and **Ivan Langella**. “Differential diffusion modelling for LES of premixed and partially premixed flames with presumed FDF”. In: *Combust. Theory Model.* (2024), pp. 1–36. URL: https://doi.org/10.1080/13647830.2024.2389099.

204. **Paul J Colucci** et al. “Filtered density function for large eddy simulation of turbulent reacting flows”. In: *Physics of Fluids* 10.2 (1998), pp. 499–515. DOI: https://doi.org/10.1063/1.869537.

205. **Feng Gao** and **Edward E. O’Brien**. “A large-eddy simulation scheme for turbulent reacting flows”. In: *Physics of Fluids A: Fluid Dynamics* 5.6 (June 1993), pp. 1282–1284. ISSN: 0899-8213. DOI: 10.1063/1.858617.

206. **Farhad A. Jaberi** and **Paul J. Colucci**. “Large eddy simulation of heat and mass transport in turbulent flows. Part 1: Velocity field”. In: *International Journal of Heat and Mass Transfer* 46.10 (2003), pp. 1811–1825. ISSN: 0017-9310. DOI: https://doi.org/10.1016/S0017-9310(02)00484-2.

207. **César Dopazo** and **Edward E. O’Brien**. “Functional formulation of nonisothermal turbulent reactive flows”. In: *The Physics of Fluids* 17.11 (Nov. 1974), pp. 1968–1975. ISSN: 0031-9171. DOI: 10.1063/1.1694652.

208. **Cesar Dopazo**. “Probability density function approach for a turbulent axisymmetric heated jet. Centerline evolution”. In: *The Physics of Fluids* 18.4 (1975), pp. 397–404. DOI: https://doi.org/10.1063/1.861163.

209. **Cesar Dopazo**. “Relaxation of initial probability density functions in the turbulent convection of scalar fields”. In: *The Physics of Fluids* 22.1 (Jan. 1979), pp. 20–30. ISSN: 0031-9171. DOI: 10.1063/1.862431.

210. **W.P. Jones** and **M. Kakhi**. “Pdf Modeling of Finite-rate Chemistry Effects in Turbulent Nonpremixed Jet Flames”. In: *Combustion and Flame* 115.1 (1998), pp. 210–229. ISSN: 0010-2180. DOI: https://doi.org/10.1016/S0010-2180(98)00002-9. URL: https://www.sciencedirect.com/science/article/pii/S0010218098000029.

211. **W.P. Jones**, **A.J. Marquis**, and **V.N. Prasad**. "LES of a turbulent premixed swirl burner using the Eulerian stochastic field method". In: *Combustion and Flame* 159.10 (2012), pp. 3079–3095. ISSN: 0010-2180. DOI: https://doi.org/10.1016/j.combustflame.2012.04.008.

212. **Vinayaka Nakul Prasad**. "Large eddy simulation of partially premixed turbulent combustion". PhD thesis. Imperial College London (University of London), 2011.

213. **Eirik Æsøy** et al. "Acoustic-Convective Interference in Transfer Functions of Methane/Hydrogen and Pure Hydrogen Flames". In: *ASME J. Eng. Gas Turbines Power* 143.12 (Oct. 2021), p. 121017. DOI: https://doi.org/10.1115/1.4051960.

214. **Eirik Æsøy** et al. "Tailoring the Gain and Phase of the Flame Transfer Function through Targeted Convective-Acoustic Interference". In: *Combust. Flame* 236 (Feb. 2022), p. 111813. DOI: https://doi.org/10.1016/j.combustflame.2021.111813.

215. **Eirik Æsøy** et al. "Suppression of Self-Excited Thermoacoustic Instabilities by Convective-Acoustic Interference". In: *Proc. Combust. Inst.* 39.4 (2023), pp. 4611–4620. DOI: https://doi.org/10.1016/j.proci.2022.08.033.

216. **TNF Workshop**. *Hydrogen Flames*. Accessed: February 24, 2026. TNF Workshop, 2026. URL: https://tnfworkshop.org/.

217. **Andrea Aniello** et al. "Experimental and Numerical Investigation of Two Flame Stabilization Regimes Observed in a Dual Swirl H2-Air Coaxial Injector". In: *Combust. Flame* 249.4 (Mar. 2023), p. 112595. DOI: https://doi.org/10.1016/j.combustflame.2022.112595.

218. **Andrea Ballotti**, **Simone Castellani**, and **Antonio Andreini**. "A Dynamic Thickening Strategy for High-Fidelity Computational Fluid Dynamics Analyses of Multi-Regime Combustion". In: *ASME J. Eng. Gas Turbines Power* 146.12 (Sept. 2024), p. 121010. DOI: https://doi.org/10.1115/1.4066212.

219. **Halit Kutkan** et al. "LES of Turbulent Premixed CH4/H2/Air Flames with Stretch and Heat Loss for Flame Characteristics and Dynamics". In: *Proceedings of ASME Turbo Expo 2022* (Rotterdam, The Netherlands). GT2022-82397. 2022, V03BT04A021. DOI: https://doi.org/10.1115/GT2022-82397.

220. **Halit Kutkan** et al. "Modeling of Turbulent Premixed CH4/H2/Air Flames Including the Influence of Stretch and Heat Losses". In: *ASME J. Eng. Gas Turbines Power* 144.1 (Jan. 2022), p. 011020. DOI: https://doi.org/10.1115/1.4051989.

221. **Matteo Amerighi** et al. “Complete Dynamics From Ignition to Stabilization of a Lean Hydrogen Flame With Thickened Flame Model”. In: *ASME J. Eng. Gas Turbines Power* 147.4 (Apr. 2025), p. 041019. DOI: https://doi.org/10.1115/1.4066590.

222. **Tarik Yahou**, **James R Dawson**, and **Thierry Schuller**. “Impact of Chamber Back Pressure on the Ignition Dynamics of Hydrogen Enriched Premixed Flames”. In: *Proc. Combust. Inst.* 39.4 (2023), pp. 4641–4650. DOI: https://doi.org/10.1016/j.proci.2022.07.236.

223. **Weiyue Liu** and **W.P. Jones**. “LES of dual-swirl non-premixed H2 turbulent flame using Eulerian stochastic fields”. In: *Combustion and Flame* 275 (2025), p. 114094. ISSN: 0010-2180. DOI: https://doi.org/10.1016/j.combustflame.2025.114094.

224. **Weiyue Liu** and **W.P. Jones**. “Differential diffusion effects in a lean-premixed bluff-body stabilized hydrogen flame”. In: *Combustion and Flame* 284 (2026), p. 114682. ISSN: 0010-2180. DOI: https://doi.org/10.1016/j.combustflame.2025.114682.

225. **Gregory P. Smith** et al. *Current and Future Releases of GRI-Mech*. University of Berkelet. URL: http://www.me.berkeley.edu/gri_mech/.

226. **James C Tyacke** and **Paul G Tucker**. “Future Use of Large Eddy Simulation in Aero-Engines”. In: *ASME J. Turbomach.* 137.8 (Aug. 2015), p. 081005. DOI: https://doi.org/10.1115/1.4029363.

227. **IB Celik**, **ZN Cehreli**, and **I Yavuz**. “Index of Resolution Quality for Large Eddy Simulations”. In: *ASME J. Turbomach.* 127.5 (Sept. 2005), pp. 949–958. DOI: https://doi.org/10.1115/1.1990201.

228. **Reo Kai** et al. “LES flamelet modeling of hydrogen combustion considering preferential diffusion effect”. In: *International Journal of Hydrogen Energy* 48.29 (2023), pp. 11086–11101. DOI: https://doi.org/10.1016/j.ijhydene.2022.12.164.

229. **Noah Klarmann** et al. “Flamelet Generated Manifolds for Partially Premixed, Highly Stretched and Non-Adiabatic Combustion in Gas Turbines”. In: *54th AIAA Aerospace Sciences Meeting* (San Diego, California, USA). AIAA 2016-2120. 2016. DOI: https://doi.org/10.2514/6.2016-2120.

230. **H Yamashita**, **M Shimada**, and **T Takeno**. “A Numerical Study on Flame Stability at the Transition Point of Jet Diffusion Flames”. In: *Symposium (international) on combustion* 26.1 (1996), pp. 27–34. DOI: https://doi.org/10.1016/S0082-0784(96)80196-2.

231. **E Knudsen** and **H Pitsch**. “Capabilities and Limitations of Multi-Regime Flamelet Combustion Models”. In: *Combust. Flame* 159.1 (Jan. 2012), pp. 242–264. DOI: https://doi.org/10.1016/j.combustflame.2011.05.025.

232. **Yujuan Luo** et al. “Assessment of Flamelet Manifolds for Turbulent Flame-Wall Interactions in Large-Eddy Simulations”. In: *Combust. Flame* 255 (Sept. 2023), p. 112923. DOI: https://doi.org/10.1016/j.combustflame.2023.112923.

233. **Jonathan D. Regele** et al. “A two-equation model for non-unity Lewis number differential diffusion in lean premixed laminar flames”. In: *Combust. Flame* 160.2 (2013), pp. 240–250. URL: https://doi.org/10.1016/j.combustflame.2012.10.004.

234. **P. E. Lapenna**, **R. Lamioni**, and **F. Creta**. “Subgrid modeling of intrinsic instabilities in premixed flame propagation”. In: *Proc. Combust. Inst.* 38.2 (2021), pp. 2001–2011. ISSN: 1540-7489. URL: https://doi.org/10.1016/j.proci.2020.06.192.

235. **R Cabra** et al. “Simultaneous laser Raman-Rayleigh-LIF measurements and numerical modeling results of a lifted turbulent H_2/N_2 jet flame in a vitiated coflow”. In: *Proc. Combust. Inst.* 29 (2002), pp. 1881–1888. URL: https://doi.org/10.1016/S1540-7489(02)80228-0.

236. **Reo Kai** et al. “LES flamelet modeling of hydrogen combustion considering preferential diffusion effect”. In: *Int. J. Hydrog. Energy* 48.29 (2023), pp. 11086–11101. URL: https://doi.org/10.1016/j.ijhydene.2022.12.164.

237. **Takeshi Shoji** et al. “Effects of flame behaviors on combustion noise from lean-premixed hydrogen low-swirl flames”. In: *AIAA journal* 58.10 (2020), pp. 4505–4521. DOI: https://doi.org/10.2514/1.J059049.

238. **T Capurso** et al. “NOx pathways in lean partially premixed swirling H2-air turbulent flame”. In: *Combust. Flame* 248 (2023), p. 112581. DOI: https://doi.org/10.1016/j.combustflame.2022.112581.

239. **Sylvain Marragou** et al. “Stabilization regimes and pollutant emissions from a dual fuel CH4/H2 and dual swirl low NOx burner”. In: *Int. J. Hydrog. Energy* 47.44 (2022), pp. 19275–19288. DOI: https://doi.org/10.1016/j.ijhydene.2022.04.033.

240. **Ivan Langella** and **Nedunchezhian Swaminathan**. “Unstrained and strained flamelets for LES of premixed combustion”. In: *Combust. Theory Model.* 20.3 (2016), pp. 410–440. URL: https://doi.org/10.1080/13647830.2016.1140230.

241. **Böttler** et al. “Can flamelet manifolds capture the interactions of thermo-diffusive instabilities and turbulence in lean hydrogen flames? - An a-priori analysis”. In: *Int. J. Hydrog. Energy* 56 (2024), pp. 1397–1407. URL: https://doi.org/10.1016/j.ijhydene.2023.12.193.

242. **Lukas Berger** et al. “LES combustion model for premixed turbulent hydrogen flames with thermodiffusive instabilities: a priori and a posteriori analysis”. In: *Journal of Fluid Mechanics* 1003 (2025), A33. URL: https://doi.org/10.1017/jfm.2024.1201.

243. **Eindhoven University of Technology**. *CHEM1D. A one dimensional laminar flame code*. 2021.

244. **Michael P Burke** et al. “Comprehensive H2/O2 kinetic model for high-pressure combustion”. In: *International Journal of Chemical Kinetics* 44.7 (2012), pp. 444–474. URL: https://doi.org/10.1002/kin.20603.

245. **E. Æsøy** and **James R. Dawson**. *TNF workshop*. 2023. URL: https://tnfworkshop.org/bluff-body-hydrogen-flame-ntnu-trondheim/ (visited on 11/27/2024).

246. **Alessandro Porcarelli** and **Ivan Langella**. “Mitigation of preferential diffusion effects by intensive strain in lean premixed hydrogen flamelets”. In: *Proceedings of the Combustion Institute* 40.1-4 (2024), p. 105728. DOI: https://doi.org/10.1016/j.proci.2024.105728.

247. **AN Lipatnikov** and **Jerzy Chomiak**. “Molecular transport effects on turbulent flame propagation and structure”. In: *Prog. Energy Combust.* 31.1 (2005), pp. 1–73. URL: https://doi.org/10.1016/j.pecs.2004.07.001.

248. **Alessandro Porcarelli** et al. “Stability analysis of thermodiffusively unstable counterflow lean premixed hydrogen flames”. In: *Proceedings of the Combustion Institute* 41 (2025), p. 105906. URL: https://doi.org/10.1016/j.proci.2025.105906.

249. **JA Van Oijen** et al. “State-of-the-art in premixed combustion modeling using flamelet generated manifolds”. In: *Progress in Energy and Combustion Science* 57 (2016), pp. 30–74. URL: https://doi.org/10.1016/j.pecs.2016.07.001.

250. **H. Pitsch**, **M. Chen**, and **N. Peters**. “Unsteady flamelet modeling of turbulent hydrogen-air diffusion flames”. In: *Symposium (International) on Combustion* 27.1 (1998). Twenty-Seventh Sysposium (International) on Combustion Volume One, pp. 1057–1064. ISSN: 0082-0784. DOI: https://doi.org/10.1016/S0082-0784(98)80506-7.

251. **J.P.H. Sanders**, **J.-Y. Chen**, and **I. Gökalp**. “Flamelet-based modeling of NO formation in turbulent hydrogen jet diffusion flames”. In: *Combustion and Flame* 111.1 (1997), pp. 1–15. ISSN: 0010-2180. DOI: https://doi.org/10.1016/S0010-2180(97)00094-1.

252. **Mohamad Fathi** et al. “Effects of intense strain on flame structure and NOx generation in turbulent counterflow lean-premixed hydrogen flames”. In: *Combustion and Flame* 282 (2025), p. 114459. DOI: https://doi.org/10.1016/j.combustflame.2025.114459.

253. **Maria Rosaria Acquaviva**, **Alessandro Porcarelli**, and **Ivan Langella**. “Influence of Soret effect on flame structure and NOx emissions in highly strained lean premixed counterflow hydrogen flames”. In: *Fuel* 395 (2025), p. 134939. DOI: https://doi.org/10.1016/j.fuel.2025.134939.

254. **Dominik Ebi** and **Noel T. Clemens**. “Experimental investigation of upstream flame propagation during boundary layer flashback of swirl flames”. In: *Combustion and Flame* 168 (2016), pp. 39–52. DOI: https://doi.org/10.1016/j.combustflame.2016.03.027.

255. **Martin Skottene** and **Kjell Erik Rian**. “A study of NOx formation in hydrogen flames”. In: *International Journal of Hydrogen Energy* 32.15 (2007), pp. 3572–3585. DOI: https://doi.org/10.1016/j.ijhydene.2007.02.038.

256. **Tarek Echekki** and **Epaminondas Mastorakos**. “Turbulent combustion modeling: Advances, new trends and perspectives”. In: (2010). DOI: 10.1007/978-94-007-0412-1.

257. **EJ Pérez-Sánchez**, **EM Fortes**, and **D Mira**. “Assessment of the Flamelet Generated Manifold method with preferential diffusion modeling for partially premixed hydrogen flames”. In: *Combustion and Flame* 277 (2025), p. 114141. DOI: https://doi.org/10.1016/j.combustflame.2025.114141.

258. **Stijn N.J. Schepers** and **Jeroen A. van Oijen**. “FGM modeling of thermo-diffusive unstable lean premixed hydrogen–air flames”. In: *Combustion and Flame* 280 (2025), p. 114332. ISSN: 0010-2180. DOI: https://doi.org/10.1016/j.combustflame.2025.114332.

259. **Hannes Böttler** et al. “Flamelet modeling of thermo-diffusively unstable hydrogen-air flames”. In: *Proceedings of the Combustion Institute* 39.2 (2023), pp. 1567–1576. DOI: https://doi.org/10.1016/j.proci.2022.07.159.

260. **Jean-Philippe Legier**, **Thierry Poinsot**, and **Denis Veynante**. “Dynamically thickened flame LES model for premixed and non-premixed turbulent combustion”. In: *Proceedings of the summer program*. Vol. 12. Center for Turbulence Research Stanford, CA. 2000, pp. 157–168.

261. **TD Butler** and **Peter J O’Rourke**. “A numerical method for two dimensional unsteady reacting flows”. In: *Symposium (international) on combustion*. Vol. 16. 1. Elsevier. 1977, pp. 1503–1515. DOI: https://doi.org/10.1016/S0082-0784(77)80432-3.

262. **Jean-Jacques Hok** et al. “A modeling strategy for the Thickened Flame simulation of propagating lean hydrogen–air flames”. In: *International Journal of Hydrogen Energy* 78 (2024), pp. 1133–1141. DOI: https://doi.org/10.1016/j.ijhydene.2024.06.298.

263. **Nicola Detomaso** et al. “A generalization of the Thickened Flame model for stretched flames”. In: *Combustion and Flame* 258 (2023), p. 113080. DOI: https://doi.org/10.1016/j.combustflame.2023.113080.

264. **M Vilespy** et al. “Analysis of the origin of NOx emissions in non premixed dual swirl hydrogen flames”. In: *Combustion and Flame* 273 (2025), p. 113925. DOI: https://doi.org/10.1016/j.combustflame.2024.113925.

265. **Michael C. Drake** and **Richard J. Blint**. “Thermal NOx in stretched laminar opposed-flow diffusion flames with CO/H2/N2 fuel”. In: *Combustion and Flame* 76.2 (1989), pp. 151–167. DOI: https://doi.org/10.1016/0010-2180(89)90064-3.

266. **Michael P Burke** et al. “Comprehensive H2/O2 kinetic model for high-pressure combustion”. In: *International Journal of Chemical Kinetics* 44.7 (2012), pp. 444–474. DOI: https://doi.org/10.1002/kin.20603.

267. **T Capurso** et al. “NOx pathways in lean partially premixed swirling H2-air turbulent flame”. In: *Combustion and Flame* 248 (2023), p. 112581. DOI: https://doi.org/10.1016/j.combustflame.2022.112581.

268. **Lukas Berger** et al. “Effects of Karlovitz number variations on thermodiffusive instabilities in lean turbulent hydrogen jet flames”. In: *Proceedings of the Combustion Institute* 40.1-4 (2024), p. 105219. DOI: https://doi.org/10.1016/j.proci.2024.105219.

269. **Ivan Langella**. “Large eddy simulation of premixed combustion using flamelets”. PhD thesis. Apollo - University of Cambridge Repository, 2016. DOI: 10.17863/CAM.14139.

270. **Shuguo Shi** et al. “Assessing turbulence–flame interaction of thermo-diffusive lean premixed H2/air flames towards distributed burning regime”. In: *Combustion and Flame* 269 (2024), p. 113699. DOI: https://doi.org/10.1016/j.combustflame.2024.113699.

271. **C.K. Law**. *Combustion Physics*. Cambridge University Press, 2010. ISBN: 9781139459242. URL: https://books.google.it/books?id=vWgJvKMXwQ8C.

Aknowledgments

This publication thesis was produced while attending the PhD programme in Industrial Engineering at the University of Cagliari, Cycle XXXVIII, with the support of a scholarship financed by NRRP, funded by the European Union - NextGenerationEU - Mission 4 "Education and Research", Component 2 “From Research to Business” - Investment 1.5 “Creating and strengthening "innovation ecosystems", building "local R&D leaders”.